UTS UNIVERSITY OF TECHNOLOGY SYDNEY

Load identification and structural damage detection of bridges

by Bing Zhang

Thesis submitted in fulfilment of the requirements for the degree of

Doctor of Philosophy

under the supervision of A/Prof Xinqun Zhu

University of Technology Sydney

Faculty of Engineering and Information Technology

October 2022

Certificate of Original Authorship

I, Bing Zhang declare that this thesis, is submitted in fulfilment of the requirements for the award of Doctor of Philosophy, in the School of Civil and Environmental Engineering, Faculty of Engineering and Information Technology at the University of Technology Sydney.

This thesis is wholly my own work unless otherwise referenced or acknowledged. In addition, I certify that all information sources and literature used are indicated in the thesis.

This document has not been submitted for qualifications at any other academic institution.

This research is supported by the Australian Government Research Training Program.

Signature

Date: October 5, 2022

Acknowledgement

First and foremost, I would like to give my deepest gratitude to my principal supervisor, Prof. Xinqun Zhu for your invaluable advice, continuous support, and patience during my PhD study. This doctoral thesis would not have been possible without your guidance and help. I learned a lot from the discussion with you in your office, where you always patiently explained the ideas and mechanisms to me. I learned a lot from your broad knowledge, inspiring ideas and enthusiasm in scientific research. Also, I would like to thank you for your encouragement and patience which were supportive for my first two years when I was lost. Those experiences trained me to be a person with independent thought and an open mind which is helpful for my future study and work.

I also would like to express my great appreciation to my other supervisors, Prof. Jianchun Li, Dr. Wengui Li and Dr. Yang Yu for their advice and guidance during my PhD study. Especially, Prof. Jianchun Li's guidance helped me a lot in my research. Interesting and lively discussions we had in each group meeting always bring me inspiration for scientific research.

My sincere thanks also go to the University of Technology Sydney for providing excellent research and social environment, scholarships, financial supports, facilities, and funding resources that made this thesis possible.

Friends are always the sources of my happiness and colourful life. I particularly appreciate my dear friends who have mad the leisure time of journey pleasant and enriched my daily life.

Family is always the strongest shield while I am stuck in the frustration of study. I appreciate my parents and my sister who are always unconditionally supporting me. Without my family support, I would not have achieved my goals and no words can describe the appreciation for their encouragement. Special thanks are given to my wife, Dr. Xuan Zhang, who is always by my side, encouraging me and trusting me.

List of publications

1. **Zhang B.** and Zhu X.Q. (2021) "Study of shear connector damage influence on interface slippage in steel-concrete composite beams with a novel slippage measurement method", *Proceedings of the 10th Australasian Congress on Applied Mechanics*, Engineers Australia, pp.491-503.
2. Ren J.Y., **Zhang B.**, Zhu X.Q. and Li S.H. (2022) "Damaged cable identification in cable-stayed bridge from bridge deck strain measurements using support vector machine." *Advanves in Structural Engineering*, 25(4), 754-771.
3. Li J.T., Zhu X.Q., **Zhang B.** and Samali B. (2022) "Chapter 3: Drive-by bridge structural health monitoring: a case study on modal identification using a mobile sensory system." *Recent Advances in Structural Health Monitoring Research in Australia*, NOVA Science Publishers, pp. 113-136.
4. **Zhang B.**, Zhu X.Q. and Li J.C (2022) "Impact force identification based on truncated transfer matrix", *Mechanical Systems and Signal Processing*. (Under preparation)
5. **Zhang B.**, Zhu X.Q. and Li J.C (2022) "Low-rank transfer submatrix-based group sparse regularisation for impact force localization and reconstruction", *Journal of Sound and Vibration*. (Under preparation)

Table of Contents

List of Figures

List of Tables

Abstract

Load identification and structural damage detection are two important research areas in bridge structural health monitoring (SHM). In practice, the incomplete measurement information, variable service environments and other uncertainties make the structural load and damage identification difficult. Currently, many identification methods for load identification and bridge structural damage detection cannot effectively serve under operating conditions. Hence how to use the SHM data to accurately estimate the loads and evaluate the structural damage of the bridge has been a hot topic for researchers and engineers in the world. This study will focus on these two areas including the following contents.

Regarding the load identification, a truncated transfer matrix-based regularisation method is proposed for impact force identification. This method includes two steps. The first step is the force location identification. Once the location is determined, the transfer matrix for the force value identification could be constructed, then the force value identification could be conducted in the second step. To improve the impact force localization and value identification method, a low rank transfer submatrix-based group sparse regularisation method is proposed to localise and reconstruct the impact force simultaneously. The low rank transfer submatrix-based group sparse regularisation method is to construct a structured regularisation on the unknown forces, by binding the unknown amplitudes associated with different potential locations into separate groups and promoting the group-level sparsity among the potential locations. Similarly, the group sparse feature also exists in the equivalent nodal force which is transferred from the moving force. Based on this feature, a group weighted Tikhonov regularisation method is proposed for the moving force identification via the equivalent nodal force. These proposed methods for load identification are validated numerically and experimentally.

In terms of structural damage detection, a new interface slip monitoring system based on Ultra-flat Industrial Potentiometer Membrane (UIPM) sensor has been developed to directly measure the relative displacement between the concrete slab and steel girder and the integrity of the shear connectors has been assessed by the slip measurements. The finite element model has been developed to study the interface damage detection of the steel-concrete composite structure under the pseudo moving vehicular load. The results show that the slippage divergence ratio is very sensitive to the shear connector damage, which is a potential indicator for the damage of the shear connection system.

In practice, the cable force of the cable-stayed bridge is difficult to be monitored for its damage detection. Based on the relationship between the cable force and the strain of the bridge deck, a new method is proposed for the localization and servility identification of cable damage using the strain measurements on the bridge deck. Here the damage cable identification problem is treated as a multi-classification problem and the damage degree identification problem as a nonlinear regression problem using support vector machine. The results show that the proposed method has a strong anti-noise performance and can be easily adapted to the health monitoring system in the field.

Chapter 1 Introduction

1.1 Background

Bridge structures are regarded as important components of transportation networks. The existing bridges are rapidly deteriorating with long-term excessive loads, harsh environments, aging materials. These factors will make the bridge structural bearing capacity decline, and eventually cause the bridge damage. The damage or even collapse of bridges resulting from their structural deterioration disrupts transportation systems and directly results in the tragedy of the life and property loss. During the service of the bridge, the operational load induced by the moving vehicles is one of the main live loads on the bridge. The overheavy vehicles will increase the road damage by 1.2 to 4 times (Cebon 1989) and cause 70% of the bridge response (Cantieni 1984). According to the report of the United States Federal Highway Administration (*National Bridge Inventory (NBI)*), there were 611,845 highway bridges in the United States in 2015, of which 142,915 were unhealthy bridges, accounting for up to 36%. If the bridge damage has not been repaired and reinforced in time, particularly under the long-term effect of over-limit vehicle loads, it is easy to cause damage accumulation, aggravate damage and even cause catastrophic accidents in extreme cases. The collapse accident of Hintze-Ribeiro Bridge in Portugal in 2001 and the catastrophic Minnesota River Bridge collapse (Figure1.1) in the USA in 2007 highlighted the importance of accurately monitoring, assessing, maintaining and prolonging the design life of our aging bridges. In order to accurately obtain the bridge service status and ensure the safety in the bridge operation, bridge structure health monitoring research has urgent social needs and a great engineering significance.

(a) Hintze-Ribeiro Bridge collapse (b) Minnesota River Bridge collapse

Figure 1.1 Bridge damage cause catastrophic accidents

Operational load identification and structural damage detection are two important research areas in the bridge SHM. Accurate identification of the operational loads and structural damage on the bridge is helpful to the operation, evaluation and maintenance of the existing bridge, and the operational loads can also provide reliable data for the bridge design code. With the advancement of the structural health monitoring technology, many methods for structural damage detection and operational load identification have been developed over the past three decades (Carden and Fanning 2004; Casas and Moughty 2017; Fan and Qiao 2011; Wang and Chan 2009). In practice, the actual bridge structure is generally large and complex, the number of measuring points in existing SHM systems are not sufficient, and the service environment is time-varying. Most existing methods cannot be used to reconstruct the dynamic load and predict the bridge local damage in operational environments, and this is the drawback of the SHM technique for practical applications. In terms of bridge operational load identification and structural damage detection, there are still many problems in the current research as reviewed in Chapter 2. Four main problems to be focused in this project are summarised as follows:

(1) Most existing methods are to identify the impact forces with known locations. In practice, the locations the forces are unknown, which will introduce another challenge for the force

identification problem. It is necessary to study the problem of impact force identification with the unknown locations and develop a new method for impact load identification.

(2) Most existing methods for moving force identification are usually based on the modal decomposition and they are subject to modal truncation errors in the dynamic responses. To solve this problem, an attempt is made to identify the moving vehicle load via equivalent nodal forces.

(3) The vibration-based method is a global method and it is difficult to identify the local damage, such as the damage in the shear connection system of steel-concrete composite structures. Damage or failure of shear connectors results in the interface slip and hence the relative displacement between girders and the slab could be a good damage indicator of the shear connection system. However, the existing methods are not suitable for monitoring the slip during the bridge life cycle. A new applicable measurement method for composite slab-on-girder bridges needs to be developed for practical applications.

(4) Many indicators have been proposed for detecting the cable damage. But the interrelationship of the indicators and their respective sensitivity relative to the damage severity and location have not yet been considered together to improve the effectiveness and efficiency of damage detection.

1.2 Research objectives

The primary aim of this research project is to develop the vehicle-bridge interaction (VBI) based monitoring system for bridge structural damage detection. Aiming at the research gaps listed in Section 1.1, the detail objectives in this research are as follows:

(1) Considering the strong correlation of adjacent column vectors in transfer matrix and the specific feature of the impact force and its relevant dynamic response, to develop new method to localise and reconstruct the impact force.

(2) To develop new method for moving force identification that applied to complicated structure.

(3) To investigate a new interface slippage monitoring system developed for shear connector damage detection of composite beam.

(4) To study the interrelationship of the damage indicators and their respective sensitivity relative to the damage severity and damage location.

1.3 Significance

Accurate identification of the operational load and structural damage on the bridge is significant to the operation, evaluation and maintenance of the existing bridge, and can also provide reliable data for the bridge design code. The approach for operational load identification that will consider the unknown locations can be able to overcome some difficulties in operational environments. The method proposed for bridge local damage detection in this research will integrate the damage features together to identify the severity and location of the local damage, which will improve the accuracy of detection. Based on the above two methods, the problem of simultaneous identification of the operational load and structural damage will be transformed into a single identification problem of operational load, which is suitable for the practical engineering.

Overall, because ageing bridge infrastructures are still actively in service in the world, the proposed methods will make a significant contribution to monitor their structural conditions and in protecting the structure and human lives.

1.4 Structure of the thesis

This thesis is organised into eight chapters.

Chapter 1 introduces the background, research objectives, significance, and the structure of the thesis.

Chapter 2 presents a detailed review of load identification, VBI based bridge damage detection and simultaneous identification of the system input and state. This overview helps to find out the research gap and contribution.

In Chapter 3, a new two-step approach is proposed for multiple impact force identification based on truncated transfer matrix. The first step is to localise the impact forces using the sparse regularisation technique. Once the force location is determined, the transfer matrix can be constructed. Then the second step is to identify the force values using a truncated transfer matrix-based regularisation technique.

In Chapter 4, one low-rank transfer submatrix-based group sparse regularisation method for impact force localization and reconstruction is proposed. With this technique, the localization and time history reconstruction of the impact force could be realized simultaneously in a determined situation with one sensor configuration.

In Chapter 5, one group weighted Tikhonov regularisation method is proposed for moving force identification via equivalent nodal forces. Its effectiveness and applicability are studied numerically on a simply supported beam in comparison with the standard sparse regularisation method and the classical Tikhonov regularisation method.

In Chapter 6, a new interface slip monitoring system is developed to measure directly the relative displacement between concrete slab and steel girder. The detailed design, working principle and calibration of the slip sensor are presented. Parametric studies base on one accurate numerical model were performed to investigate the variation in shear connector damage severities, shear connector damage positions and load positions on interface slippage performance.

In Chapter 7, a new Damage Cable Identifier (DCI) and a new Damage Degree Identifier (DDI) are proposed for the cable damage situation in a cable-stayed bridge, based on deck bending

strain responses and Support Vector Machine (SVM). Then the proposed method is verified using numerical study and experimental test.

Chapter 8 summarises the methods developed in this thesis and points out their features. Finally, recommendations for future study and potential research direction are discussed.

Chapter 2 Literature Review

2.1 Overview

This thesis is to develop the methods for the load and structural damage identification for bridges. Accurate identification of the operational loads and structural damage on the bridge is helpful to the operation, evaluation and maintenance of the existing bridge, and the operational loads can also provide reliable data for the bridge design code. Load identification and vibration based structural damage detection has been widely studied last three decades and many methods have been developed. This chapter is to review recent developments and find the research gaps in these aspects. The chapter will be organised as four aspects: (a) Load identification; (b) VBI based structural damage detection; (c) Bridge local damage detection; (d) Simultaneous identification of the operational load and damage.

2.2 Load identification

For an engineering system under the forces, the relationship between the force and the system response can be represented as a mathematical function,

$$\mathbf{L}[\mathbf{b}(t)] = \mathbf{f}(t) \tag{2.1}$$

where $\mathbf{L}$ is a mathematical operator, $\mathbf{b}(t)$ represents the structural responses, and $\mathbf{f}(t)$ is the force acting on the system. The model can be linear or nonlinear.

If the forces $\mathbf{f}(t)$ are known, to find the system responses $\mathbf{b}(t)$ is typically referred to as a forward problem. There is another case. The responses of the system are measured and the forces on the system are unknown. Using the system responses to estimate the forces is opposite to the forward problem and it is referred to as an inverse problem.

2.2.1 Load identification methods

The analysis of the forward problem is straightforward, typically involving the solution of differential equations for the system. The inverse problem is very different from the forward problem. For the inverse problem, the influence of measurement noise is significant on the identification results. The load identification problems are ill-conditioned problems. The small changes in the input response data or model parameters will result in large errors in the load identification results or solutions. Thus, the solution of the inverse problem is much susceptible to indeterminacies such as singularities or non-uniqueness of the solution and this requires a higher level of analytical rigor compared with that of the forward problem. Many methods have been developed for load identification. To facilitate the analysis and summarization of the basic ideas and features of these methods, these methods can be divided into five categories: the direct inversion approach, the regularisation approach, Kalman filtering, the stochastic based approach and the artificial intelligence-based approach.

The direct inversion approach is to establish the relationship between the dynamic load and structural vibration response for inverse calculating to estimate the dynamic load. Bartlett and Flannelly (1979) first used the direct inversion approach to reconstruct the dynamic load in the frequency domain for the helicopter pulp. Okubo (1985) identified the excitation force of the machine tool and automobile engine and analysed the influence of measurement noise on the identified results. Later, Hansen (1990) found that the frequency response function matrix is close to the pathological state near the resonance region in the direct inversion approach. The condition number is calculated with the maximum column norm, and the condition number of the modal matrix can be improved by the sensor placement. To reduce the dynamic load identification error, the improved frequency response function matrix inversion methods have proposed. To avoid the deficiency of the numerical method for dynamic load identification, Chen et al. (2012) proposed a time domain semi-analytical method by combining the discrete

data fitting and modal decomposition to identify the load on the structure. The numerical results show that the method is effective to identify the position of the dynamic load on the structure. The regularisation technique is an effective method to solve the ill-conditioned problem. Law et al. (2001) firstly introduced the regularisation technique into moving force identification in time domain. Yu and Chan (2003) used the singular value decomposition and direct inversion methods to calculate the generalized inverse of the structural feature matrix for identifying the moving load. The results show that the singular value decomposition has better result than that by the direct inversion method. Mao (2009) discretely transformed the equation of state of a linear time-invariant system into an algebraic equation when identifying the impact load and obtains the regularized solution of the algebraic equation by singular value decomposition method. Compared with the least squares method, the singular value decomposition method has better noise immunity. The truncated singular value decomposition method is a regularisation method for solving the rank loss of the system matrix. It mainly filters out the small singular values of the system matrix to maintain the stability of the solution. The overall least squares method is a type of regularisation method for solving structural models and vibration responses with errors. Liu and Shepard Jr (2005) studied the effects of frequency response function error and vibration response error on dynamic load identification, in which extended least squares method, truncated singular value decomposition method, Tikhonov regularisation method and total least square method are used respectively. The results of identifying the dynamic loads on the structure shows that the overall least squares method is better than the results identified by other regularisation methods.

Kalman filter theory is a very well-known state estimation theory. Because of its accuracy, it is often used as a state estimator to estimate the operating state of the system. Since the theory was proposed in 1960, it has been widely used in the field of engineering. The Kalman filter algorithm based on this theory is a recursive data processing algorithm that does not need to

store too much historical information, but only Need to constantly update the information, thus occupying a very small computer storage space, is an effective online state estimation algorithm, which can identify the latest state of the system under working status in real time.

Hwang et al. (2009) used the Kalman filter algorithm to estimate the modal force of the structure with the response of the finite measurement point, and analysed the dynamic response type, noise level and structure. The influence of dynamic characteristics on the identification results of dynamic loads. Through the test data, it can be found that the displacement and velocity response are relatively stable for dynamic load identification. However, considering the difficulty of testing the speed and displacement response in engineering practice, the easy-to-test acceleration response is usually used to identify the dynamic load. To extend the dynamic load identification algorithm to nonlinear systems, the researchers introduced an extended Kalman filter algorithm. The basic idea is to perform Taylor expansion on the nonlinear function in the system model at the last moment of state estimation. The higher order term above the second order in the expansion equation obtains the linearization model of the nonlinear system, so that the Kalman filter algorithm can be applied to the dynamic load identification of the nonlinear system, thus solving the above problem. Ma and Ho (2004) combines the extended Kalman filter method with the recursive least squares method to identify the dynamic load acting on the nonlinear structural system. The displacement response used in the recognition is calculated by the Newark-β method. Lourens et al. (2012) used the improved Kalman filter method to identify the dynamic load acting on the structure. Compared with the work of Ma and Ho (2004), the difference is that he treats the noise as a random process. And the feasibility of the method is verified by experiments.

The stochastic method is a method to study the dynamic load identification problem from the perspective of probability and statistics. It is mainly applied to the identification of random dynamic loads. Since stochastic dynamic loads are more complex than other types of dynamic

loads, there are relatively few literatures on the study of stochastic dynamic load identification. Lin et al. (2001) firstly used the inverse virtual excitation method to identify the stochastic dynamic load on the structure. He decomposes the power spectral density matrix of the vibration response, and then obtains the virtual harmonic response by constructing the virtual excitation to identify the power spectral density matrix of the random dynamic load. Although the inverse virtual excitation method can improve the recognition accuracy of random dynamic load to a certain extent, it still encounters the inverse operation of the frequency response function matrix. For this reason, the researchers introduce a weighting matrix and change the frequency response function through the weighting matrix.

Artificial intelligence is a new subject emerging in the 1950s. Its main function is to use artificial intelligence systems to simulate the human brain's ability to solve, reason and learn problems. It involves knowledge of multiple subject areas. The artificial intelligence methods for dynamic load identification mainly include genetic algorithm, support vector machine, neural network algorithm and so on. Sofyan (2000) proposed a feedforward back propagation (BP) neural network to identify the aerodynamic loads acting on the thin plate and developed a set of software capable of identifying multiple types of dynamic loads. Sha (2005) used BP neural network and radial basis function neural network to identify different types of dynamic loads respectively. The recognition results show that BP neural network pairs based on Levenberg-Marquardt optimization algorithm is better than BP neural network and radial basis function neural network with additional momentum method. Although the artificial neural network based dynamic load identification method has greater application potential than the traditional dynamic load identification method, there are also many problems, such as the selection of the network model, the number of hidden layers, and the selection of the number of hidden nodes. There is no practical ubiquitous algorithm, and the user needs to make a trial to determine.

2.2.2 Impact load identification

Information of the impact force acting on civil structures is essential for their loading condition assessment, health monitoring, and structural reliability design (Jia et al. 2015; Khanam et al. 2015; LeClerc et al. 2007; Park, Ha, et al. 2009). For instance, it is important to quantify impact events such as debris impact, ice strike, falling stone and dropping tool attacking the air foil and the wind turbine blade, likely leading to structural damage. However, in such situations, the direct measurement of these impact forces is infeasible because of the inaccessible installation of force transducers. Force identification is a typical ill-posed inverse problem, where the measured responses are employed to determine the external force, and many methods have been developed in the past three decades. In the context of inverse problems, the small noise in the observed responses may induce a large oscillation of the solution. Therefore, regularisation methods are widely used to stabilise the solution due to the measurement noise and/or the modelling error.

Tikhonov regularisation and truncated singular value decomposition (TSVD) are two popular techniques for force identification. Jacquelin et al. (2003) compared the performance of the Tikhonov regularisation and TSVD techniques for reconstructing the time history of the impact force acting on an aluminium plate in time domain. TSVD is to reduce the rank-deficient of the system transfer matrix like a low-pass filter and it is efficient to solve the problem due to high frequency components. The regularisation technique is to stabilise the solution in global. Kalhori, Alamdari, et al. (2018) applied the Tikhonov regularisation method for reconstructing the time history and localization of the impact force acting on a composite panel. Jia et al. (2015) proposed a weighted Tikhonov regularisation method for identifying random dynamic force in the frequency domain, where the weighting matrix depends on the frequency response function. Jayalakshmi et al. (2018) presented a modified Tikhonov method to reconstruct the dynamic force from measurements of several sensors, which was numerically verified using a

shear building model. The Tikhonov method used above is known as l_2-norm regularisation. The identified forces obtained by the classical l_2-norm regularisation methods are smooth, meaning that the significant values not only distribute in the pulse profile of the impact force but also in the unloading interval (Qiao et al. 2016). Although this reconstructed accuracy might be barely satisfactory for a high-damping system (Huang et al. 2021), the method based on the classical l_2-norm regularisation technique would not be suitable for the impact force identification.

Recently, sparse regularisation has received considerable interest on the field of signal recovery. For the inverse problem of dynamic force identification, the l_1-norm regularisation as the standard sparse regularisation is widely used. In the Bayesian framework, Samagassi et al. (2015) applied a relevance vector machine approach based on Daubechies wavelet and l_1-norm penalty for reconstructing multiple impact forces acting on a beam. Qiao, Liu, et al. (2019) proposed an enhanced sparse regularisation method for impact force identification based on the reweighted l_1-norm minimization. To consider the intrinsic structure of the impact force that nonzero elements occur in groups, the sparse group regularisation method based on minimizing the mixed $l_{2,1}$-norm is proposed for the impact force identification (Qiao, Mao, et al. 2019). Liu et al. (2020) developed a novel sparse regularisation method with a generalized minimax-concave (GMC) penalty to deal with the impact force identification problem. Combining the redundant dictionary, the sparse regularisation can also be applied for the moving load identification. Zhong et al. (2019) used a sparse regularisation approach for traffic load monitoring based on the analytical model and redundant dictionary. To seek more sparse and accurate solution of impact force identification, the nonconvex sparse regularisation method (Liu et al. 2022; Qiao et al. 2020) is proposed to recover the time history of impact forces. All the above studies, the location of the impact force is known.

In practice, the impact force excitation locations are unknown, which will introduce another challenge for the force identification problem. Wang and Chiu (2003) expressed the amplitude and the location of the unknown impact forces as two variables of the structural response and they are identified by minimising the difference of the predict and measured responses. Li and Lu (2016) proposed a method for the localization and identification of the impact force. The location of the impact force is first determined with an error functional indicator and then a constrained optimization algorithm is used to identify the impact force time-history. Wambacq et al. (2019) presented an algorithm to localise and identify forces in the frequency domain. Group sparse feature is an important specific feature for external force and has been used for the force localization and identification. Feng et al. (2021) utilized the external force group sparse feature and developed an original time domain group sparsity regularisation method, named Group Relevance Vector Machine, to localise and reconstruct external forces on structures based on structure responses only. Liu et al. (2022) also used the force vector group sparse feature and proposed an impact force identification method based on the nonconvex overlapping group sparsity (NOGS), allowing to localise the impact and recover its time history simultaneously from quite limited measurements.

As above, during the force identification process, the transfer matrix construction has a big influence on the identification results. There are several methods to construct the transfer matrix, e.g., the mode superposition method, the state space function method, the unit impulse response function method, etc. The constructed transfer matrix using these methods is a lower triangular Toeplitz matrix, and strong correlations exist among the adjacent columns in this kind matrix. When there are several nonzero elements in the excitation time interval, the sparse regularisation method cannot identify the force value directly. For the impact force identification, there are some prior information of the impact force such as the short time interval, the excitation time from the response and its sparse location. To eliminate the effect

of the unloading interval, the transfer matrix could be truncated with specific features that corresponds to the short time interval of the impact force. In this way, an accurately and efficiently identified force could be obtained.

2.2.3 Moving load identification

Moving loads acting on bridge play a very important role on the bridge design, condition assessment of bridge and the control of transportation network (Yu, Cai, et al. 2016; Zhu and Law 2015). However, in practice, it is difficult to directly measure the dynamic loads due to the limitation of technology or the working environment. Therefore, it would be beneficial to develop the indirect identification method.

In the past several decades, many researchers have developed some indirect methods to measure the moving loads from the bridge responses (Chan et al. 1999; Law et al. 1997; Wang and Qu 2011; Wu and Shi 2006; Yu and Chan 2007; Zhu and Law 2000; Zhu et al. 2006). These techniques can effectively identify moving forces from structural responses through the relationship between moving forces and responses. Early studies of moving force identification (MFI) focus on the establishment of the identified equations. Further studies about MFI focus on how to identify moving forces accurately under the influence of measurement noises. Okubo et al. (1985) investigated the effect of the measurement noise on the inversion process. Due to the ill-conditioned frequency response function (FRF) matrix at frequencies at the structural resonances, the noise involving in measurement responses, even a minor error, can result in highly ill-posed and destroy badly the stability and accuracy of identifying loads. Therefore, in the processes of MFI, the ill-posed problem is an important issue that must be solved. Many techniques have been developed to improve this problem. Among these techniques, regularisation techniques have been widely applied in the MFI field. Many researchers adopted Tikhonov regularisation and truncated singular value decomposition (TSVD) to reduce the effect of noises (Chen and Chan 2017; Chen et al. 2020; Law et al. 2001; Pan et al. 2017; Zhu

and Law 2002; Zhu and Law 2003). Law et al. (2001) firstly introduced Tikhonov regularisation into time domain to identify the moving force. Subsequently, Zhu and Law (2001) applied this method to identify moving loads on a continuous beam. Because of expensive matrix computation, this method was later improved with a new formulation where the large matrices in the analytical formulation are expressed as combination of a number of smaller matrices (Zhu and Law 2002). Application of this regularisation method to a real bridge–vehicle system was also studied with consideration of the road surface roughness and incomplete vehicle speed information. Chen et al. (2020) proposed a truncated generalized singular value decomposition method for identifying the moving force. Due to the low sensitivity of structural responses to the forces at these zone where the moving forces enter into and exit a bridge deck, Pan et al. (2017) proposed a moving average Tikhonov regularisation method for MFI to improve the identification accuracy. However, most existing methods on moving force identification are usually based on modal decomposition and are subject to modal truncation error in the dynamic responses. The above methods are all based on the continuous system and modal superposition technique, and they cannot be applied to complicated structure.

2.3 VBI based structural damage detection

Bridge health monitoring based on VBI allows the structures to be monitored or assessed under operating conditions. Many approaches based on the VBI system have been developed over the past decade and these structural damage detection approaches can be divided into three categories (Zhu and Law 2016): (1) damage detection based on bridge responses; (2) damage detection based on vehicle responses; (3) damage detection based on both vehicle and bridge responses.

2.3.1 Damage detection based on bridge responses

Structural parameter identification based only on the dynamic response of the bridge subjected to the traffic excitations can be used to the damage assessment. In early research, most of bridge

damage detection methods are based on the change of modal parameters such as frequency, mode shape, damping and frequency response function, etc. Subsequently, in order to detect the local damage effectively, scholars proposed some mode shape related parameters such as modal assurance criterion (MAC), coordinate modal assurance criterion (COMAC), flexibility, mode shape derivatives and phase space topology, etc. The VBI system is time-varying and the modal parameter change with the vehicle position due to the combined effect of the local damage and the presence of the moving vehicle. The change of the instantaneous modal parameter could be regarded as damage indicator for the bridge structure. Mazurek and DeWolf (1990) conducted laboratory studies on simple two-span girders under moving vehicular loads with structural deterioration by vibration analysis. Structural damages were artificially introduced by a release of supports and insertion of cracks and detected by the changes of the resonant frequencies and mode shapes of the bridge. Law and Zhu (2004) defined two parameters on this frequency variation: the relative frequency change (RFC) and the absolute frequency change (AFC). The AFC was compared with the natural frequency of the intact bridge and the RFC was compared with that of the damaged bridge. The RFC and AFC vary when the vehicle is moving on the bridge. They are sensitive to the weight of the moving vehicle, and the frequency ratio between the vehicle and bridge has also some effect on the RFC and AFC. They are very sensitive to damage in the bridge structure including the effect of the breathing crack. The RFC would be a useful parameter in damage detection of the bridge structure, while the AFC is dependent on a baseline reference and the load position. Lee et al. (2002) identified the operational modal properties of a bridge structure using vibration data caused by traffic loadings, and the subsequent damage assessment was based on the estimated modal parameters and the neural networks technique. Feng and Feng (2016) proposed a bridge damage detection procedure that utilizes vehicle-induced displacement response of the bridge, particularly, the curvature of the first mode shape, without requiring prior knowledge about the

traffic excitation and road roughness. The first mode shape was extracted by directly analysing the power spectral density functions of measured bridge displacement responses under vehicle excitations. There also exist a lot of modal-based damage indicators for general structural damage detection and they could be applied to the detection of the VBI system.

The vehicle is continued passing the bridge and the bridge response has a discontinuity when the vehicle is passing over the damage. Recently, advanced signal processing techniques such as wavelet transform, Hilbert-Huang transform (HHT) etc. are used to extract the discontinuity. An approach to make use of this relationship from the operational deflection time history of a bridge subjected to a moving vehicular load using the continuous wavelet transform was proposed for the first time (Zhu and Law 2006). The identification of crack damages in a beam is based on the spatial wavelet analysis of the response measurement at one point of the bridge deck. The location is determined as the position of the dip in the wavelet coefficient curve and there is no baseline requirement in determining the damage location. The damage index based on wavelet coefficient is used as an indicator of the damage extent. Later on, Khorram et al. (2012) also used the maximum value of wavelet coefficient at the point of cracks as the damage index and the important parameters which affect the damage index were found using factorial design. In addition to the wavelet coefficient of the operational deflection, Yu, Xia, et al. (2016) used the Lipschitz exponent to indicate the damage extent. He and Zhu (2016) also presented an algorithm to separate the dynamic responses into those associated with the vehicle motion and those associated with the beam motion. The results showed that the moving-frequency component is a promising indicator of damage location when the speed of the moving load is low and the number of damage locations is limited.

The velocity, acceleration and strain signals have also used to detect damage of bridges subjected to moving loads. An experimental study has been carried out on a beam-vehicle interaction system, and the corresponding distortions of wavelet coefficients of the measured

strain due to the presence of various levels of damage were identified in the phase space (Pakrashi et al. 2009). Zhang, Lie, et al. (2013) also used the velocity response of the simply-supported beam subject to a moving load to extract the damage feature. Li and Hao (2015) carried out an experimental study to identify damage of the shear connection in a composite beam subjected to moving loads using the relative displacement measurements. The results show that the relative displacement is more sensitive to damage in the shear connectors in composite bridges than other measurements.

The Hilbert-Huang transform (HHT) is another advanced signal processing technique for analysing non-stationary and nonlinear signals. The HHT includes two parts: the empirical mode decomposition (EMD) and the Hilbert spectral analysis. With the EMD's initial processing, the data can be decomposed into a finite set of intrinsic mode functions (IMFs). Huang et al. (2005) proposed two damage features for monitoring the health of the bridge structure subjected to moving vehicles: the nonlinear characteristics from employing the light and heavy loads and the frequency shift. Roveri and Carcaterra (2012) also utilized the HHT to identify the presence and location of damages for bridges under a traveling load, based on a single point measurement of the bridge. The effect of ambient noise was also taken into account. Damage location is revealed by direct inspection of the first instantaneous frequency generated by the HHT, which shows a sharp crest at the damaged section. Hester and González (2014) showed that the area under the filtered acceleration response of the bridge increases with increasing damage, even at highway load speeds. Once a datum reading is established, the area under subsequent readings can be monitored and compared with the baseline reading, as an increase in the area may indicate the presence of damage. The sensitivity to road roughness and noise was tested for several damage scenarios, with damage successfully identified in favourable scenarios. Li and Hao (2015) investigated the damage of shear connectors in a composite bridge model under moving loads by the relative displacements processed by the

continuous wavelet transform and Hilbert–Huang transform. Both the numerical and experimental results indicated that both relative displacements and accelerations can be used to identify the location and occurrence damage in shear connectors when the bridge is under moving loads, but the relative displacement is a better quantity for structural health monitoring of composite bridges.

2.3.2 Damage detection based on vehicle responses

The indirect bridge monitoring approach has received a great attention recently. The bridge damage is identified from the measured response of a passing vehicle. Many methods have been developed in the last decade. Previous investigations have focused on the extraction of bridge frequencies from vehicle measurements. The vehicle operates as an exciter of bridge frequencies and the vehicle also receives the bridge vibrations. Theoretical investigations show that, when tracked over a long period, this information could act as a useful reference for determining the degradation in stiffness or strength in the structure (Yang et al. 2004). Experimental work by the same research group using a cart fitted with accelerometers towed behind a light commercial truck corroborates the findings of their earlier theoretical study (Lin and Yang 2005). A follow up theoretical study by the same authors examines the relative influence of the various dynamic parameters of the system on correctly identifying the bridge frequencies of concern (Yang and Chang 2009), and a subsequent study looked at the effectiveness of different filtering methods to identify bridge frequencies (Yang et al. 2013). Other authors have validated their drive-by algorithms via scaled laboratory experiments. It must be noted that the level of resolution of the spectrum is related to the time that the vehicle is on the bridge, i.e., frequencies cannot be predicted accurately at high traffic speeds, and sufficient level of bridge excitation is needed (Keenahan and O'Brien 2014). Rather than using only changes in bridge frequency as a potential damage indicator, vehicle measurements are used by Kim et al. (2014), González et al. (2012) and Keenahan et al. (2013) to track changes

in structural damping, by Yang et al. (2014) and Oshima et al. (2014) to extract mode shapes and by Zhu et al. (2018) to reconstruct the interaction force, which can be subsequently employed for damage detection similarly to bridge SHM. In addition to dynamic characteristics of the bridge, McGetrick et al. (2015) and Obrien et al. (2014) demonstrate that a static mechanical property such as global stiffness can also be obtained from the vehicle response and used for damage detection purposes.

Using numerical simulations, Nguyen and Tran (2010) are some of the first researchers to show that in principle drive-by systems can not only be used for identifying global damages (by tracking parameters such as frequencies or damping), but also localised damage. In particular, they analyse the body displacement experienced by a 2-axle vehicle crossing a beam using wavelets and they observe that small peaks in the wavelet coefficients occur as each axle crosses the damaged section of the beam. In more recent work, Zhang et al. (2013) use the acceleration response of a vehicle (as it crosses the beam) to identify the location of damage in the beam. The method they use to identify damage is based on using operational deflected shape curvature and they demonstrate the effectiveness of the approach using both numerical simulations and experimental testing. Both authors (Nguyen and Tran 2010; Zhang, Lie, et al. 2013) report deterioration in their results as the speed of the vehicle increases. Keenahan and O'Brien (2014) proposed an optimization approach to overcome the challenges of short signals collected from the moving vehicle and the nonlinear nature of the drive-by system. In spite of all advances in indirect bridge monitoring using passing vehicles, a recent review by Malekjafarian et al. (2015) concludes that further investigations on the impact of vehicle speeds, noise and rough road profiles are needed before drive-by systems can be successfully implemented in practise. Hester and González (2017) examined the theoretical feasibility and practical limitation of a drive-by system in identifying damage due to localised stiffness loss. They divided the total vehicle response into the static, dynamic, and damage components for

bridges with a damage. By comparing the effect of the damage component with other effects such as vehicle speed, road profile and noise on a wavelet contour plot, the workable frequency range was identified. The algorithm used the specific frequency bands to improve the sensitivity to damage. Recommendations on selection of the mother wavelet and frequency band were provided, together with discussions on the impact of noise, road profile and periodic measurements. Yang and Yang (2018) reviewed that indirect approach for modal identification and damage detection of bridges, when maturely developed, possesses the advantages of mobility, efficiency, economy and simplicity, compared with the conventional direct approach.

2.3.3 Damage detection based on both vehicle and bridge responses

With the advancement of wireless telecommunication and sensor networks, the VBI information can be captured by permanent wireless sensors on the bridge and the mobile sensory system on the passing vehicle. Bridge structural damage is identified from both vehicle and bridge responses. Majumder and Manohar (2004) consider the problem of damage detection in beam structures using vibration data from vehicle and bridge. A time domain structural damage detection scheme, within finite element modelling framework, that takes into account time varying structural matrices, structural nonlinearities and spatial incompleteness of measured data, is developed. Kim et al. (2014) presented a vibration-based health monitoring strategy for short span bridges utilizing an inspection vehicle. The feasibility of the strategy was investigated through a scaled laboratory experiment using a two-axle vehicle. Both the vehicle and bridge responses were measured either separately or together. The results indicated that the natural frequency and changes in damping of the bridge can be detected. The possibility of diagnosis of the damage location and severity of bridges by comparing patterns of identified bridge dynamic parameters through periodical monitoring was also observed.

2.4 Bridge local damage detection

The main purpose of SHM is to classify the performance of structures and facilitate their maintenance during their service life. SHM includes identifying the characteristics and behaviour of undamaged and damaged structures and specifying the location of the damage. Most research assume the damage as global damage which could be detected using traditional vibration-based method. However, when it comes to local damage such as composite beam shear connector damage and bridge cable damage, these methods are usually not suitable in practical applications. The following is reviewing work for these two damage cases.

2.4.1 Composite beam shear connector damage detection

Steel-concrete composite beams have been widely applied in bridges. Shear connectors are used to connect the concrete slab and steel girder and transfer the longitudinal shear forces at the steel-concrete interface. Deterioration or failure of the shear connectors will affect the horizontal shear resistance, and therefore reduce the bridge load-carrying capacity. The damage on the shear connectors causes shear slip between concrete and steel, resulting in a stiffness degradation of 17% in short-span bridge (Nie and Cai 2003). Hence monitoring shear connectors health plays an important role in guaranteeing structural safety and retrofitting/strengthening composite structures.

Recently, structural damage detection for shear connection systems has attracted the interests of many researchers, and some investigations have been conducted using vibration measurements. Vibration-based damage detection methods have been used for the condition assessment of shear connectors in composite bridges. It has been found that the bridge global vibration parameters such as frequencies, mode shapes, and their derivatives are not sensitive to changes in shear connector condition (Xia et al. 2007). The local damage detection methods using different signal processing techniques have been developed for composite structures. Ren et al. (2008) proposed a signal-based damage detection method in which the damage features

characterized by the wavelet packet energy changes was applied for structural damage identification of the shear connection system. Zhu et al. (2012) used wavelet-based Kullback-Leibler distance (KLD) to assess the integrity of the shear connectors. Li, Hao, et al. (2014) proposed a dynamic damage detection approach based on the wavelet packet energy of cross-correlation functions from ambient vibration measurements to identify the damage of shear connectors in slab-on-girder bridges. Tan et al. (2020) applied a procedure for detecting damage in a composite slab-on-girder bridge structure, using vibration characteristics and Artificial Neural Network. Fang et al. (2020) used both model-based and non-model-based methods to detect the occurrence, location, and extent of the damage in the steel-concrete composite slab. However, these vibration-based methods would require a number of measurements on the slab and girders, and still have a big challenge to accurately detect the damage in the shear connection system.

Damage or failure of shear connectors results in shear slippage and hence the relative displacement between girders and slab could be an damage indicator of the shear connection system if the applied load is large enough to overcome the friction force between the girders and slab (Li and Hao 2015). As the relative displacement is directly related to the shear connector conditions, it is believed to be more sensitive than other response quantities such as acceleration and deformation. In recent years, non-contact displacement sensors such as GPS (Yi et al. 2013), laser Doppler vibrometer (Nassif et al. 2005), microwave interferometer (Bartoli et al. 2008), digital image processing, and Linear variable differential transformer (LVDT) (Zheng et al. 2014) have been employed in structural health monitoring. However, these methods are not suitable for monitoring during the whole bridge life cycle. A new applicable measurement for composite slab-on-girder bridge needs to be developed for practical applications.

To overcome the limitation of relative displacement measurement methods and vibration-based approaches to access the shear connection in composite bridges, Li et al. (2015) developed an innovative relative displacement sensor to directly measure the relative displacement between the slab and girder in composite bridges. Continuous wavelet transform (CWT) and HHT were used to analyse the measured dynamic responses and to identify the damage of shear connectors in a composite bridge model under moving loads (Li and Hao 2015). The results demonstrate that relative displacement is a better response quantity for structural health monitoring of composite bridges. However, the sensor developed by Li et al. (2015) will be affected by tension/compression, bending, and torsion due to the complicated loading condition on the structure.

2.4.2 Bridge cable damage detection

Cable-stayed bridges are widely used all around the world. In this type of bridges, cables play the critical role to transmit the force from the deck to the pylons and into the foundation. However, in practice, the cables are prone to deterioration and damage because of fatigue and corrosion (Mehrabi 2006; Sun et al. 2013). Compared with other bridge components in the cable-stayed bridge, the cable is more vulnerable and usually has a shorter life. Therefore, in order to obtain the cable service state and ensure the safety in bridge operation, cable monitoring has become an indispensable part of structural health monitoring (SHM) for cable-stayed bridges (Dong et al. 2018).

Currently, the cable monitoring approaches including direct and indirect methods have been applied in cable-stayed bridges. Cable forces are usually considered as a significant safety indicator in monitoring process. In direct methods, cable tension forces can be obtained directly. Li et al. (2009) applied a fabrication procedure of the smart stay cable with fiber Bragg grating (FBG) sensors to directly measure the cable tension force of the Tianjin Yonghe Bridge. The cable tension was directly weighted by Carrión et al. (2017) with a hydraulic jack from the

bottom of the lower anchoring of a cable that pulls the cable until it is released from the deck and all the tensile force is supported by the jack. In addition, the cable responses, such as cable strains, acceleration etc. can also be used to obtain the cable tension forces in direct methods. Based on cable responses, some model-based and data-driven identification methods for cable tension force have been proposed. Li, Zhang, et al. (2014) used an extended Kalman filter (EKF) to identify the time varying cable tension force based on the acceleration of a cable. Yang et al. (2016) proposed a data-driven identification algorithm for time varying cable tension force by using blind source separation. Some researchers also studied the relationship between the tension force and the natural frequencies of the cable, which was used to evaluate the cable tension by (Sim et al. 2013), (Cho et al. 2010) and (Arjomandi et al. 2019). Huang et al. (2018) used the real-time frequency of the cable from the measured acceleration based on the Hilbert-Huang Transform to calculate the real-time cable tension. Influence lines can also be integrated with long-term monitoring data to determine the proportionality coefficient between the maximum and minimum recorded cable forces, Ren et al. (2019) used this method to extract dead load–induced cable forces under random vehicle loadings. In recent years, some researchers utilize image processing techniques to estimate the cable force. A vision-based monitoring system to estimate the tensile force of stay cables during traffic use was developed by Kim et al. (2013), and a remotely controllable pan-tilt drive was installed in the developed vision-based monitoring system to estimate the forces on multiple cables using a single system. A vision-based monitoring system to a cable-stayed bridge in traffic use and to verify the possibility of the system under various weather conditions to estimate the cable tensions was also applied by Kim et al. (2017). Although these direct methods can obtain the cable tension forces, they also have some limitations. For instance, the method based on the cable fundamental vibration frequency is limited to long cables. The weak survivability and high cost of the smart cables with FBG-fibre make it not widely used. Image processing-based method

is greatly affected by weather conditions. Therefore, to overcome these shortcomings, some researchers seek to indirect methods.

In recent years, some indirect methods utilizing bridge deck strains, deck deflections, vertical dynamic displacements, deck shear forces, rotation influence lines to monitor the cable state have been developed. A new method of detecting multiple simultaneous damages, including cable tension loss and deck damage, in a cable-stayed bridge by use of the analysis of the vertical dynamic response of a vehicle passing the bridge was presented (Yin and Tang 2011). The distributed measurement of strains along the bridge deck to detect the cables that have totally or partially lost their tensile forces, and the change in support reactions to localise and quantify the damage in the cables were used (Nazarian, Ansari and Azari 2016; Nazarian, Ansari, Zhang, et al. 2016). The partial cable damage using the abnormal variation of temperature-induced deck deflection caused by cable damage was localised and quantified (Wang and Ye 2019). A new cable damage identification technique based on the concept of rotation influence line (*RIL*) at the bridge bearing locations, and solely relies on measurements obtained from two points at either end of the bridge e.g., RIL_R and RIL_L was proposed by Alamdari et al. (2019). It is found that the cable damage state will affect the bridge responses whether the bridge is under dead loads or live loads or temperature changes, and these indirect methods can identify the cable damage and bridge deck damage simultaneously. However, few researchers regard the problem of cable damage identification as a problem of classification and regression.

2.5 Simultaneous identification of structural load and damage

In recent years, only the use of structural dynamic response to identify loads and unknown parameters has gradually developed. Different algorithms have been proposed to address this inverse problem. The most common algorithms are based on the least-squares method or Kalman filtering. Zhu and Law (2007) proposed a method for simultaneous identification of

the interaction force time histories and structural parameters iteratively using a two-step identification procedure with responses of the bridge subjected to moving vehicular loads that serve as input. Prior knowledge of the moving loads is not required. The method was later extended for the structural condition assessment of a three-span box-section concrete bridge deck subject to a three-dimensional moving vehicle (Law and Li 2010). The response sensitivity-based method was used to identify the interaction forces and bridge parameters simultaneously in an iterative manner. It was found that a sufficient number of sensors may be required to ensure an over-determined set of identification equations for simultaneous identification of the interaction forces and system parameters. It is also noted that the accuracy of the identified moving loads may have a large influence on the identification accuracy of the structural damage. Huang et al. (2009) developed a new algorithm, referred to as the adaptive quadratic sum–squares error with unknown excitations (AQSSE-UI) by minimizing the quadratic sum–squares error between the measured response and the theoretical values. The characteristics of damage and moving loads in a concrete slab bridge were estimated using a hybrid genetic algorithm from the bridge responses (Park, Noh, et al. 2009). Zhang et al. (2010) solved the problem of the composite identification of the load and parameters based on the virtual distortion method. This method was later extended to the identification of a multiple degrees-of-freedom vehicle model (Zhang, Jankowski, et al. 2013). Lu and Liu (2011) presented an iterative technique for identifying both the bridge damages and vehicle parameters based on the bridge dynamic response using the penalty function method with regularisation. The effects of measurement noise, different vehicle models, measurement time duration and modelling error on the identification results were investigated in the numerical simulation. It was shown that the proposed method has the potential for real application for damage detection and parameter identification.

A Kalman filter with unknown inputs (KF-UI) approach is derived with the weighted least-squares estimation method to investigate the joint input and state estimation by Pan et al. (2010). Subsequently, Lei et al. (2012) proposed an algorithm based on sequential application of an extended Kalman estimator for the extended state vector of a structure and least-squares estimation of its unknown external excitations. Abdullah and Achintya (2015) integrates the iterative least squares technique and the unscented Kalman filter (UKF) concept to develop a novel structural health assessment technique. The integrated procedure significantly improves the basic UKF concept.

Although most of the methods mentioned earlier yield a good estimate of force and system parameters, when the complete time history response of the structure is available, they perform rather poorly, when response measurements are not available at all locations. Apart from this limitation, Kalman filter and ILSE involve a large number of time-consuming iterations. Keeping these things in view, recently, metaheuristic algorithms like genetic algorithms, swarm intelligence algorithms are being popularly used for system parametric identification of practical engineering structures. Sun and Betti (2014) presented a hybrid heuristic optimization strategy based on the artificial bee colony (ABC) algorithm with a local search operator. The damage distribution is modelled as a modified form of the bivariate Gaussian distribution function (Noh and Lee 2013). Feng et al. (2015) proposed a new method to identify structural parameters and vehicle dynamic axle loads of a vehicle–ridge interaction system in the framework of an iterative parametric optimization process. A Bayesian inference regularisation is presented to solve the ill-posed least-squares problem. Pioldi and Rizzi (2016) proposed a new element-level system identification and input estimation technique named full dynamic compound inverse method (FDCIM). A statistical average technique, a modification process, and a parameter projection strategy are adopted at each stage to achieve stronger convergence.

Jayalakshmi and Rao (2017) used a newly developed dynamic hybrid adaptive firefly algorithm (DHAFA) to solve the inverse problem associated with the system identification.

2.6 Summary

This chapter provided an overview of the field of load identification and damage detection. The following research gaps have been found,

1) In terms of load identification, the impact force excitation locations are unknown, which will introduce another challenge for the force identification problem. This makes existing impact force identification methods greatly restricted in terms of practical applications. Therefore, it is necessary to study the problem of impact force identification under the unknown locations and develop new method for impact load identification.
2) Most existing methods on moving force identification are usually based on modal decomposition and are subject to modal truncation error in the dynamic responses. These methods are all based on the continuous system and modal superposition technique, and they cannot be applied to complicated structure. To solve this problem, an attempt is made to identify the moving vehicle load via equivalent nodal force.
3) With regard to damage detection, for steel-concrete composite beams, the vibration-based methods would require a number of measurements, and still have a big challenge to accurately detect the damage in the shear connection system. Damage or failure of shear connectors results in shear slippage and hence the relative displacement between girders and slab could be an damage indicator of the shear connection system. However, these methods are not suitable for monitoring during the whole bridge life cycle. A new applicable measurement for composite slab-on-girder bridge needs to be developed for practical applications.
4) In addition, many indicators have been proposed for detecting the bridge local damage such as cable damage. But the interrelationship of the indicators and their respective sensitivity

relative to the damage severity and damage location have not yet taken into account together to improve the effectiveness and efficiency of damage detection.

Chapter 3 Impact force identification based on truncated transfer matrix

3.1 Overview

This chapter proposes a novel hybrid approach by integrating the truncated transfer matrix-based regularisation method for the impact force value identification and the sparse regularisation method for the force location identification. It is organized as follows. Section 3.2 presents the governing equation of the impact force value and location identification. In Section 3.3, the truncated transfer matrix-based regularisation identification method is depicted and compared with the standard l_1-norm and classical l_2-norm regularisation techniques. Numerical and experimental validation are presented in Sections 3.4 and 3.5. Finally, several conclusions are drawn in Section 3.6.

3.2 Theory

3.2.1 Impact force identification

A simple supported Euler-Bernoulli beam is subjected an impact force and the excitation location is unknown. The beam is assumed to be of constant cross section with uniform mass per unit length, and have a linear, viscous proportional damping. The effects of shear deformation and rotary inertia are neglected. The dynamic governing equation is given as (Zhu and Law, 2016):

$$\boldsymbol{M}\ddot{\boldsymbol{x}}(t) + \boldsymbol{C}\dot{\boldsymbol{x}}(t) + \boldsymbol{K}\boldsymbol{x}(t) = \boldsymbol{L}\boldsymbol{F}(t) \tag{3.1}$$

where $\boldsymbol{M}$, $\boldsymbol{C}$ and $\boldsymbol{K}$ are the mass, damping, stiffness matrices, respectively. $\ddot{\boldsymbol{x}}(t)$, $\dot{\boldsymbol{x}}(t)$ and $\boldsymbol{x}(t)$ are the acceleration, velocity and displacement vectors of the beam, respectively. $\boldsymbol{F}(t)$ is the

input force vector, and $\boldsymbol{L}$ is the mapping matrix for the input. Based on modal superposition, the dynamic response $\boldsymbol{x}(t)$ can be obtained as,

$$\boldsymbol{x}(t) = \sum_{r=1}^{n} \boldsymbol{\Phi}_r \, q_r(t) \tag{3.2}$$

$$\boldsymbol{\Phi} = [\boldsymbol{\Phi}_1 \;\; \boldsymbol{\Phi}_2 \;\cdots\; \boldsymbol{\Phi}_n] = \begin{bmatrix} \varphi_{1,1} & \varphi_{2,1} & \cdots & \varphi_{n,1} \\ \varphi_{1,2} & \varphi_{2,2} & \cdots & \varphi_{n,2} \\ \vdots & \vdots & \ddots & \vdots \\ \varphi_{1,m} & \varphi_{2,m} & \cdots & \varphi_{n,m} \end{bmatrix} \tag{3.3}$$

where $\boldsymbol{\Phi}$ is the mode shape of the beam. $\boldsymbol{q}(t)$ is the modal coordinate. r is the r^{th} vibration mode. m is the m^{th} vibration node.

Substituting Eq. (3.2) into Eq. (3.1), and multiplying by $\boldsymbol{\Phi}^T$, and applying the orthogonality conditions, we obtain

$$M_r \ddot{q_r}(t) + C_r \dot{q_r}(t) + K_r q_r(t) = f_r(t), \, (r = 1, \cdots, n) \tag{3.4}$$

Where $M_r = {\boldsymbol{\Phi}_r}^T \boldsymbol{M} \boldsymbol{\Phi}_r$, $C_r = {\boldsymbol{\Phi}_r}^T \boldsymbol{C} \boldsymbol{\Phi}_r$, , $K_r = {\boldsymbol{\Phi}_r}^T \boldsymbol{K} \boldsymbol{\Phi}_r$, and $f_r(t) = {\boldsymbol{\Phi}_r}^T \boldsymbol{L} \boldsymbol{F}(t)$, are the modal mass, modal damping, modal stiffness, and modal force, respectively. n is the number of the vibration modes.

Eq. (3.4) is also expressed as,

$$\ddot{q_r}(t) + 2\xi_r \omega_r \dot{q_r}(t) + {\omega_r}^2 q_r(t) = \frac{f_r(t)}{M_r}, \, (r = 1, \cdots, n) \tag{3.5}$$

where ${\omega_r}^2 = \frac{K_r}{M_r}$, $\xi_r = \frac{C_r}{2\omega_r M_r}$ denotes the damping ratio for the r^{th} mode. Ignoring the initial responses, the solution of Eq. (3.5) can be obtained,

$$q_r(t) = \frac{1}{M_r \omega_{dr}} \int_0^t e^{-\xi_r \omega_r (t-\tau)} \, sin \, \omega_{dr}(t-\tau) \, f_r(\tau) d\tau \tag{3.6}$$

$$\ddot{q}_r(t) = \frac{1}{M_r \omega_{dr}} \int_0^t e^{-\xi_r \omega_r (t-\tau)} [\left({\xi_r}^2 {\omega_r}^2 - {\omega_{dr}}^2\right) sin \, \omega_{dr}(t-\tau) - 2\xi_r \omega_{dr} \omega_r cos \omega_{dr}(t - \tau)] f_r(\tau) d\tau \tag{3.7}$$

Where ω_r is the r^{th} natural circular frequency of the system. $\omega_{dr} = \omega_r \sqrt{1 - {\xi_r}^2}$ is the r^{th} actual vibration circle frequency of the system under the damping C_r.

Then the vibration displacements and accelerations in Eq. (3.1) can be obtained,

$$\boldsymbol{x}(t) = \sum_{r=1}^{n} \boldsymbol{\Phi}_r \, q_r(t) = \sum_{r=1}^{n} \frac{\boldsymbol{\Phi}_r \boldsymbol{\Phi}_r{}^T \boldsymbol{L}}{M_r \omega_{dr}} \int_0^t \boldsymbol{F}(t) e^{-\xi_r \omega_r (t-\tau)} \, sin\, \omega_{dr}(t-\tau) \, d\tau \tag{3.8}$$

$$\ddot{\boldsymbol{x}}(t) = \sum_{r=1}^{n} \frac{\boldsymbol{\Phi}_r \boldsymbol{\Phi}_r{}^T \boldsymbol{L}}{M_r \omega_{dr}} \int_0^t \boldsymbol{F}(t) e^{-\xi_r \omega_r (t-\tau)} [\left(\xi_r{}^2 \omega_r{}^2 - \omega_{dr}{}^2\right) sin\, \omega_{dr}(t-\tau) -$$

$$2\xi_r \omega_{dr} \omega_r cos \omega_{dr}(t-\tau)] \, d\tau \tag{3.9}$$

The acceleration expression could be simply expressed as follows:

$$\ddot{\boldsymbol{x}}(t) = \int_0^t \boldsymbol{R}(t-\tau) \boldsymbol{F}(t) d\tau \tag{3.10}$$

where $\boldsymbol{R}$ is the impulse response function matrix:

$$\boldsymbol{R}(t-\tau) = \sum_{r=1}^{n} \frac{\boldsymbol{\Phi}_r \boldsymbol{\Phi}_r{}^T \boldsymbol{L}}{M_r \omega_{dr}} e^{-\xi_r \omega_r (t-\tau)} [\left(\xi_r{}^2 \omega_r{}^2 - \omega_{dr}{}^2\right) sin\, \omega_{dr}(t-\tau)$$

$$- 2\xi_r \omega_{dr} \omega_r cos \omega_{dr}(t-\tau)] \tag{3.11}$$

By discretising, Eq. (3.10) can be written in the matrix convolution form in the time duration from t_1 to t_{nt} as follows:

$$\begin{Bmatrix} \ddot{\boldsymbol{x}}(t_1) \\ \ddot{\boldsymbol{x}}(t_2) \\ \vdots \\ \ddot{\boldsymbol{x}}(t_{nt}) \end{Bmatrix} = \Delta t \begin{bmatrix} \boldsymbol{R}(t_1) & \boldsymbol{0} & \cdots & \boldsymbol{0} \\ \boldsymbol{R}(t_2) & \boldsymbol{R}(t_1) & \cdots & \boldsymbol{0} \\ \vdots & \vdots & \ddots & \vdots \\ \boldsymbol{R}(t_{nt}) & \boldsymbol{R}(t_{nt-1}) & \cdots & \boldsymbol{R}(t_1) \end{bmatrix} \begin{Bmatrix} \boldsymbol{F}(t_1) \\ \boldsymbol{F}(t_2) \\ \vdots \\ \boldsymbol{F}(t_{nt}) \end{Bmatrix} \tag{3.12}$$

where nt is the number of time steps. Δt is time interval determined by sampling frequency. { } is the vector notation. The above equation form can be simplified into a matrix-vector form as:

$$\boldsymbol{A}_{(ns \times nt) \times 1} = \boldsymbol{H}_{(ns \times nt) \times (nl \times nt)} \boldsymbol{F}_{(nl \times nt) \times 1} \tag{3.13}$$

where $\boldsymbol{A}_{(ns \times nt) \times 1}$ is the accelerations response vector. ns is the number of measurement points. $\boldsymbol{F}_{(nl \times nt) \times 1}$ is the force vector to identify, nl is the number of force locations, and the transfer matrix $\boldsymbol{H}_{(ns \times nt) \times (nl \times nt)}$ is a lower triangular Toeplitz matrix.

In practice, the measurement noise always exists. The forward problem can be expressed as,

$$\boldsymbol{A} = \boldsymbol{H}\boldsymbol{F} + \boldsymbol{e} \tag{3.14}$$

where the vector $\boldsymbol{e}$ represents the inevitable measurement noise that corrupts the actual response $\boldsymbol{A}$.

The inverse problem is to reconstruct the impact force vector $\boldsymbol{F}$ from the acceleration response vector $\boldsymbol{A}$. To solve this inverse problem, the regularisation techniques can be used to stabilize the results of force identification. The regularisation method will be introduced in Section 3. In this inverse problem, the accelerations response vector is known, and the modes of the structural system could be extracted from the acceleration response. When the modes and load locations are known, the transfer matrix $\boldsymbol{H}$ can be obtained. While the load positions are unknown, they need to be determined firstly. Li and Lu (2016) proposed a constrained optimization method for impact localization and identification simultaneously. However, the global optimal location is not guaranteed using this method. And most existing research only identify a single impact force. In this study, a new method to extract the load position information from the modal forces is presented as below.

3.2.2 Impact force localization

The force location information has the sparse feature and that is embedded in the modal forces. A method using singular value decomposition and sparse regularisation is proposed to localise the forces.

The first step of this method is to obtain the modal force. Eq. (3.7) can be expressed as,

$$\ddot{q}_r(t) = \int_0^t \ddot{h}_r(t-\tau) f_r(\tau) d\tau \tag{3.15}$$

with

$$\ddot{h}_r(t) = \frac{1}{M_r \omega_{dr}} e^{-\xi_r \omega_r t}\left[\left({\xi_r}^2 {\omega_r}^2 - {\omega_{dr}}^2\right) sin\, \omega_{dr} t - 2\xi_r \omega_{dr} \omega_r cos \omega_{dr} t\right] \tag{3.16}$$

Eq. (3.15) can be discretized, leading to a set of algebraic equations as below,

$$\begin{bmatrix} \ddot{q}_r(t_1) \\ \ddot{q}_r(t_2) \\ \vdots \\ \ddot{q}_r(t_{nt-1}) \\ \ddot{q}_r(t_{nt}) \end{bmatrix} = \Delta t \begin{bmatrix} \ddot{\mathrm{h}}_\mathrm{r}(t_1) & 0 & \cdots & 0 & 0 \\ \ddot{\mathrm{h}}_\mathrm{r}(t_2) & \ddot{\mathrm{h}}_\mathrm{r}(t_1) & \cdots & 0 & 0 \\ \vdots & \vdots & \cdots & \vdots & \vdots \\ \ddot{\mathrm{h}}_\mathrm{r}(t_{nt-1}) & \ddot{\mathrm{h}}_\mathrm{r}(t_{nt-2}) & \cdots & \ddot{\mathrm{h}}_\mathrm{r}(t_1) & 0 \\ \ddot{\mathrm{h}}_\mathrm{r}(t_{nt}) & \ddot{\mathrm{h}}_\mathrm{r}(t_{nt-1}) & \cdots & \ddot{\mathrm{h}}_\mathrm{r}(t_2) & \ddot{\mathrm{h}}_\mathrm{r}(t_1) \end{bmatrix} \begin{bmatrix} f_r(t_1) \\ f_r(t_2) \\ \vdots \\ f_r(t_{nt-1}) \\ f_r(t_{nt}) \end{bmatrix} \quad (3.17)$$

Where nt is the number of time steps. Δt is time interval determined by sampling frequency. Eq. (3.17) can be written in a matrix form as,

$$\ddot{\boldsymbol{q}}_r = \ddot{\boldsymbol{H}}_r \boldsymbol{f}_r \text{ , } (r = 1, \cdots, n) \quad (3.18)$$

where $\ddot{\boldsymbol{q}}_r$ is the r^{th} mode amplitude vector. $\boldsymbol{f}_r$ is the r^{th} modal force vector and the r^{th} transfer matrix $\ddot{\boldsymbol{H}}_r \in \boldsymbol{R}^{nt \times nt}$ is a lower triangular Toeplitz matrix. $\ddot{\boldsymbol{q}}_r$ is extracted from the response using the mode superposition.

Based on the mode superposition method, the modal force can be derived as follows:

$$\boldsymbol{f}(t) = \boldsymbol{\Phi}^T \boldsymbol{L} \boldsymbol{F}(t) \quad (3.19)$$

where $\boldsymbol{f}(t) = [f_1(t)\ f_2(t) \cdots f_n(t)]^T$ is the modal force, and $f_r(t)$is the r$^{\text{th}}$ modal force. $\boldsymbol{L} = [\boldsymbol{L}_1\ \boldsymbol{L}_2\ \cdots \boldsymbol{L}_{nl}]$ is the mapping matrix. $\boldsymbol{L}_i = [0 \cdots 0\ 1\ 0 \cdots 0]^T$ is the i$^{\text{th}}$ force mapping vector, and the element value 1 represents the i$^{\text{th}}$ force location.

Eq. (3.19) can be discretised as,

$$\boldsymbol{f} = \sum_{i=1}^{nl} \boldsymbol{\Phi}^T \boldsymbol{L}_i \boldsymbol{F}_i \quad (3.20)$$

where $\boldsymbol{f} = [\boldsymbol{f}_1\ \boldsymbol{f}_2 \cdots \boldsymbol{f}_n]^T$ is the modal force matrix. $\boldsymbol{f}_r$ is the r^{th} modal force vector. As shown in Eq. (3.20), the force location information is embedded in the modal force matrix.

According to the sparse feature of the impact force, assuming each impact is not simultaneous and overlapped, the modal force matrix could also be separated to the following form based on the number of impact forces

$$\boldsymbol{f} = \left[\boldsymbol{f}_1^{'}\ \boldsymbol{f}_2^{'} \cdots \boldsymbol{f}_{nl}^{'}\right] \quad (3.21)$$

where $\boldsymbol{f}_i^{'}$ is the i^{th} impact force.

$$\boldsymbol{f}_i^{'} = \boldsymbol{\Phi}^T \boldsymbol{L}_i \boldsymbol{F}_i^{'} \text{ , } (i = 1, \cdots, nl) \quad (3.22)$$

where $\boldsymbol{F}_i^{'}$ is the i^{th} impact force vector.

To characterize the sources, an nt-by-n matrix of the n modal forces may be assembled over nt spectral lines (with n $\leqslant$ nt) and decomposed via singular value decomposition (SVD) as

$$\boldsymbol{f}_i^{'} = \boldsymbol{U}_i \boldsymbol{\Sigma}_i \boldsymbol{V}_i^{T} \ , (i = 1, \cdots, nl) \tag{3.23}$$

where $\boldsymbol{U}_i = \left[\boldsymbol{U}_{i,1}, \boldsymbol{U}_{i,2}, \cdots, \boldsymbol{U}_{i,m}\right]$ is the right singular vectors, $\boldsymbol{V}_i^{T} = \left[\boldsymbol{U}_{i,1}, \boldsymbol{U}_{i,2}, \cdots, \boldsymbol{U}_{i,m}\right]$ is the left singular vectors, $\boldsymbol{\Sigma}_i = diag\left[\sigma_{i,1}, \sigma_{i,2}, \cdots, \sigma_{i,m}\right]$ is the singular values.

According to the Eq. (3.22), $\boldsymbol{f}_i^{'}$ contains only one feature vector $\boldsymbol{F}_i^{'}$. Eq. (3.23) could be approximated by the first singular value and associated basis vectors as follows:

$$\boldsymbol{f}_i^{'} \approx \boldsymbol{U}_{i,1} \sigma_{i,1} \boldsymbol{V}_{i,1}^{T} \tag{3.24}$$

Combining Eqs. (3.23) and (3.24), the singular vector $\boldsymbol{U}_{i,1}$ is associated with the modal coefficients, and it could be expressed as

$$\boldsymbol{U}_{i,1} = \boldsymbol{\Phi}^T \boldsymbol{a}_i + \boldsymbol{e} \ , (i = 1, \cdots, nl) \tag{3.25}$$

where $\boldsymbol{a}_i = \boldsymbol{L}_i a_i$ and a_i is a coefficient. $\boldsymbol{e}$ is the inevitable error.

Here $\{a_i, i = 1,2, \ldots nl\}$ are related to the locations of the impact forces and they can be determined by the sparse regularisation as,

$$\underset{\boldsymbol{a}_i}{\text{Minimize}} \qquad \|\boldsymbol{\Phi}^T \boldsymbol{a}_i - \boldsymbol{D}^*\|_2^2 + \lambda \|\boldsymbol{a}_i\|_1 \ , (i = 1, \cdots, nl) \tag{3.26}$$

Once the force locations are determined, the transfer matrix could be constructed for the force amplitudes corresponding to all modes.

3.3 Regularisation model for impact force identification

In this section, two popular regularisation techniques for the inverse problem are compared and then a new method based the regularisation technique is proposed for impact force identification. The Tikhonov regularisation, which is based on minimizing l_2-norm, is the most popular method for solving linear inverse problems. Its solution is generally non-sparse, and it

plays an important role in the field of the force identification in the past two decades. Exploiting the sparse prior of the unknown solution, the sparse regularisation based on minimizing l_1-norm, recently has been introduced into the field of the force identification.

3.3.1 l_2-norm Regularisation

Tikhonov regularisation seeks for a stable solution by introducing an l_2-norm penalty with controlling highly oscillating components. Hence, the impact force identification problem is defined as a trade-off between the residual and regularized norms.

$$\underset{\boldsymbol{F}}{\text{Minimize}} \qquad \|\boldsymbol{HF}-\boldsymbol{A}\|_2^2+\lambda\|\boldsymbol{F}\|_2^2 \tag{3.27}$$

where $\lambda > 0$ is named the regularisation parameter. The l_2-norm of the impact force $\|\boldsymbol{F}\|_2^2$ is called the regularisation term or the penalty term. The ill-posed problem in Eq. (3.14) is solved by introducing the regularisation term, and it renders the problem less sensitive to perturbations. Due to the convexity of Eq. (3.27), Tikhonov regularisation always has an analytic solution with any fixed λ

$$\boldsymbol{F}=(\boldsymbol{H}^T\boldsymbol{H}+\lambda\boldsymbol{I})^{-1}\boldsymbol{H}^T\boldsymbol{A} \tag{3.28}$$

From Eq. (3.28), one can note that the Tikhonov solution is a smooth function of λ, as it varies over the interval $(0, \infty)$.

3.3.2 l_1-norm Regularisation

The l_1-norm Regularisation technique is also called the Lasso regression. It is widely used in domains with massive datasets, such as genomics, where efficient and fast algorithms are essential. The lasso regression is not robust to highly correlated predictors. It chooses only one and shrinks the others to zero. The lasso penalty expects many coefficients to be close to zero, and only a small subset to be larger (and nonzero). The lasso estimator uses the l_1 penalized least squares criterion to obtain a sparse solution as

$$\underset{\boldsymbol{F}}{\text{Minimize}} \qquad \|\boldsymbol{HF}-\boldsymbol{A}\|_2^2+\lambda\|\boldsymbol{F}\|_1 \tag{3.29}$$

3.3.3 Truncated transfer matrix-based method for impact force identification

Previous studies assumed that the impact force as a triangular pulse with only one nonzero value. Under this assumption, the identification method based on the l_1-norm regularisation technique performs very well. In practice, the impact force has a time duration and for the discrete form, there are several nonzero values within the specific time interval. As shown in Figure 3.1, a single impact force can be separated into zero entries and non-zero entries. The transfer matrix is a lower triangular Toeplitz matrix and strong correlations exist among the adjacent columns in this matrix. The l_1-norm penalty treats all variables differently and encourage sparsity in individual coefficients. The strong correlation of variables will result in elimination of coefficients.

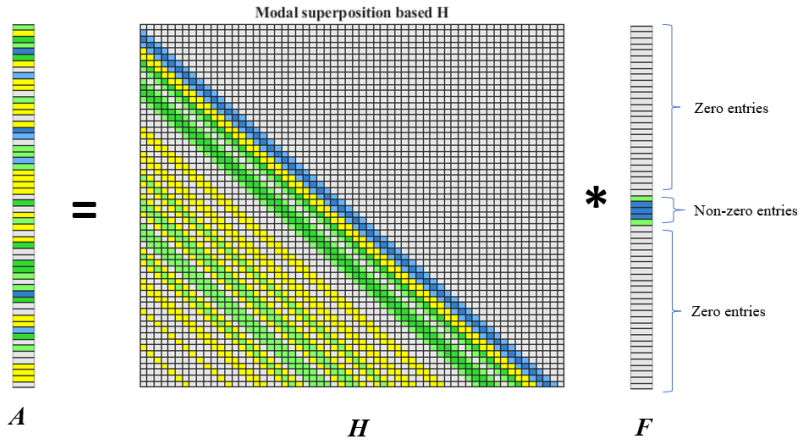

Figure 3.1 Discrete form of the impact force identification

The l_1-norm regularisation is not robust to variables with high correlations. It is not good for the identification of the impact force with a time duration. The l_2-norm penalty treats all variables equally and does not encourage sparsity. The identified result will be smoothed, especially with the effect of the measurement noise in the response. The group lasso regularisation technique combining the l_1-norm penalty and l_2-norm penalty is adopted here as

$$\underset{\boldsymbol{F}}{\text{Minimize}} \qquad \|\boldsymbol{HF}-\boldsymbol{A}\|_2^2+\lambda\sum_i^{GN}\left\|\boldsymbol{F_{gi}}\right\|_2^2 \tag{3.30}$$

The group lasso regularisation technique is extreme time-consuming, especially for this inverse problem with a large transfer matrix (Pan et al, 2020). Considering the sparse feature of the impact force, the nonzero force values in the specific time interval can be located according to the structural dynamic response as shown in Figure 3.2. From the dynamic response, the excitation time can be estimated approximately. The time interval enclosed by the red rectangle could be used to decrease the columns of the transfer matrix into several variables and it is the truncated transfer matrix as shown in Figure 3.2(b). The truncated transfer matrix based the group lasso regularisation (TML2) method is proposed as,

$$\underset{\boldsymbol{F}}{\text{Minimize}} \qquad \left\|\boldsymbol{H}_{gi}\boldsymbol{F}-\boldsymbol{A}\right\|_2^2+\lambda\left\|\boldsymbol{F}_{gi}\right\|_2^2 \tag{3.31}$$

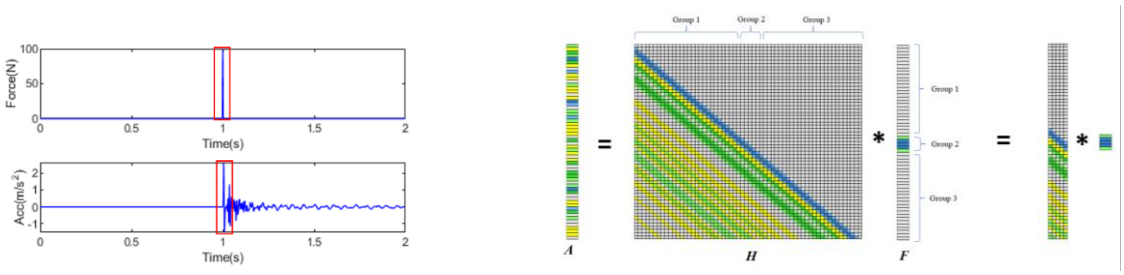

(a) (b)

Figure 3.2 (a) Time history of impact force and relevant dynamic response; (b) Truncated transfer matrix

3.4 Numerical study

3.4.1 Identification of impact forces on a simple supported beam

To evaluate the performance of the proposed method, a simply supported beam model subjected an impact force is adopted, as shown in Figure 3.3. The beam has the length of 6 m, the cross section of 0.1 m×0.03 m and the mass density of 7850 kg/m^3. The Young's modulus E of the beam material is 2.05×10^{11} N/m^2. Normally two coefficients of the Rayleigh damping are determined by measured natural frequencies and damping ratios. The structural damping is considered as the Rayleigh damping with α=0.5, β=1 in this study. The beam is divided into

300 equal Euler-Bernoulli finite elements. The first six natural frequencies of the beam are 1.95, 7.81, 17.50, 31.25, 48.83, and 70.32 Hz. The dynamic response of the beam under an impact force is calculated using the Newmark method with a time interval of 0.001 s and the time duration of 8 s. The impact force is a triangular pulse with five nonzero values.

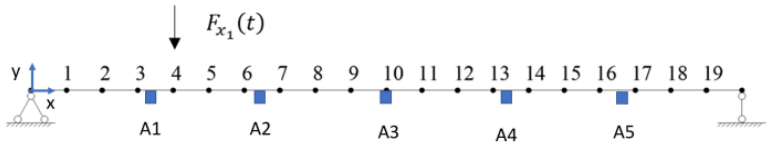

Figure 3.3 Numerical model of simply supported beam

Nineteen possible force locations are considered in the force localization. These locations are uniformly distributed along the beam. The interval between each position is 0.3 meters.

Table 3.1 Predefined possible force locations

Force	p1	p2	p3	p4	p5	p6	p7	p8	p9	p10	p11	p12	p13
x(m)	0.3	0.6	0.9	1.2	1.5	1.8	2.1	2.4	2.7	3	3.3	3.6	3.9
Force	p14	p15	p16	p17	p18	p19							
x(m)	4.2	4.5	4.8	5.1	5.4	5.7							

In the following study, the number of sensors for acceleration measurements are 5, 7 and 9 respectively and the sensor locations are evenly distributed along the beam. Those acceleration response measurements are used for the impact force identification. For example, the case with five sensors, the sensor locations $A_1 - A_5$ are labelled in Figure 3.3.

For evaluating the accuracy of the identified impact force, a relative percentage error (RE) is defined as

$$RE = \frac{\|f_{identified} - f_{true}\|_1}{\|f_{true}\|_1} \times 100\% \tag{3.32}$$

The force peak relative percentage error (PRE) is also defined for evaluating the accuracy of the identified peak for impact forces as

$$PRE = \frac{|\max(f_{identified}) - \max(f_{true})|}{\max(f_{true})} \times 100\% \tag{3.33}$$

where $f_{identified}$ and f_{true} are the identified and true forces respectively.

White noise is added to simulate the measurement as

$$\boldsymbol{A_n} = \boldsymbol{A} + lev \times \frac{1}{n} \|\boldsymbol{A}\|_1 \times \boldsymbol{rand} \tag{3.34}$$

where $\boldsymbol{A_n}$ and $\boldsymbol{A}$ are the structural responses corresponding to noise and noiseless, respectively. n is the total number of elements in the vector $\boldsymbol{A}$. lev is the noise level. $\|\boldsymbol{A}\|_1$ is the l_1-norm of the vector $\boldsymbol{A}$. $\boldsymbol{rand}$ is a random vector with the normal distribution.

3.4.2 Single impact force identification

In this section, the single impact force identification from dynamic measurements of the beam is conducted. The impact force is applied at the location P4. From acceleration response measurements from five sensors evenly distributed along the beam, the mass normalized modal coefficient, the modal response under the impact force excitation could be extracted as shown in Figure 3.4. Then each modal force could be reconstructed from the modal response using regularisation method respectively. The results are shown in Figure 3.4.

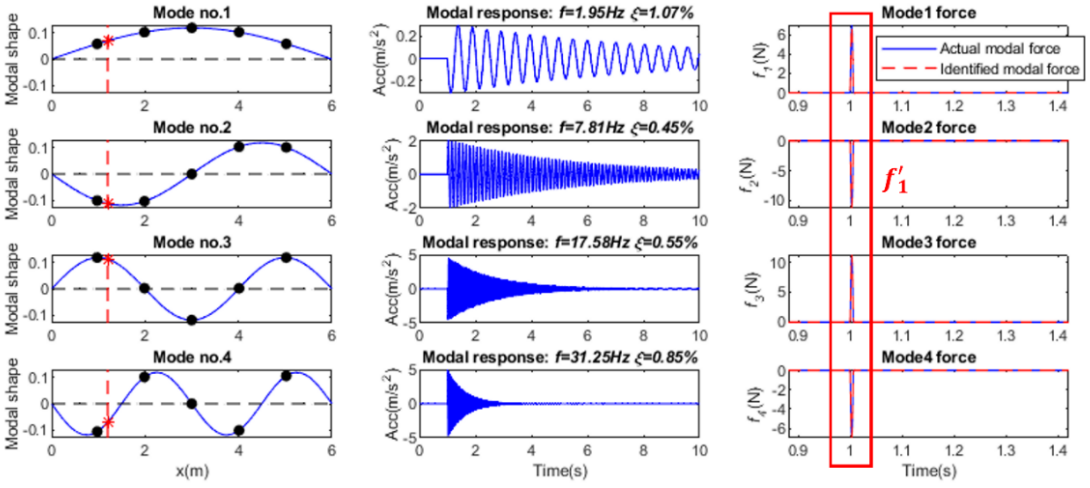

Figure 3.4 Modal parameters for the single force identification

The modal force contains the force location information. Using Eqs. (3.23) and (3.24), the singular vector containing the force location information can be extracted from the modal force. As shown in Eq. (3.25), this singular vector has a strong correlation with the modal shape coefficient. Due to the sparsity of the location, the sparse regularisation method could be used for the location identification by Eq. (3.26). Once the force location is determined, Eq. (3.14) is used for the impact force identification. The following sections are to study the performance of different regularisation methods and the influence of the mode number, the sensor number and the noise level.

3.4.2.1 Comparison of results with different regularisation methods

In this section, a conparison study on the l_1-norm, l_2-norm and TML2 regularisation methods on the impact force identification is conducted. Nine sensors are used in this study and they are evenly distributed along the beam. 10 modes are used for the transfer matrix construction. 10% noise level is considered in this section. Table 3.2 shows the identified errors using the Tikhonov regularisation, the standard sparse regularisation, and the truncated transfer matrix based regularisation. The identified results with 10 modes from response measurement of nine sensors with 10% noise level are shown in Figure 3.5.

Table 3.2 Identified errors using different regularisation methods

Tikhonov regularisation			Standard sparse regularisation			Truncated transfer matrix based regularisation		
RE (%)	PRE (%)	Time (s)	RE (%)	PRE (%)	Time (s)	RE (%)	PRE (%)	Time (s)
30.45	12.39	24.73	142.54	258.77	335.51	6.41	1.86	1.04

The results show that the TML2 regularisation method has the best performance for impact force value identification. The identified result by the l_2-norm regularisation method is a little smaller than the true value and this is the smoothing effect due to the measurement noise. There

is a large identified error by the l_1-norm regularisation method. This is due to there is a high correlation existing inside the transfer matrix and the l_1-norm regularisation method is not suitable for this case with five nonzero values in the impact force. In the following sections, the effect of different parameters on the identified results using the TML2 regularisation method is studied.

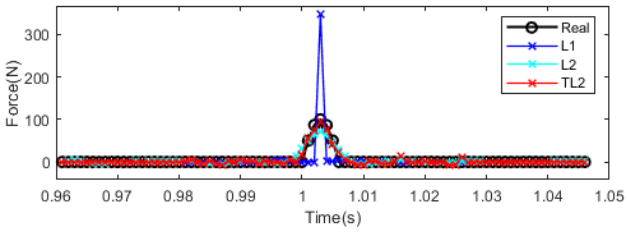

Figure 3.5 Identified impact force with measurements of nine sensors considering 10% noise level

3.4.2.2 Effect of measurement noise

In this section, the effect of the measurement noise is studied and 1%, 5% and 10% noise levels are discussed. The noise is included in the original measurement response as listed in Eq. (3.34). Nine sensors are used. 10 modes are used to construct the transfer matrix.

To reduce the noise effect, the low pass filter is used for each modal response. The identification results from measurements with 1%, 5% and 10% noise levels are shown in Figure 3.6. As shown in Figure 3.6(a), there are variations in the identified force locations. When the noise level is 10%, there is a mis-identified force location around 5.5 m. To accurately locate the force position, the signal processing techniques is needed to reduce the measurement noise in the responses. As shown in Figure 3. 6(b), the identified force values from the measurements with different measurements are very close. The results show that the proposed method is robust to the measurement noise for the force value identification.

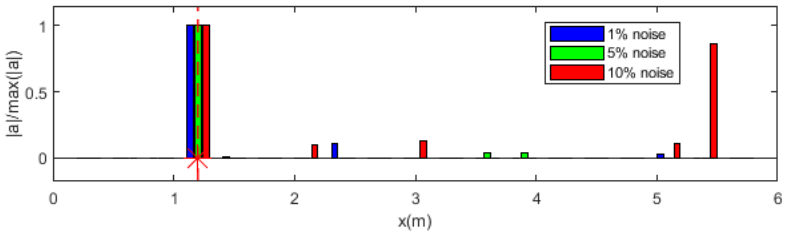

(a) Location identification

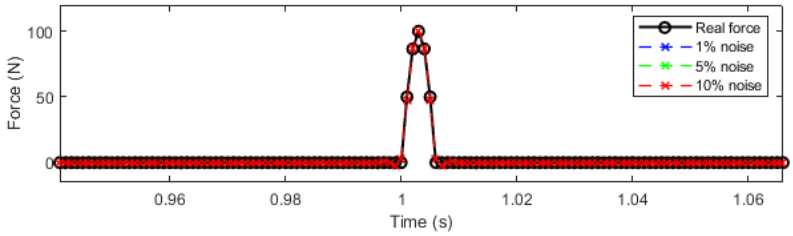

(b) Force value identification

Figure 3.6 Effect of measurement noise on impact force identification

3.4.2.3 Effect of number of modes

In this section, the effect of the number of modes on impact force identification is studied. 4 modes, 6 modes. 8 modes and 10 modes are used, respectively. 5% noise level and nine sensors are considered in this study. The identified results are shown in Figure 3.7.

As shown in Figure 3.7(a), the location of the impact force can be identified successfully using different number of modes. Since the noise level influences the modal response extraction, especially the high frequency modes, there are large errors in the force location identification with the high number of modes. As shown Figure 3.7(b), the number of modes has a significant influence on the force value identification. The identified result is much close to the true value with the increase of the number of modes. Since the transfer matrix is constructed based on the modal superposition method, the transfer matrix with low modes does not contain high frequency components. The identified force value with less modes would be much smaller than the true value and the result with four modes is the worst case.

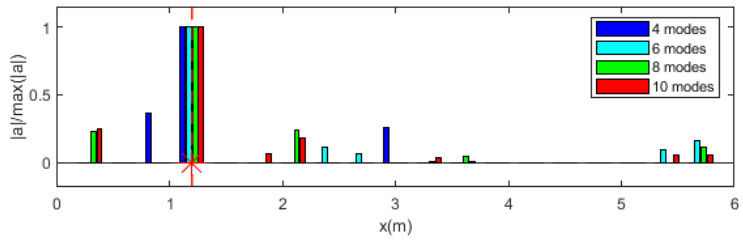

(a) Location identification

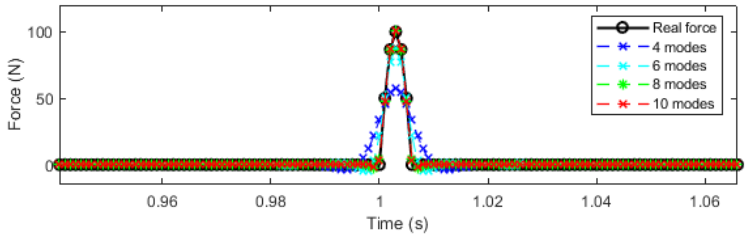

(b) Force value identification

Figure 3.7 Force identification results with different number of modes

3.4.2.4 Effect of number of sensors

In this section, the impact force identification with different number of sensors is conducted. Three cases, e.g., 5 sensors, 7 sensors and 9 sensors are studied. 5% noise level is considered, and 10 modes are used for the transfer matrix construction in this section. The identified results are shown in Figure 3.8.

From Figure 3.8(a), the location of the impact force is identified correctly when the number of sensors is 7 or 9. When the number of sensors is 5, the impact force location cannot be identified correctly. The results show that 7 sensors are needed to identify the force location. With more sensors, more accurate modal response could be decomposed from responses and more accurate load location coefficient could be extracted from the identified modal force. From Figure 3.8(b), the identified results by 5, 7 and 9 sensors are approximate the same and it shows that the number of sensors has no big influence on the force value reconstruction.

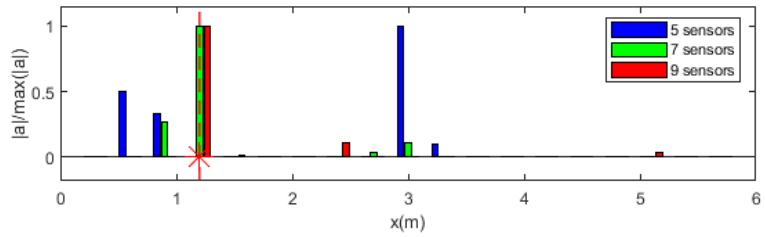

(a) Location identification results

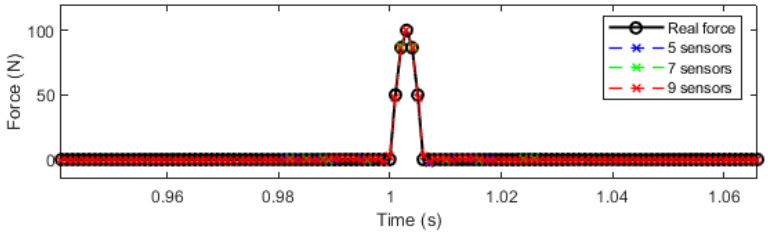

(b) Force value identification results

Figure 3.8 The force identification results with different number of sensors

Table 3.3 Identification accuracy index RE and PRE results

	Noise level			Number of modes				Number of sensors		
	1%	5%	10%	4	6	8	10	5	7	9
RE (%)	1.02	1.19	1.82	136.79	20.45	6.88	1.19	1.25	1.22	1.19
PRE (%)	1.02	1.19	1.82	39.98	12.86	2.34	1.18	1.18	1.17	1.17

3.4.3 Multiple impact force identification

To verify the performance of the multiple impact force identification, two impact forces are applied at Locations P4 and P8 respectively. As the same as the above, the sensors are evenly distributed along the beam. Figs. 3.9(a) and 3.9(b) show the mass normalized modal coefficient and the modal response under these impact force excitations extracted from the acceleration measurements. Fig 3.9(c) shows the modal forces reconstructed from the modal response using the regularisation method. Conclusions similar to those obtained for the identification of the single impact.

In this study, 10 modes are used for the transfer matrix. the number of sensors is 9, and 5% noise level is considered in the response measurements. Figure 3.10 shows the identification results. From Figure 3.10(a), the identified locations of two impact forces are the same as the true locations. In Figure 3.10(b), the identified two impact forces agree well with the true values. The results show that two impact forces can be identified accurately by the proposed method.

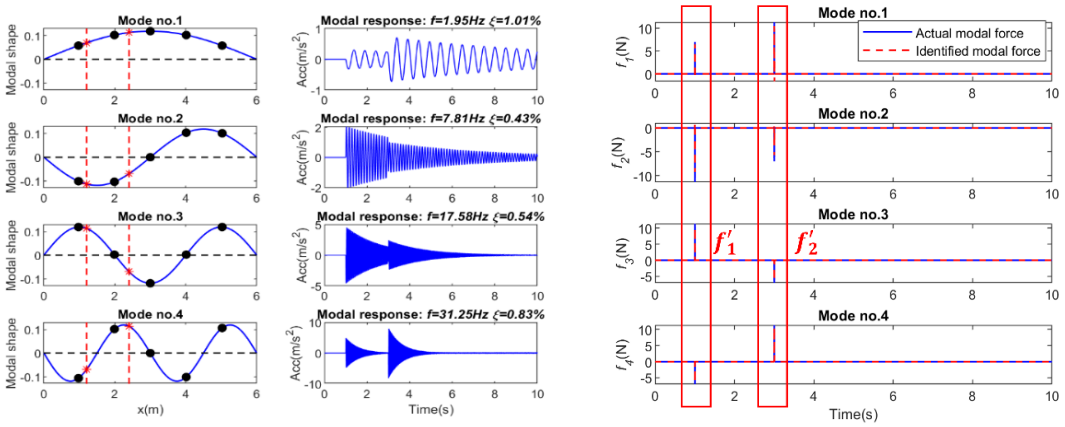

Figure 3.9 Modal parameters for two impact force identification

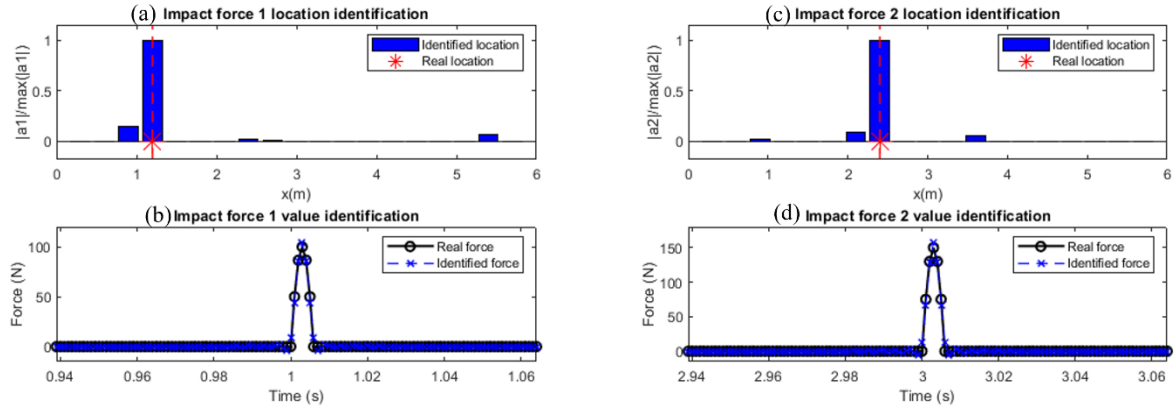

Figure 3.10 Identification of two impact forces (a) Location of Impact force 1; (b) The value of Impact force 1; (c) Location of Impact force 2; (d) The value of Impact force 2

3.5 Experimental validation

3.5.1 Experimental setup

To further verify the proposed method, a three-span steel-concrete composite beam bridge model (10000mm long, 1000mm wide and 300mm thick) was built in the laboratory, as shown in Figure 3.11. Three bridge spans are independent and the left and right spans are 2000 mm long. The middle span with 6000 mm long was the main span for testing. The main bridge is a concrete slab on two steel I-beams connected by shear connectors. The concrete slab has the thickness of 100 mm and the width of 1000 mm. Concrete grade 40 was used to construct slabs and shear connectors were marked as SC32. There are 45 accelerometers installed at the bottom of the bridge deck and the accelerometers arrangement is shown in Figure 3.12. From the results in Section 3.4.2.4, the accurate result can be obtained when the number of sensors is 5 or above, nine sensors in the middle of the beam are used for the load identification in this study.

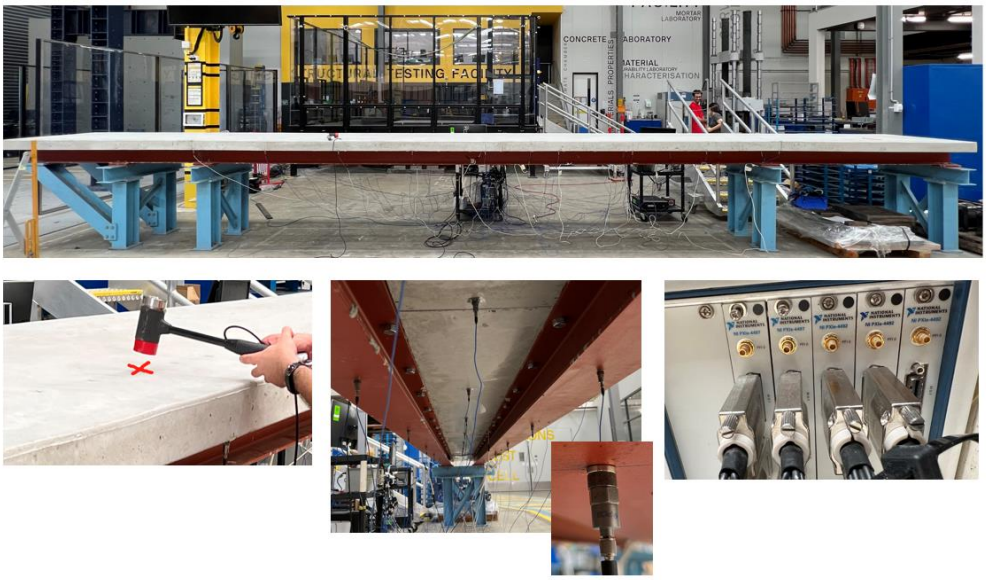

Figure 3.11 Experimental setup

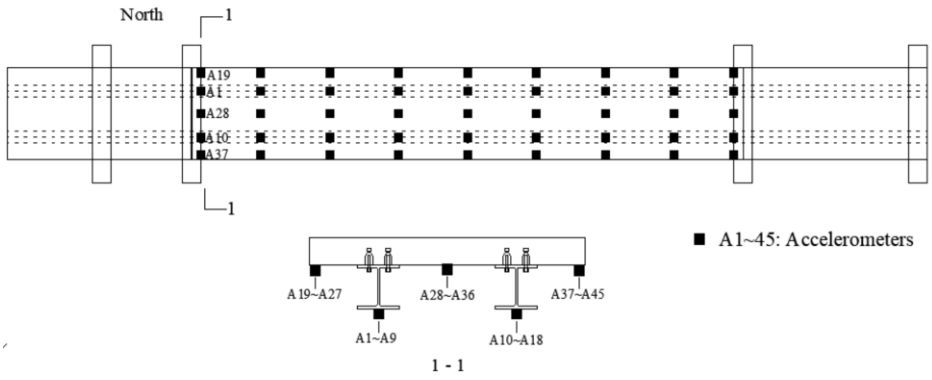

Figure 3.12 Arrangement of the accelerometers

3.5.2 Finite element model validation

The finite element (FE) model of the bridge was established using ANSYS. The convergence study has been conducted and all components including concrete slab, shear connectors, steel beam were properly modelled, as shown in Figure 3.13. The concrete slab and the steel girders were modelled by the shell element with four nodes (Shell 63). The steel girder and concrete slab are connected via bolts as shear connectors, which are used to transmit the longitudinal shear force between the steel girders and concrete slab. A non-linear spring element (Combin39) was employed to model the shear connector. The positions of the spring elements coincide with the positions of the shear connectors in the composite beam. The elastic Young's modulus of 205 GPa and Poisson's ratio of 0.3 are defined for the steel girder. The elastic Young's modulus of 30 GPa and Poisson's ratio of 0.3 are defined for the concrete slab. The bottom of the steel girder both ends are restricted to move in the X, Y, Z directions for simulating the real boundary conditions, as shown in Figure 8. The effect of frictional contact between steel girders and concrete slab is ignored in this model.

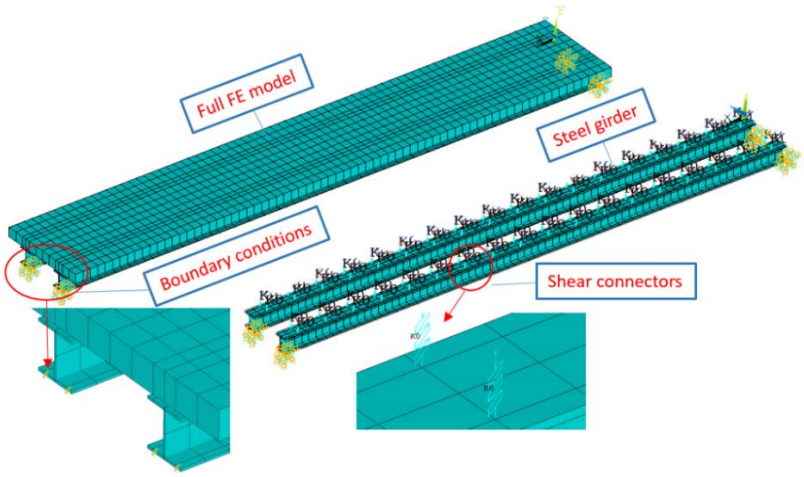

Figure 3.13 Finite element model

The mass-normalized mode shape coefficients can be calculated from FE model for the force identification. The errors of the FE model could affect the force identification results. The FE model was updated to ensure the best correlation between experimental and numerical frequency and mode shapes.

Table 3.4 Comparison of modal frequencies from the experiment testing and the updated FE model

Mode No.	Description	Modal Frequency (Hz)		Error	MAC
		Experiment	FE model		
1	1st bending	13.3	13.44	1.05%	99.76%
2	1st torsion	35.3	34.92	-1.08%	95.78%
3	2nd bending	48.6	48.37	-0.47%	99.95%
5	2nd torsion	82.7	80.72	-2.39%	94.44%
6	3rd bending	101.3	99.63	-1.65%	98.94%
8	3rd torsion	130.4	127.11	-2.52%	91.02%

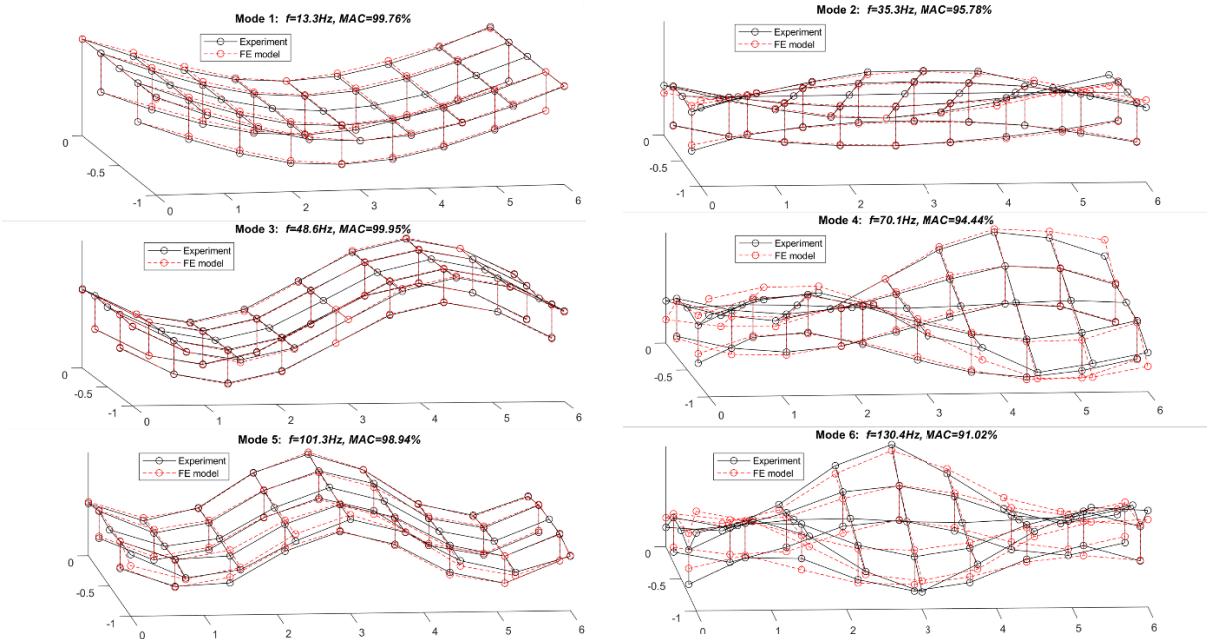

Figure 3.14 First 6 modal shape comparison between experimental model and FE model

Table 3.4 shows the modal frequencies and MAC values of the first modes from the experiment testing and the updated FE model. Figure 3.14 shows the modal shapes of the first modes. From Table 3.4, the natural frequencies from the experimental testing are very close to that from the FE model and the MAC values are all over 0.9000. From Figure 3.14, the modal shapes from the FE model are also very close to that from the experimental testing. The results show that the updated model could represent the experimental model. The updated FE model will be used to construct the modal shape coefficients in this study.

3.5.3 Impact force identification

In the experimental test, 28 possible excitation locations are labeled from S1 to S14 and N1 to N14 shown in Figure 3.15. The acceleration responses from A1 to A18 are used for the force identification. Single force identification and multiple force identification are conducted in this section.

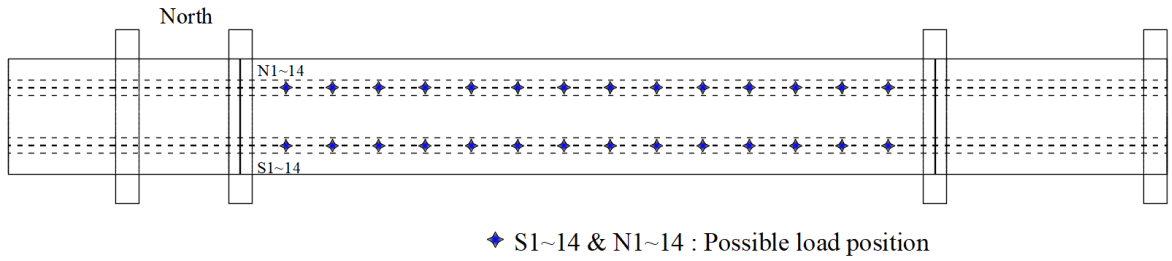

Figure 3.15 Predefined possible load position in the experiment model

3.5.3.1 Single force identification validation

For single force identification, the hammer excitation is applied at the location S4 as shown in Figure 3.15. The impact force and the acceleration responses at A1~A18 are recorded. The signal sampling frequency is 1000Hz. Figure 3.16 shows the impact force (located at S4) and the response time history at A2.

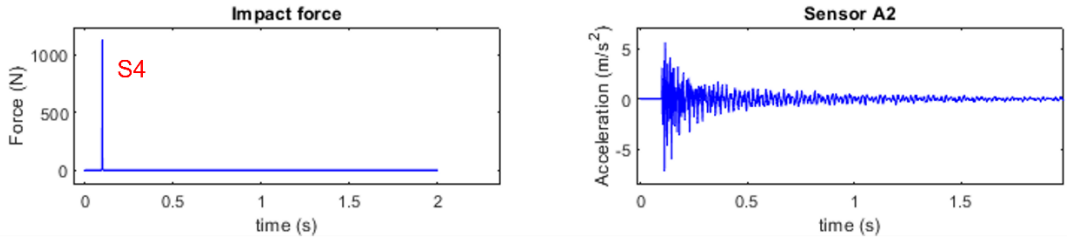

Figure 3.16. Time history of the impact force at S4 and the acceleration response at A2

The mass-normalized modal shape coefficient are obtained from the updated FE model. Acceleration responses at A1 to A18 are used for the force identification. From these acceleration responses, the modal responses can be extracted. To reduce the effect of the measurement noise, the bandpass filter is used to get the modal responses. Figure 3.17 shows the identified results of the impact force location using 4 modes, 6modes, 8 modes and 10 modes respectively. From the results, the force location can be identified correctly when the number of modes is 6, 8 or 10. The force location cannot be identified correctly using 4 modes. This is due to the force location information is embedded in the correlation coefficient of the modal force and the accuracy of the modal force affects the identification of the force location.

After obtaining the force location, the transfer matrix for the force value identification could be constructed.

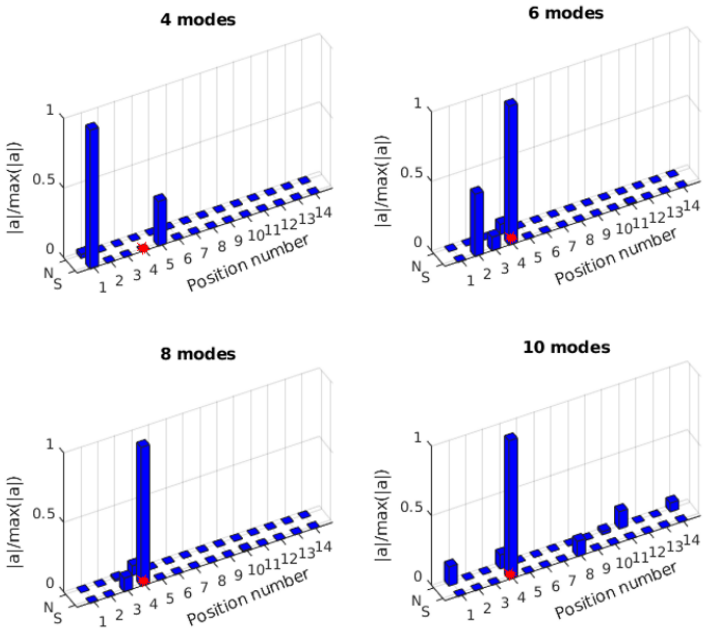

Figure 3.17 Impact force at S4 location identification results in 4 modes, 6 modes, 8 modes and 10 modes

From the numerical study in Section 3.4.2.3, the number of modes for constructing the transfer matrix has a large influence on the impact force identification. The frequency range of the measured acceleration response is up to 500 Hz as the sampling frequency is 1000 Hz. Only the limited modes are used to construct the transfer matrix. To reduce this effect, a lowpass filter is used and the cut-off frequency is chosen to cover the modes to construct the transfer matrix. As comparison, 4 and 10 modes are used to construct the transfer matrix in this study. Section 3.4.2.4 has discussed the effect of the number of sensors using numerical results. Here it is further verified using the experimental study. The sensors are installed on the beam evenly to capture the modal spatial information. Figure 3.18 shows the impact force identification using different number of sensors and modes. Figures 3.18(a) and 3.18(b) show the results by one sensor at A2 using 4 and 10 modes respectively. Figures 3.18(c) and 3.18(d) show the

identified results by three sensors at A2, A4 and A6 using 4 and 10 modes respectively. The results show that the force amplitude can be identified accurately for all cases. The result using 10 modes is better than that by 4 modes, and the results by 0ne and three sensors are approximate the same.

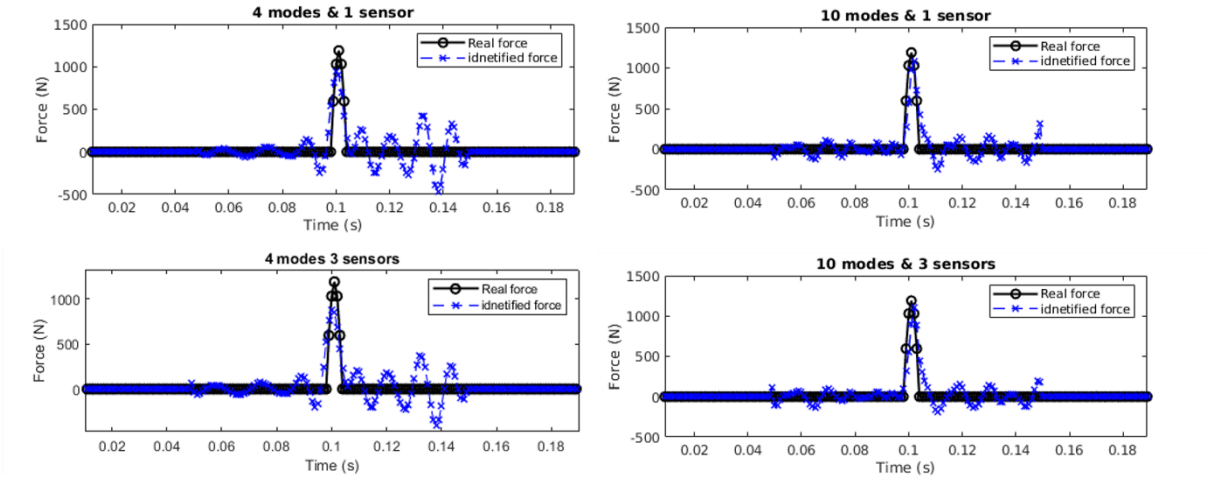

Figure 3.18 Impact force identification with different number of sensors and modes

3.5.3.2 Multiple force identification validation

For multiple force identification, the locations of these two impact forces are at S4 and S6 separately. The sampling frequency is 1000Hz. Figure 3.19 shows the impact forces (located at S4 and S6) and the time history response at A2.

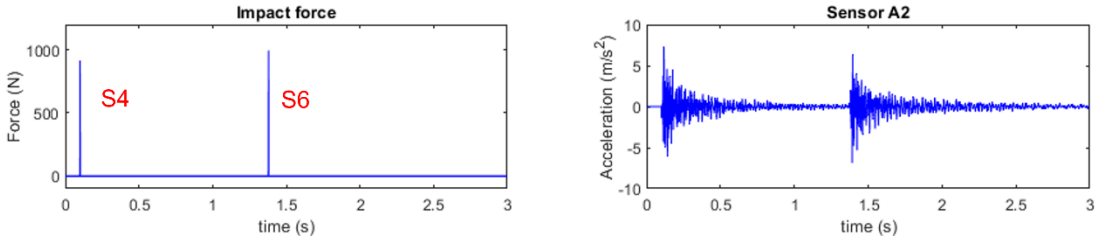

Figure 3.19 Impact forces at S4, S6 and the acceleration response at A2

Similar process with single force identification could be conducted for multiple force identification. The mass-normalized modal shape coefficients are extract using the updated FE model, and the modal responses are obtained from measured acceleration responses of 18

sensors. As comparison, 4 modes, 6 modes, 8 modes and 10 modes are used for these two force locations identification. The results are shown in Figures 3.20 and 3.21.

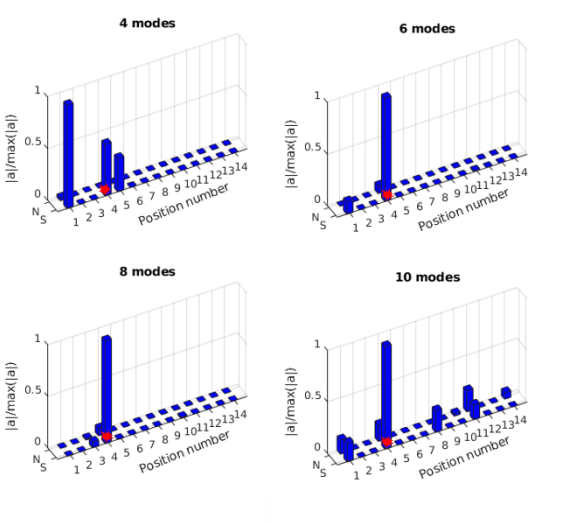

Figure 3.20 Identification of the impact force at S4 with different number of modes

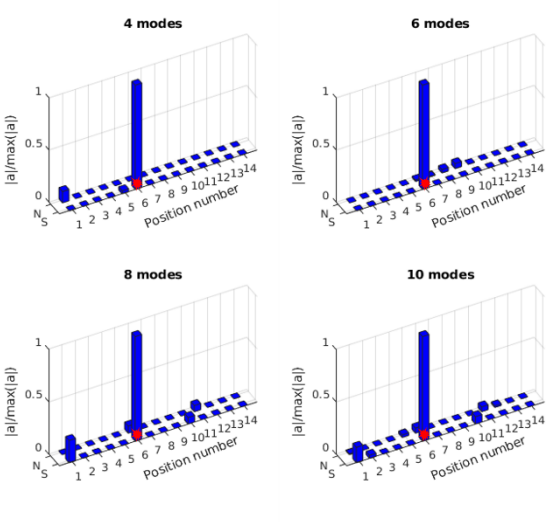

Figure 3.21 Identification of the impact force at S6 with different number of modes

From Figure 3.20, the location of the impact force at S4 is identified successfully using 6, 8 and 10 modes, there is an error using 4 modes. From Figure 3.21, the impact force at S6 can be correctly localised even using 4 modes. After obtaining the force location, the transfer matrix for the force value identification could be constructed.

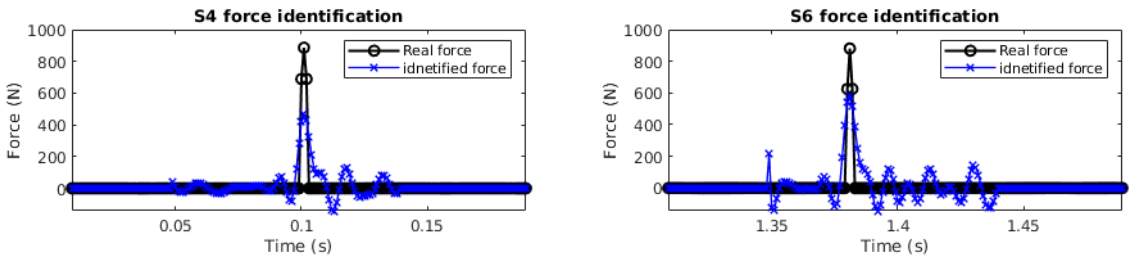

Figure 3.22 Two impact force identification with 10 modes & 3 sensors

From Section 4, the number of sensors has no big effect on the force value identification. For the multiple force value identification, 10 modes are used for constructing the transfer matrix and three sensors (A2, A4, A6) are used. Figure 3.22 shows the identified impact forces. The

results show that two impact forces are identified successfully, and the amplitudes of identified forces are a little smaller than the measured values.

3.6 Summary

In this paper, a new two-step method has been developed for multiple impact force identification. The sparse regularisation method is for the impact force localisation and the truncated transfer matrix-based regularisation method is to identify the impact force value. Based on the prior information of the impact force, the transfer matrix could be truncated into specific features to eliminate the effect of unloading intervals. The modal parameters and the sparse feature could be used to localise the force location. The validation of the proposed method is conducted numerically on a simply supported beam model and experimentally on a composite bridge model. Comparing with the classical Tikhonov (l_2-norm) regularisation method and the standard sparse (l_1-norm) regularisation method, the proposed method has the better accuracy and time efficiency on the impact force value identification. Its robustness to the measurement noise. The effect of the number of modes and sensors is also discussed. In the experimental study, single force and multiple forces localization and identification are conducted to validate the proposed method. The results show that the proposed method has a good applicability and accuracy for potential practical applications.

Chapter 4 Low-rank transfer submatrix-based group sparse regularisation for impact force localization and reconstruction

4.1 Overview

Recently the group sparsity has been exploited as an alternative sparse regularisation technique in force localization-and-reconstruction problems. Feng et al. (2021) utilized the external force group sparse feature and proposed a time domain group sparsity regularisation method, named Group Relevance Vector Machine, to localise and reconstruct external forces on structures based on structure responses only. Liu et al. (2022) also used the force vector group sparse feature and proposed an impact force identification method based on the nonconvex overlapping group sparsity (NOGS), allowing to localise the impact and recover its time history simultaneously from limited measurements. As above, the entire transfer matrix is used for impact force identification. However, the matrix part for the unloading time interval force information is redundant in the calculation. So the number of sensors should be larger than the number of forces. For the impact force identification, the prior information of the impact force such as the time duration of the force that is easily obtained from the response, could be used. To eliminate the effect of the unloading interval, the transfer submatrix associated with the impact excitation time interval could be extracted for the loading interval force identification.

In this chapter, a new transfer submatrix-based group sparse regularisation method for impact force localization and reconstruction is proposed. It is organized as follows. Section 4.2 presents the theory of the impact force identification. In Section 4.3, the standard l_1-norm regularisation method, the classical l_2-norm regularisation method, and the sparse group regularisation based on $l_{2,1}$ norm penalty method are depicted. Numerical and experimental

validation are presented in Sections 4.4 and 4.5. Finally, several conclusions are drawn in Section 4.6.

4.2 Theory

4.2.1 Force identification

Figure 4.1 shows a simple supported Euler-Bernoulli beam subjected to impact forces. The excitation locations are unknown and several potential force locations are pre-defined. The beam is uniform with the linear, viscous proportional damping and the deflection is small. The effects of shear deformation and rotary inertia are neglected. The dynamic governing equation of the beam is given by:

$$\boldsymbol{M}\ddot{\boldsymbol{x}}(t) + \boldsymbol{C}\dot{\boldsymbol{x}}(t) + \boldsymbol{K}\boldsymbol{x}(t) = \boldsymbol{L}\boldsymbol{F}(t) \tag{4.1}$$

where $\boldsymbol{M}$, $\boldsymbol{C}$ and $\boldsymbol{K}$ are the mass, damping, and stiffness matrices of the beam respectively. $\ddot{\boldsymbol{x}}(t)$, $\dot{\boldsymbol{x}}(t)$ and $\boldsymbol{x}(t)$ are acceleration, velocity and displacement vectors of the beam. $\boldsymbol{F}(t)$ is the input force vector and $\boldsymbol{L}$ is the mapping matrix for the input.

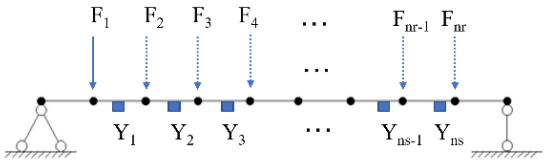

Figure 4.1 Simply supported beam subjected to impact forces

Eq. (4.1) can be expressed in the state space as

$$\dot{\boldsymbol{z}}(t) = \boldsymbol{A}\boldsymbol{z}(t) + \boldsymbol{B}\boldsymbol{F}(t) \tag{4.2}$$

where $\boldsymbol{z}(t) = \begin{Bmatrix}\boldsymbol{x}(t)\\ \dot{\boldsymbol{x}}(t)\end{Bmatrix}$, $\boldsymbol{A} = \begin{bmatrix}\boldsymbol{0} & \boldsymbol{I}\\ -\boldsymbol{M}^{-1}\boldsymbol{K} & -\boldsymbol{M}^{-1}\boldsymbol{C}\end{bmatrix}$, and $\boldsymbol{B} = \begin{bmatrix}\boldsymbol{0}\\ \boldsymbol{M}^{-1}\boldsymbol{L}\end{bmatrix}$. $\boldsymbol{A}$ is the continuous system matrix. $\boldsymbol{B}$ is the input matrix and $\boldsymbol{I}$ is an identity matrix. When acceleration response measurements are available at certain locations of the structure, the output vector can be

formulated as $\boldsymbol{y}(t) = \mathbf{R}\ddot{\boldsymbol{x}}(t)$ with **R** being the output influence matrix, which depends on the sensor location information. Consequently, the measurement can be expressed as

$$\boldsymbol{y}(t) = \boldsymbol{C}\boldsymbol{z}(t) + \boldsymbol{D}\boldsymbol{F}(t) \tag{4.3}$$

where $\boldsymbol{C} = [-\boldsymbol{R}\boldsymbol{M}^{-1}\boldsymbol{K}, -\boldsymbol{R}\boldsymbol{M}^{-1}\boldsymbol{C}]$ and $\boldsymbol{D}(t) = \boldsymbol{R}\boldsymbol{M}^{-1}\boldsymbol{L}$ are respectively the continuous output matrix and feedthrough matrix.

Combining Eqs. (4.4) and (4.5), we can obtain the continuous analytical solution as follows

$$\boldsymbol{y}(t) = \boldsymbol{C}\boldsymbol{\Phi}(t)\boldsymbol{z}(0) + \boldsymbol{C}\int_0^t \boldsymbol{\Phi}(t,\tau)\boldsymbol{B}\boldsymbol{F}(\tau)d\tau + \boldsymbol{D}\boldsymbol{F}(t) \tag{4.4}$$

where $\boldsymbol{\Phi}(t) = \exp(\boldsymbol{A}t)$

Considering the zero initial conditions, the dynamic force $F_i(t)$ is supposed to be an impulse signal,

$$\boldsymbol{F}(t) = \boldsymbol{e_i}\delta(t-\tau), \text{ with } \boldsymbol{e_i} = [0,\cdots,0,1,0,\cdots,0]^T \tag{4.5}$$

The measured response at the *j*th point is

$$h_{ji}(t,\tau) = y_j(t) = \boldsymbol{C}_j\int_0^t \boldsymbol{\Phi}(t,\tau)\boldsymbol{B}\boldsymbol{e_i}\delta(\tau-\tau_1)d\tau + \boldsymbol{D}\boldsymbol{e_i}\delta(t-\tau_1) \tag{4.6}$$

For the multiple dynamic forces and multiple measured responses, it can be expressed as

$$\boldsymbol{y}(t) = \int_0^t \boldsymbol{h}(t,\tau)\boldsymbol{F}(\tau)d\tau \tag{4.7}$$

where $\boldsymbol{h}(t,\tau) = \begin{bmatrix} h_{11}(t,\tau) & h_{12}(t,\tau) & \cdots & h_{1,nr}(t,\tau) \\ h_{21}(t,\tau) & h_{22}(t,\tau) & \vdots\vdots & h_{2,nr}(t,\tau) \\ \cdots & \cdots & \cdots & \cdots \\ h_{ns,1}(t,\tau) & h_{ns,2}(t,\tau) & \cdots & h_{ns,nr}(t,\tau) \end{bmatrix}$, $\boldsymbol{F}(t) = [F_1(t), F_2(t), \cdots, F_{nr}(t)]^T$.

The convolution problem of Eq. (4.7) can be converted into the following discrete equation as

$$\mathbf{Y} = \mathbf{H}\mathbf{F} \tag{4.8}$$

where $\mathbf{Y} = \begin{Bmatrix} \boldsymbol{Y_1} \\ \boldsymbol{Y_2} \\ \vdots \\ \boldsymbol{Y_{ns}} \end{Bmatrix}$, $\boldsymbol{H} = \begin{bmatrix} \boldsymbol{H}_{11} & \boldsymbol{H}_{12} & \cdots & \boldsymbol{H}_{1,nr} \\ \boldsymbol{H}_{21} & \boldsymbol{H}_{22} & \cdots & \boldsymbol{H}_{2,nr} \\ \vdots & \vdots & \ddots & \vdots \\ \boldsymbol{H}_{ns,1} & \boldsymbol{H}_{ns,2} & \cdots & \boldsymbol{H}_{ns,nr} \end{bmatrix}$ and $\boldsymbol{F} = \begin{Bmatrix} \boldsymbol{F_1} \\ \boldsymbol{F_2} \\ \vdots \\ \boldsymbol{F_{nr}} \end{Bmatrix}$

$$\mathbf{H_{11}} = \begin{bmatrix} h_{11}(t_1) & 0 & \cdots & 0 & 0 \\ h_{11}(t_2) & h_{11}(t_1) & \cdots & 0 & 0 \\ \vdots & \vdots & \cdots & \vdots & \vdots \\ h_{11}(t_{n-1}) & h_{11}(t_{n-2}) & \cdots & h_{11}(t_1) & 0 \\ h_{11}(t_n) & h_{11}(t_{n-1}) & \cdots & h_{11}(t_2) & h_{11}(t_1) \end{bmatrix} \Delta t \tag{4.9}$$

4.2.2 Impact force identification using one single sensor

Generally, a standard transfer matrix is used for force identification. Providing that one impact force is applied at F_1 on a simple supported Euler-Bernoulli beam as shown in Figure 4.1, Eq. (4.8) could be express submatrices in Figure 4.2. For *nr* potential pre-defined force locations, the assembled force vector ***F*** can be naturally divided into *nr* subgroups, and each subgroup is associated with one potential force location. Among the potential locations, only a fraction of them is exerted by non-zero forces, which is referred as the true force location. The rest of them are referred as non-force locations. To solve this equation, the number of sensors should be more than the number of forces. Otherwise, this problem will be under-determined.

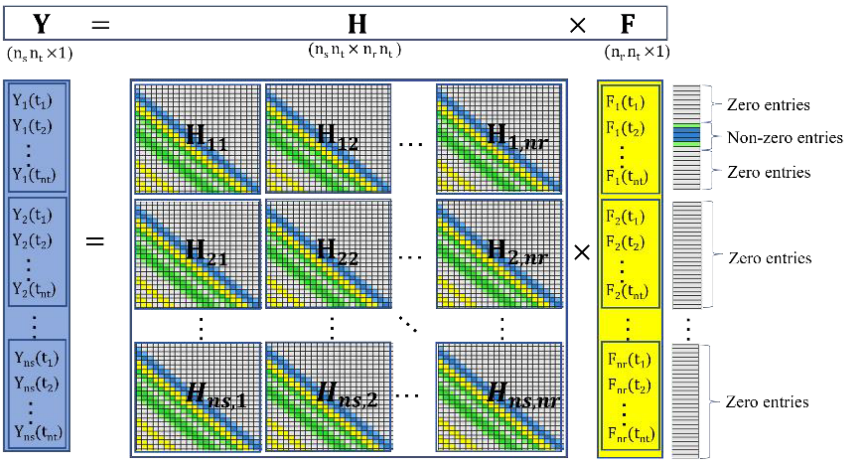

Figure 4.2 The discrete format of Eq. (4.8)

Based on the intrinsic feature of the impact force in Figure 4.2, only a submatrix of the standard transfer matrix is associated with the impact force time interval and this submatrix could be selected for the force identification. In this study, one single sensor response is used for the impact force identification and the discrete form is shown in Figure 4.3. The dimension of the

submatrix is much smaller than that of the standard transfer matrix and the computational efficiency could be increased significantly.

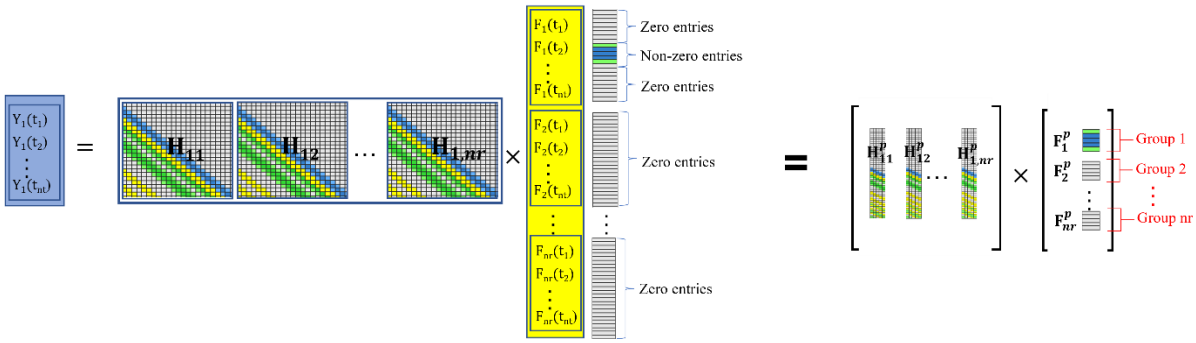

Figure 4.3 The discrete form using the submatrix with one single sensor

For the case with one single sensor, Eq. (4.8) can be expressed as

$$\mathbf{Y_1} = \mathbf{H}^p\mathbf{F}^p \tag{4.10}$$

Here, the force vector is grouped as

$$\mathbf{F}^p = \left[\mathbf{F}_1^{p\,T}\ \mathbf{F}_2^{p\,T} \cdots \mathbf{F}_{nr}^{p\ T}\right]^{\boldsymbol{T}} \tag{4.11}$$

where $\mathbf{F}_i^p$ is the force history vector at the location i.

Considering the measurement noise in the response, Eq. (4.10) can be written as

$$\mathbf{Y_1} = \mathbf{H}^p\mathbf{F}^p + \mathbf{w} \tag{4.12}$$

where the vector $\mathbf{w}$ represents the inevitable measurement noise.

4.3 Impact force identification using group sparse regularisation

In this section, the group sparse regularisation technique for the impact force identification is introduced. The force identification is an inverse problem and many regularisation techniques have been proposed for solving the linear inverse problems. The Tikhonov regularisation and *l*1-norm regularisation are two popular algorithms. These two methods have been introduced in Chapter 3. This section mainly presents the group sparse regularisation method.

For the impact force identification, the pulse interval can be regarded as a group and the sparse elements of unknown impact forces exhibit intrinsic structure in form of groups as shown in Figure 4.3. The standard sparse regularisation technique in Eq. (3.29) does not take advantage of the group structure of the impact force. To utilise the group structure, the group sparse regularisation technique for impact force identification is proposed and the $l_{2,1}$-norm penalty is used to replace the pure l_2-norm term in Eq. (3.27) or the l_1-norm penalty in Eq. (3.29). The regularisation technique based on the mixed $l_{2,1}$-norm penalty has been successfully used in the group Lasso, the logistic group Lasso and the generalized linear models, generally leading to a better recovery performance. Here the group sparse regularisation technique is integrated with the subspace transfer matrix for the impact force localization and reconstruction as,

$$\underset{\boldsymbol{F}}{\text{Minimize}} \qquad \|\mathbf{H}^p\mathbf{F}^p - \mathbf{Y_1}\|_2^2 + \lambda \sum_{i=1}^{nr} \left\|\mathbf{F}_i^p\right\|_2 \tag{4.13}$$

where $\mathbf{F}_i^p$ is the force history vector at the location i.

4.4 Numerical study

4.4.1 Simple supported beam

To verify the effectiveness and performance of the proposed method for impact force identification, the simulations are carried out on a simply supported beam model. The beam model is 6 m long with the cross section of 0.1m×0.03m and the mass density of 7850 kg/m^3. The Young's modulus E of the beam material is 2.05×10^{11}N/m^2, and the structural damping is considered as Rayleigh damping with α=0.5, β=1. The beam model is divided into 300 equal Euler-Bernoulli finite elements. The dynamic response of the beam is calculated with a time interval of 0.001s and the measurement duration of 4 s. The impact force is simulated as a triangular pulse with 5 nonzero values. The range of the impact force with nonzero force values is identified. Nine possible force locations are considered in the force localization, as listed in Table 4.1. These locations are uniformly distributed along the beam. The distance between two

adjacent locations is 0.6 m. Since the sensor locations do not have much effect on the identification result. In this study the effect of the sensor location is not further discussed.

Table 4.1 Predefined possible force locations

Force	p1	p2	p3	p4	p5	p6	p7	p8	p9
x(m)	0.6	1.2	1.8	2.4	3	3.6	4.2	4.8	5.4

To localise the impact force, the location index for the i^{th} group of the identified force vector is defined as

$$LOC_i = \frac{\|\tilde{\mathbf{F}}_i^p\|_2}{\|\tilde{\mathbf{F}}^p\|_2} \times 100\% \tag{4.14}$$

where $\tilde{\mathbf{F}}_i^p$ is the i^{th} group of the estimated force vector, $\tilde{\mathbf{F}}^p$ is the entire estimated force vector. From Eq. (4.14), the location index can be calculated by the ratio between the l_2 norm of the estimated ith group force vector and that of the entire force vector in percentage.

Here a relative error in percentage is used to evaluate the accuracy of identified impact forces. The relative error (RE) for the i^{th} force identification is defined as the difference between the actual force vector $\mathbf{F}_i^p$ and the estimated one $\tilde{\mathbf{F}}_i^p$,

$$RE_i = \frac{\|\mathbf{F}_i^p - \tilde{\mathbf{F}}_i^p\|_1}{\|\mathbf{F}_i^p\|_1} \times 100\% \tag{4.15}$$

To evaluate the accuracy of the peak value of the identified impact forces, the relative percentage error of the peak value (PRE) for the i^{th} force identification is defined as

$$PRE_i = \frac{\left\|\mathrm{F}_{pi}^p - \tilde{\mathrm{F}}_{pi}^p\right\|_1}{\left\|\mathrm{F}_{pi}^p\right\|_1} \times 100\% \tag{4.16}$$

where $\tilde{\mathrm{F}}_{pi}^p$ and F_{pi}^p are the ith identified and true impact forces respectively.

To study the effect of measurement noise, the white noise is added to simulate the measurement as

$$\mathbf{Y}_n = \mathbf{Y}_1 + lev \times \frac{1}{n}\sum_{i=1}^{n}|\mathbf{Y}_1| \times \boldsymbol{rand} \tag{4.17}$$

where $\mathbf{Y}_{\boldsymbol{n}}$ and $\mathbf{Y}_1$ are the structural responses corresponding to noise and noiseless, respectively. n is the total number of elements in the vector $\mathbf{Y}_1$. lev is the noise level. $\boldsymbol{rand}$ is a standard normal distribution vector.

4.4.2 Determination of the low-rank matrix for impact force identification

Based on the specific feature of the impact force and its relevant dynamic response, the duration of the impact force can be estimated as shown in Figure 4.4. From the acceleration response, the force duration is around the beginning of the response marked as two red dotted lines in the figure. Based on this prior information, a low-rank matrix from the transfer matrix could be selected to identify the predefined locations force in this study. How to determine the suitable submatrix of the transfer matrix needs to be studied to ensure the identification accuracy and computational efficiency.

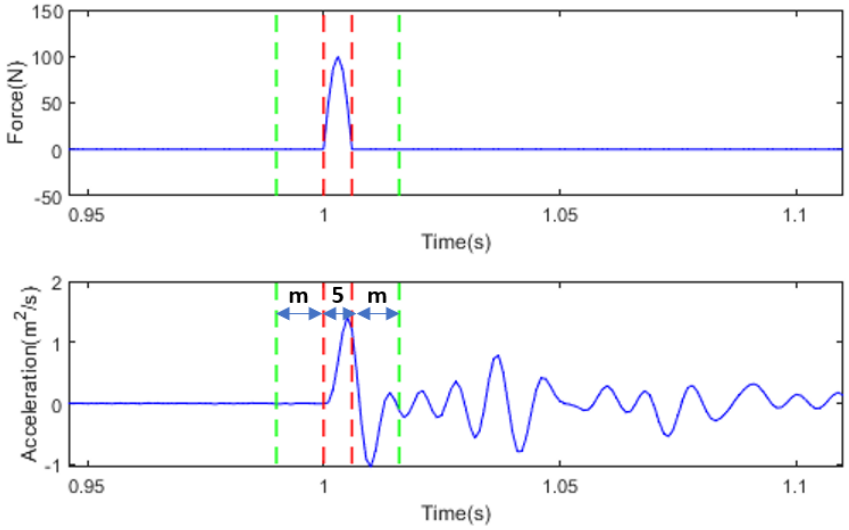

Figure 4.4 Impact excitation interval determination from acceleration responses

The impact force is assumed as a triangular pulse with the short time interval. For example, the time interval is 0.006 s and there are 5 nonzero values as the sampling rate is 0.001 s. To cover the excitation time interval, the corresponding submatrix from the transfer matrix should be determined. As shown in Figure 4.4, the $2m$ +5 values around the beginning of the response

are chosen to cover the force time interval. m is the selected number of values. In the simulations, the impact force is conducted at location P2. one sensor (Y1) response is used. 5% noise is added to the response to simulate the polluted measurement. The effect of the m value is discussed below. The m value is from 0 to 30 in this study.

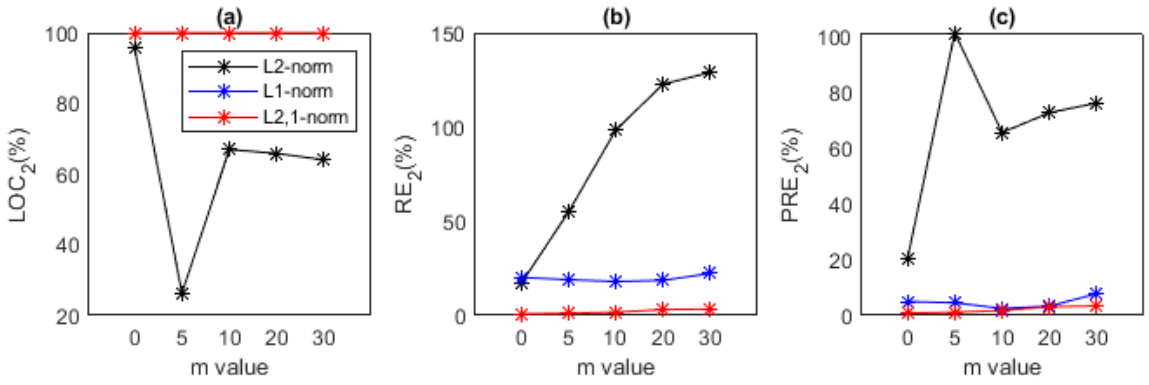

Figure 4.5 The identification index results under different range of partial matrix: (a) localization index LOC; (b) identification accuracy index RE; (c) identification accuracy index PRE

The proposed group sparse regularisation method with a low-rank submatrix is implemented for the impact force identification. The results are compared with that by the l_2-norm regularisation method and the l_1-norm regularisation method. Figure 4.5, and Tables 4.2 and 4.3 show the LOC values and the force identification accuracy RE and PRE with different sizes of submatrices. From Figure 4.5 and Table 4.2, both the l_1-norm regularisation method and the group sparse regularisation methods could identify the location of the impact force with different sizes of submatrices successfully. The l_2-norm regularisation method cannot localise the impact force when m=5 and 10. From Figures 4.5(b) and 4.5(c), and Tables 4.2 and 4.3, the identified error by the l_1-norm regularisation method reduces with the increase of the m value, and that by the group sparse regularisation method increases with the size of the submatrix. The errors by the proposed group sparse regularisation method are all below 4.5% and 1.3% for the RE and PRE values respectively. There are large errors by the l_2-norm regularisation

method. As the above, the proposed group sparse regularisation method has the best performance for the impact force localisation and identification.

Table 4.2 The LOC values with different sizes of submatrices

Force location (m)	Method	P1	P2	P3	P4	P5	P6	P7	P8	P9
	L2-norm	10.5	95.6	11.1	11.9	13.0	12.3	10.0	6.9	3.6
0	L1-norm	0.1	100.0	0.0	0.0	0.0	0.0	0.0	0.0	0.0
	L2,1-norm	0.3	100.0	0.2	0.1	0.1	0.2	0.1	0.1	0.1
	L2-norm	28.6	27.3	33.8	39.4	47.1	9.3	32.2	40.5	27.7
5	L1-norm	0.0	100.0	0.0	0.0	0.0	0.0	0.0	0.0	0.0
	L2,1-norm	0.4	100.0	0.4	0.3	0.2	0.4	0.4	0.3	0.3
10	L2-norm	28.7	18.8	34.8	41.2	48.4	9.1	33.3	40.5	27.3
	L1-norm	0.0	100.0	0.0	0.0	0.0	0.0	0.0	0.0	0.0
	L2,1-norm	0.7	100.0	0.8	0.3	0.4	0.6	0.6	0.5	0.3
20	L2-norm	50.5	65.8	27.6	22.1	19.8	22.7	20.6	18.0	14.6
	L1-norm	0.0	100.0	0.0	0.0	0.0	0.0	0.0	0.0	0.0
	L2,1-norm	0.4	100.0	0.5	0.2	0.2	0.4	0.4	0.3	0.2
30	L2-norm	47.7	64.0	27.2	21.4	20.8	26.0	23.0	22.4	17.1
	L1-norm	0.0	100.0	0.0	0.0	0.0	0.0	0.0	0.0	0.0
	L2,1-norm	0.7	100.0	1.0	0.5	0.5	0.7	0.7	0.6	0.4

Table 4.3 The RE and PRE values with different sizes of submatrices

	L2-norm		L1-norm		L2,1-norm	
m	RE%	PRE%	RE%	PRE%	RE%	PRE%
0	17.25	20.79	20.15	4.59	0.55	0.07
5	80.51	57.82	20.91	4.90	1.06	0.15
10	97.89	66.12	20.54	4.60	1.96	0.11
20	122.91	72.50	18.25	2.67	3.07	0.86
30	128.45	74.61	16.26	2.16	4.49	1.27

Figure 4.6 shows the identified results using the submatrix with m=5 by the l_1-norm regularisation method, the l_2-norm regularisation method and the proposed group sparse regularisation method. The corresponding identified results of the impact force location by these three methods are shown in Figures 4.7(a), 4.7(b) and 4.7(c), respectively and the reconstructed time histories of the impact force are shown in Figures 4.7(d), 4.7(e) and 4.7(f), respectively. The force vector is separated into 9 groups, each associated with one potential force location. Among the potential locations, only non-zero forces occur at the true force location. From Figure 4.6, the identified result by the proposed method is very close to the true value, and that by the l_1-norm regularisation method is close to the true value with some small oscillations. There are large oscillations in the result by the l_2-norm regularisation method and it fails to reconstruct the impact force. From Figures 4.7(a), 4.7(b) and 4.7(c), all three methods could indicate the location of the impact force. From Figures 4.7(b) and 4.7(c), the LOC values are close to zero except for 100% at the true force location by the l_1-norm and $l_{2,1}$-norm regularisation methods and the results show that the impact force location information could be extracted accurately using these two methods. Figure 4.7(d) shows that compared with the true value, the reconstructed impact force by the l_2-norm regularisation method has large errors, and the RE and PRE values are 80.51% and 57.82% respectively. In Figure 4.7(e), the identified result by the l_1-norm regularisation method has some oscillations around the force peak, and the RE and PRE values are 20.91% and 4.90% respectively. From Figure 4.7(f), the result by the proposed $l_{2,1}$-norm regularisation method fits well with the true force, and the RE and PRE values are 1.06% and 0.15% respectively. From the above, the impact force location and values could be accurately identified simultaneously with one sensor by this proposed transfer submatrix based group sparse regularisation method.

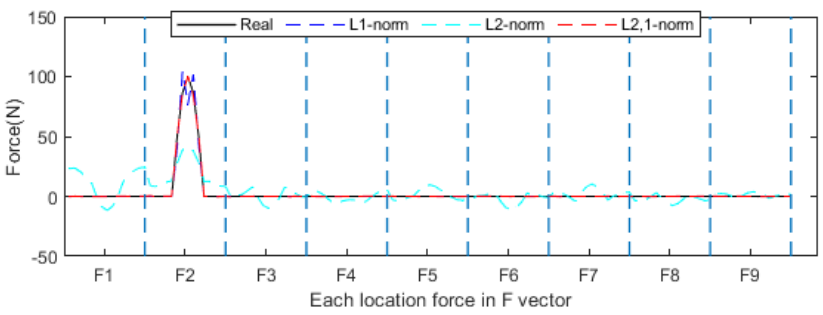

Figure 4.6 Identified force vector divided into predefined groups

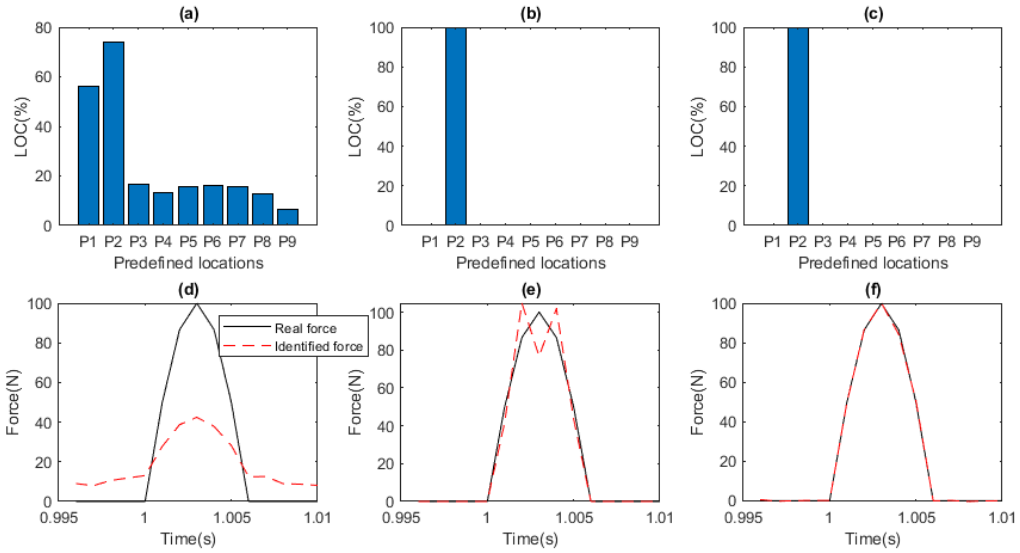

Figure 4.7 The results of impact force identification with the submatrix of m=5: the localization index results: (a) using L2-norm regularisation; (b) using L1-norm regularisation; (c) using L2,1-norm regularisation; impact force time history reconstruction at real location results: (d) via L2-norm regularisation; (e) via L1-norm regularisation; (f) via L2,1-norm regularisation.

4.4.3 Effect of measurement noise

To study the effect of measurement noise, the white noise is added to the calculated responses to simulate the polluted measurements, and 1%, 3%, 5%, 10% and 15% noise levels are studied. One single sensor response is used for the impact force identification. Transfer submatrix for this section with m =5 is employed. The impact force is the same as that in Section 4.4.2. The

LOC, and RE and PRE values are listed in Tables 4.4 and 4.5. Figures 4.8(a), 4.8(b) and 8(c) show the LOC, RE and PRE values with different measurement noise levels using three methods. The reconstruction time history results from the responses with different measurement noise levels using three methods are shown in Figures 4.8(d), 4.8(e) and 4.8(f) respectively.

Table 4.4 Localization index LOC results under different noise levels

Impact location		P1	P2	P3	P4	P5	P6	P7	P8	P9
	L2-norm	56.2	73.7	16.9	13.1	15.9	15.9	15.6	12.6	6.8
1%	L1-norm	0.0	100.0	0.0	0.0	0.0	0.0	0.0	0.0	0.0
	L2,1-norm	0.1	100.0	0.1	0.0	0.1	0.1	0.1	0.1	0.1
	L2-norm	56.2	73.7	16.7	13.2	15.9	15.9	15.5	12.6	6.9
3%	L1-norm	0.0	100.0	0.0	0.0	0.0	0.0	0.0	0.0	0.0
	L2,1-norm	0.2	100.0	0.2	0.1	0.1	0.2	0.1	0.2	0.1
	L2-norm	56.1	73.8	16.9	13.0	16.0	16.1	15.6	12.6	6.8
5%	L1-norm	0.1	100.0	0.0	0.0	0.0	0.0	0.0	0.0	0.0
	L2,1-norm	0.2	100.0	0.2	0.1	0.1	0.1	0.1	0.1	0.1
	L2-norm	56.0	73.6	17.4	12.9	15.9	16.5	15.7	12.8	6.7
10%	L1-norm	1.2	100.0	0.8	0.2	1.0	0.0	0.6	0.2	0.3
	L2,1-norm	0.9	100.0	0.9	0.5	0.7	0.6	0.6	0.5	0.6
	L2-norm	55.9	73.5	17.3	13.2	16.0	16.3	15.8	13.0	7.2
15%	L1-norm	0.8	100.0	0.9	0.0	0.7	0.7	0.2	0.0	0.1
	L2,1-norm	1.2	100.0	1.2	0.8	0.5	0.9	0.9	0.7	0.8

Table 4.5 Identification accuracy index RE and PRE results under different noise levels

Noise	L2-norm		L1-norm		L2,1-norm	
	RE%	PRE%	RE%	PRE%	RE%	PRE%
1%	80.33	57.42	24.97	8.06	0.93	0.32
3%	80.44	57.43	23.38	6.53	1.02	0.32
5%	81.11	58.65	21.81	5.88	0.61	0.43
10%	79.97	59.74	17.87	3.17	4.61	3.30
15%	81.65	59.85	20.31	3.22	5.55	3.42

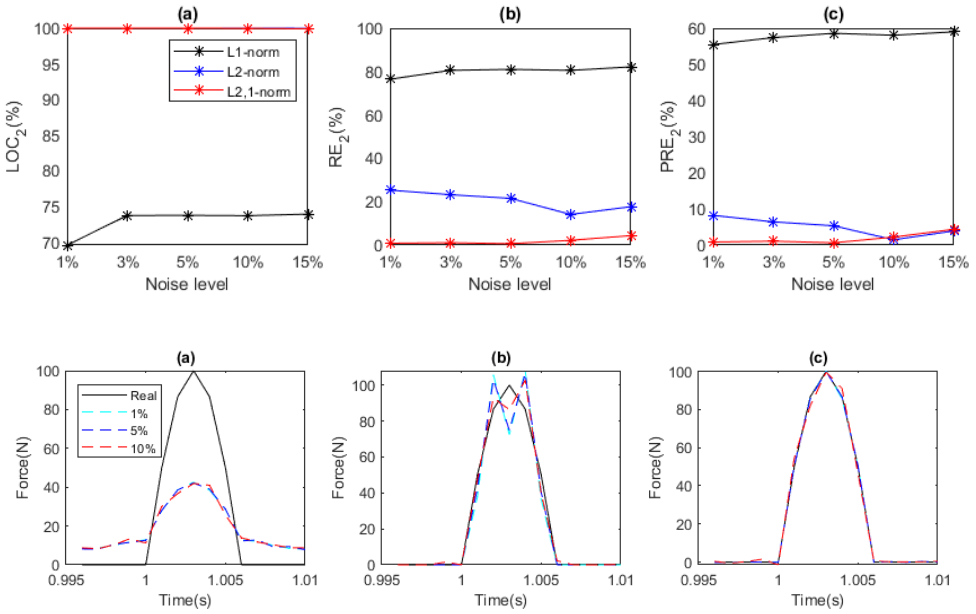

Figure 4.8 The results of impact force identification under different noise effect: The identification index results: (a) localization index LOC; (b) identification accuracy index RE; (c) identification accuracy index PRE; impact force time history reconstruction at real location results under 1%, 5% and 10% noise effect results: (d) via L2-norm regularisation; (e) via L1-norm regularisation; (f) via L2,1-norm regularisation.

From Figure 4.8(a) and Table 4.4, all three methods could indicate the location of the impact even with 15% measurement noise. The LOC values by the l_1-norm and $l_{2,1}$-norm regularisation methods are 100% at the true location and others are close to zero. The LOC value by the l_2-norm regularisation method is around 70% and the values are not zero at other locations. From Figures 8(b) and 8(c), the RE and PRE values are approximate the same for different noise levels. And it shows that all three methods are robust to the measurement noise. From Table 4.5, the RE and PRE values of the proposed method are smallest with 5.55% and 3.42% when the measurement noise is 15%. It shows that the proposed method is robust to the measurement noise and has the highest accuracy for the impact force reconstruction. Figures 4.8(d), 4.8(e) and 4.8(f) shows the identified impact forces from the response measurements with different noise levels. The results also confirm that the measurement noise does not have a big influence

on the identified results. There is a big error in the force amplitude by the l_2-norm regularisation method, as shown in Figure 4.8(d), and this is due to the smoothing effect of the l_2-norm. From Figure 4.8(e), there are some oscillations around the peak of the impact force. The identified results by the proposed $l_{2,1}$-norm regularisation method agree well with the true values as shown in Figure 4.8(f).

4.4.4 Multiple impact force identification with one single sensor

In practice, multiple impact forces usually appear at different locations asynchronously. The identification of two and three impact forces using the proposed method is studied in this section. For the case with two impact forces, these impact forces are applied at the locations P2 and P4 separately. The response of one single sensor (Y1) shown in Figure 4.9 is employed. 5% noise is added to the response to simulate the polluted measurement. The interval between two adjacent green dash lines in Figure 4.9 associated the transfer submatrix is selected for the localization and reconstruction of the corresponding impact force. There are two intervals corresponding to two impact forces.

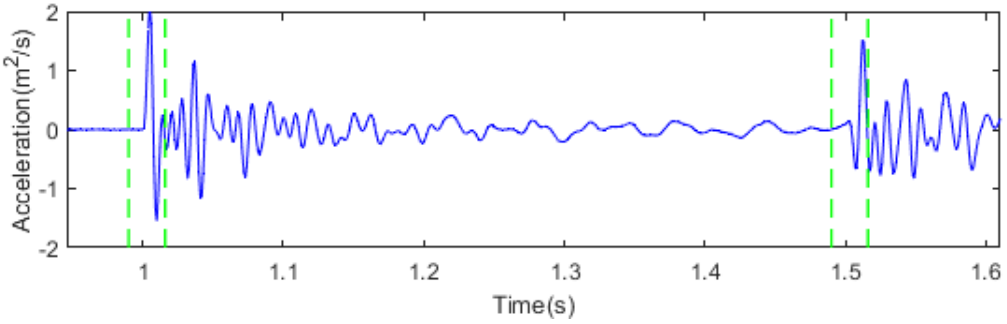

Figure 4.9 Acceleration time history response for estimation of two intervals related to impact forces

The identified force vector results based on the proposed method are illustrated in Figure 4.10. The corresponding localization results of two impact forces by three methods are shown in Figures 4.11(a), 4.11(b) and 4.11(c) respectively. The reconstructed time histories of two impact force are shown in Figures 4.11(d) and 4.11(e) respectively. Location index LOC and

identification accuracy indices RE and PRE are listed in Tables 4.6 and 4.7. From Figure 4.10, the locations of two impact forces F2 and F4 could be identified successfully by the l_1-norm regularisation method and the proposed $l_{2,1}$-norm regularisation method. The identified result by the l_2-norm regularisation method contains highly oscillatory false components at other locations and these oscillations affect the accuracy of the impact force identification. From Table 4.6, the LOC values at locations of these two impacts are all 70% or above by the l_1-norm regularisation method and the proposed $l_{2,1}$-norm regularisation method and the results show that the impact forces could be accurately located. The LOC values for two impact forces are only 57.5% and 42.5% by the l_2-norm regularisation method respectively. Figures 4.11(d) and 4.11(e) show the identified impact force time histories by three methods. The identified results of two impact forces by the $l_{2,1}$-norm regularisation method are close to the true values. The identified result of the impact force at P2 by the l_1-norm regularisation method is close to the true value and there are some oscillations at the identified result of the impact force at P4. This is probably induced by the initial response condition for the second impact force. For the first impact force conducted at P2, the initial response is zero. While for the second impact force at P4, the initial response is non-zero and it may affect the second force identification. There is no this effect by the proposed $l_{2,1}$-norm regularisation method as shown in Figures 4.11(d) and 4.11(e). Accurate force time history for both impact forces are obtained using this proposed method.

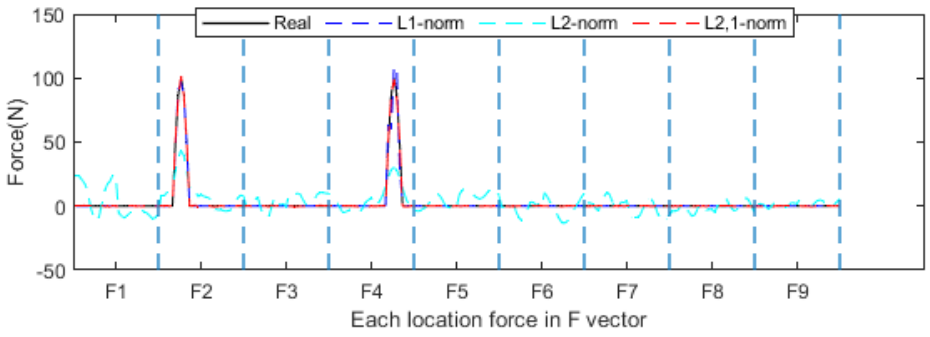

Figure 4.10 Identified force vector for double impact divided into predefined groups

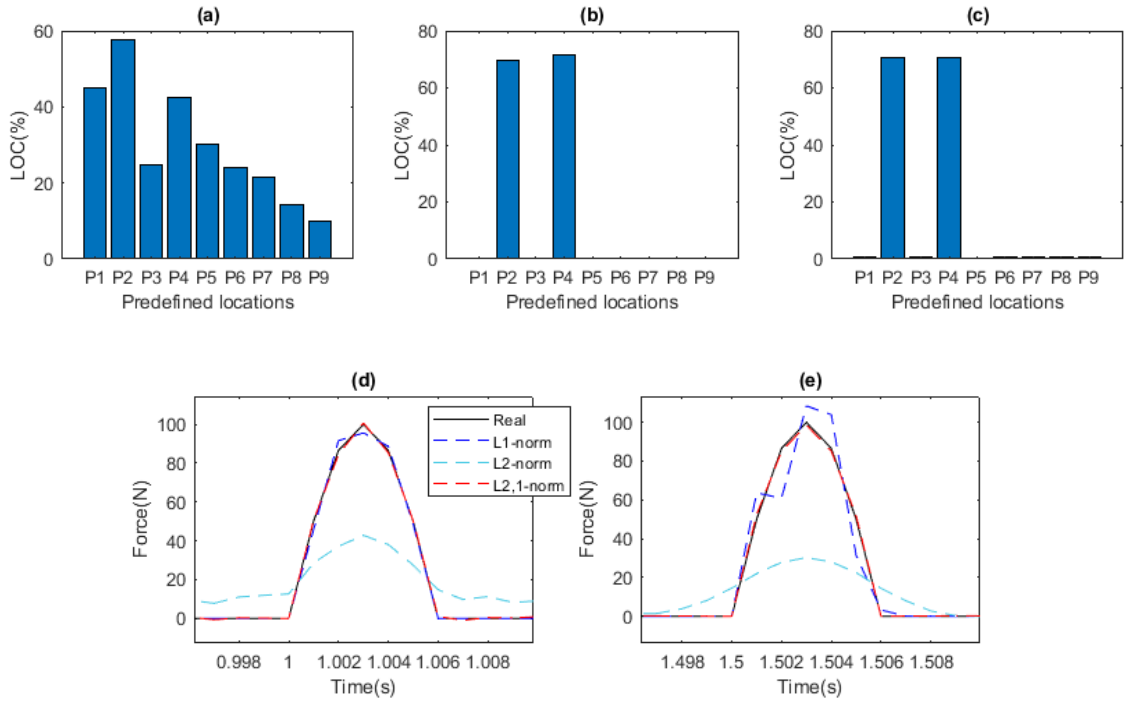

Figure 4.11 The results of double impact force identification: the localization index results: (a) using L2-norm regularisation; (b) using L1-norm regularisation; (c) using L2,1-norm regularisation; impact force time history reconstruction at real location results: (d) identified impact force at P2; (e) identified impact force at P4

For the case of three impact force identification, three impact forces are applied at locations P2, P4 and P6 separately. One single sensor (Y1) response shown in Figure 4.12 is employed. 5% noise is added to the response to simulate the polluted measurement. Three intervals indicated by green dash lines in Figure 4.12 associated transfer submatrices are selected for three impact force localization and reconstruction.

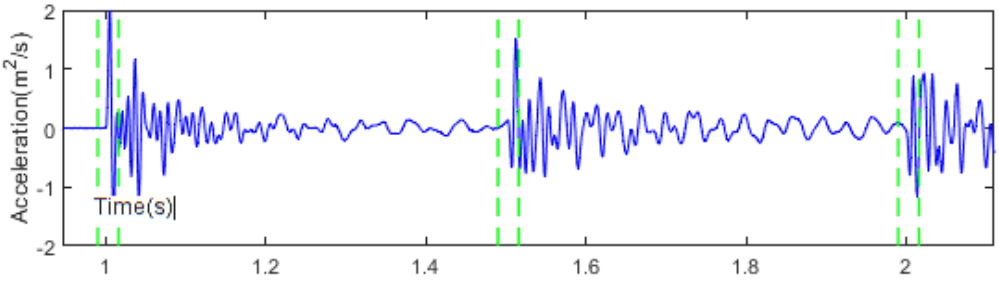

Figure 4.12 Acceleration time history for triple excitations interval determination

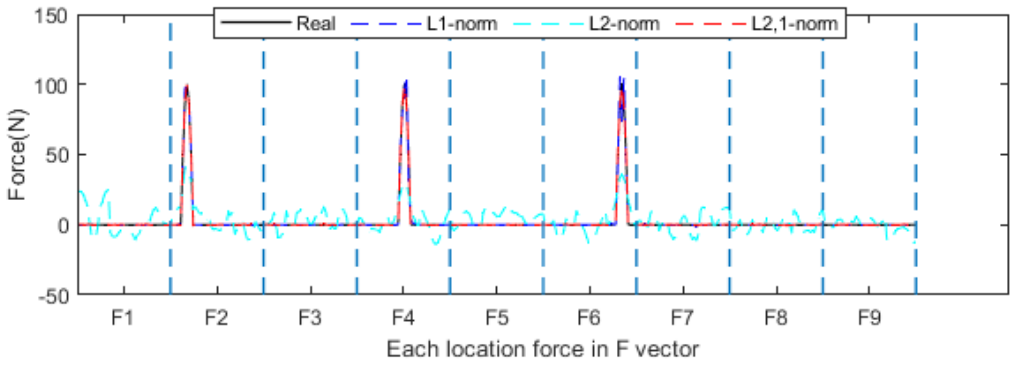

Figure 4.13 Identified force vector for triple impacts divided into predefined groups

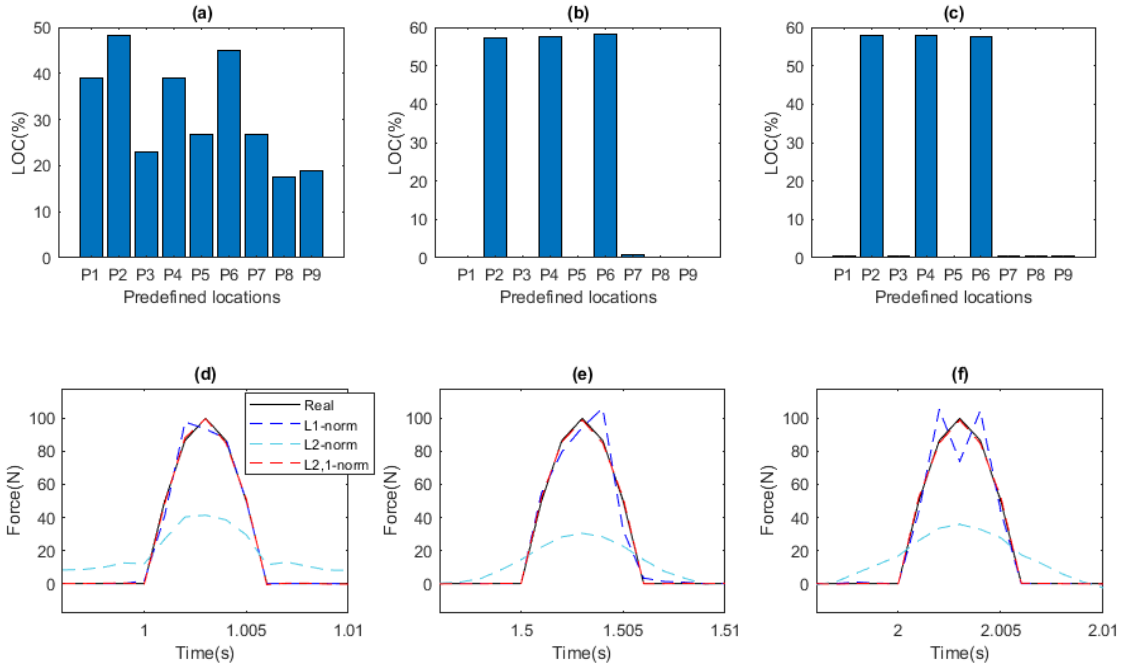

Figure 4.14 The results of triple impact force identification: the localization index results: (a) using L2-norm regularisation; (b) using L1-norm regularisation; (c) using L2,1-norm regularisation; impact force time history reconstruction at real location results: (d) identified impact force at P2; (e) identified impact force at P4; (e) identified impact force at P6

From Eq. (4.13), the distance and the amplitude ratio of two forces do not have the effect of the identified results. Here three forces with the same amplitude and distance are used to verify the proposed method. The identified force vector results based on the proposed method are illustrated in Figure 4.13. The corresponding localization results by three methods are shown

in Figures 4.14(a), 4.14(b) and 4.14 (c) respectively. The reconstructed time histories of three impact forces by three methods are shown in Figures 4.14(d), 4.14(e) and 4.14 (f) respectively. The corresponding LOC, RE and PRE values are listed in Tables 4.6 and 4.7. From Figures 4.13 and 4.14, and Tables 4.6 and 4.7, three impact force forces are located successfully by the l_1-norm regularisation method and the proposed $l_{2,1}$-norm regularisation method and the identified results of three impact forces by the proposed method are all close to the true values. The proposed transfer submatrix based the $l_{2,1}$-norm regularisation method has a good performance on multiple impact force localization and reconstruction.

Table 4.6 Localization index LOC results for different number of impact force

Impact location		P1	P2	P3	P4	P5	P6	P7	P8	P9
1	L2-norm	56.1	73.8	16.9	13.0	16.0	16.1	15.6	12.6	6.8
	L1-norm	0.1	100.0	0.0	0.0	0.0	0.0	0.0	0.0	0.0
	L2,1-norm	0.2	100.0	0.2	0.1	0.1	0.1	0.1	0.1	0.1
2	L2-norm	45.2	57.5	24.7	42.5	30.0	23.9	21.4	14.3	9.9
	L1-norm	0.0	69.9	0.0	71.6	0.0	0.2	0.0	0.0	0.0
	L2,1-norm	0.7	70.7	0.8	70.7	0.4	0.7	0.6	0.6	0.6
3	L2-norm	39.0	48.2	23.1	38.9	26.7	44.8	26.9	17.4	18.9
	L1-norm	0.2	57.2	0.3	57.7	0.0	58.3	0.7	0.2	0.1
	L2,1-norm	0.5	57.8	0.6	57.7	0.2	57.6	0.5	0.4	0.4

Table 4.7 Identification accuracy index RE and PRE results for different number of impact force

Impact number	Impact position	L2-norm		L1-norm		L2,1-norm	
		RE%	PRE%	RE%	PRE%	RE%	PRE%
1	P2	81.11	58.65	21.81	5.88	0.61	0.43
2	P2	99.78	57.20	4.59	4.39	1.60	0.69
	P4	46.87	69.73	11.66	8.47	1.74	1.32
3	P2	59.11	58.61	4.07	2.21	2.05	0.27
	P4	62.21	69.56	8.10	6.21	1.63	0.95
	P6	40.34	64.19	6.87	5.36	1.33	1.06

4.5 Experimental validation

4.5.1 Experimental setup

To further verify the effectiveness and applicability of the proposed method, the experimental study is performed on a steel-concrete composite bridge model shown in Figure 4.15. The detail information of the bridge is listed in Chapter 3. 28 possible impact force locations are predefined and labelled from S1 to S14 and N1 to N14 shown in Figure 4.16. The impact hammer (PCB 086D20 with sensitivity 0.23 mV/N) is used for the excitation. NI data acquisition system is used to record the impact force and acceleration response data with a sampling frequency 1000Hz. The acceleration response from A1 is used for the impact force identification. Single force (conducted at S4) identification and two force (conducted at S4 and S6) identification are conducted in this section. The transfer matrix can be constructed according to the procedure. The transfer submatrix associated with the impact force time interval could be selected for the loading interval force identification.

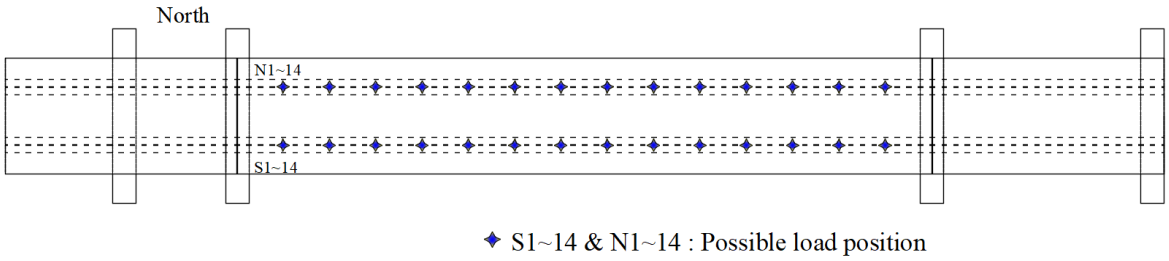

Figure 4.16 Predefined possible load position in the experiment model

4.5.2 Results and discussion

The proposed transfer submatrix-based group sparse method is used to identify the impact force and the results are compared with that by the l_2-norm and l_1-norm regularisation methods.

Figure 4.17 shows the single impact force localization and reconstruction results from one single response. Figures 4.17(a), 4.17(b) and 4.17(c) show the identified location of the impact force using three methods respectively. Figures 4.17(d), 4.17(e) and 4.17 (f) show the

corresponding identified impact force time histories respectively. From Figures 4.17(a)-4.17(c), the location of the impact force is clearly indicated by the peaks of the results by the l_1-norm regularisation method and $l_{2,1}$-norm regularisation method. There is no clear peak by the l_2-norm regularisation method and it shows that the method fails to obtain the clear location information. From Figures 4.17(d)- 4.17(f), the identified result by the proposed method is much closer to the true value compared with that by other two methods. There is a big error of the impact force amplitude by the l_2-norm regularisation method. From Figures 4.17(b) and 4.17(e), the impact force localization is slightly affected by other potential positions and the impact force time history identification is less accurate by the l_1-norm regularisation method comparing with the proposed method.

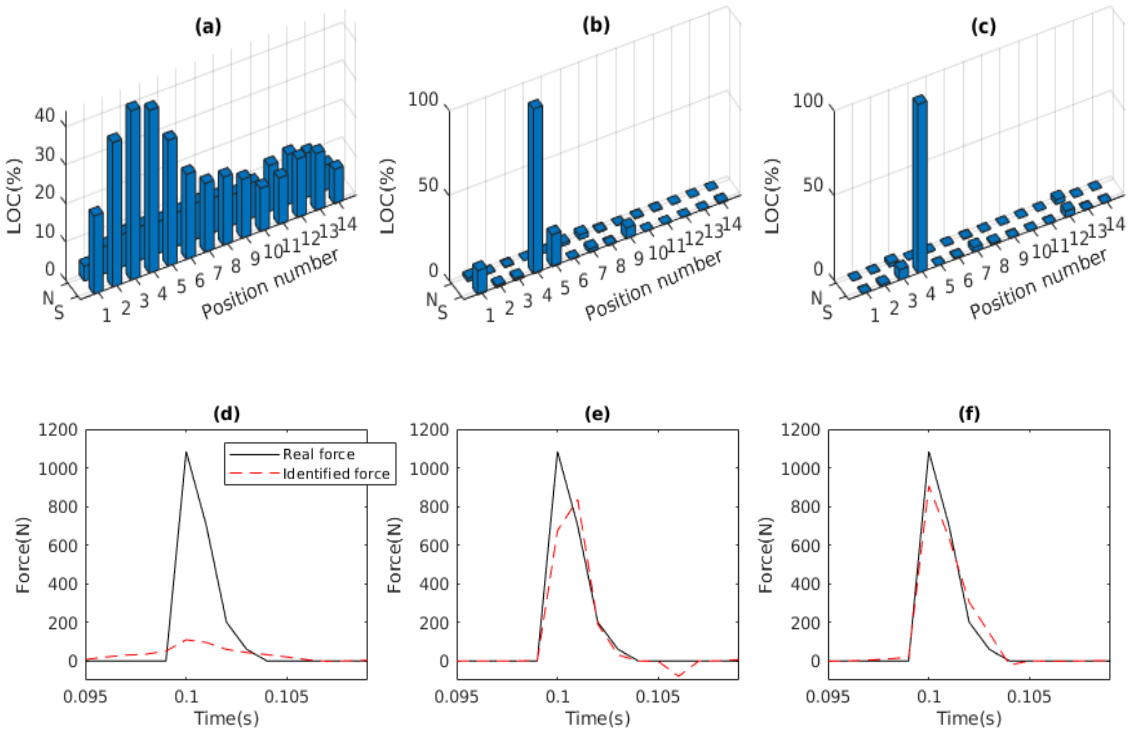

Figure 4.17 Experimental results of single impact force identification at location S4: the localization index results: (a) using L2-norm regularisation; (b) using L1-norm regularisation; (c) using L2,1-norm regularisation; impact force time history reconstruction at real location

results: (d) via L2-norm regularisation; (e) via L1-norm regularisation; (f) via L2,1-norm regularisation.

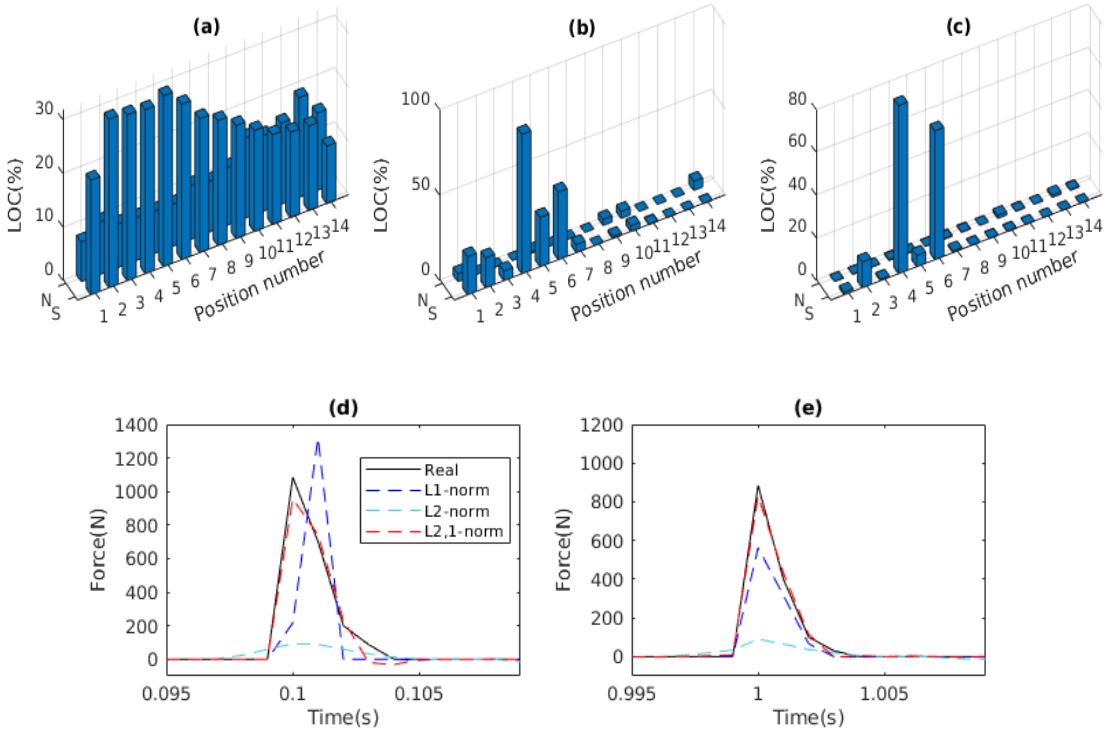

Figure 4.18 Experimental results of double impact force identification: the localization index results: (a) using L2-norm regularisation; (b) using L1-norm regularisation; (c) using L2,1-norm regularisation; impact force time history reconstruction at real location results: (d) identified impact force at S4; (e) identified impact force at S6

The same accelerometer (A2) is used to identify two impact forces at S4 and S6 separately. The LOC values by three methods are shown in Figures 4.18(a), 4.18(b) and 4.18(c) respectively. The reconstructed time histories of these two impact forces are shown in Figures18(e) and 18(f). Figures 4.18(a), 4.18(d) and 4.18(e) show that two impact forces are not able to be located and reconstructed by the l_2-norm regularisation method. Figure 4.18(b) shows that two impact forces could be located correctly and the LOC value for the second force is less than 50%. From Figures 4.18(d) and 4.18(e), the identified first impact force is larger that the true value and the identified second impact force is smaller than the true value by the

l_1-norm regularisation method. That means the first force is overestimated and the second one is underestimated. From Figures 4.18(c), 4.18(d) and 4.18(e), by the proposed $l_{2,1}$-norm regularisation method, these two impact forces are clearly located by two peaks and the identified results are much close to the true values. The results show that the proposed method has good robustness and accuracy for two impact force identification.

4.6 Summary

In this paper, the transfer submatrix-based group sparse regularisation method for multiple impact force localization and reconstruction is proposed. Based on the intrinsic feature of impact force, the transfer submatrix associated with the impact excitation time interval could be constructed for the loading interval force identification. By this method, the dimension of the inverse problem can be dramatically decreased, and the computational efficiency can be significantly improved. It could also improve the ill-posedness of the inverse problem, especially when the number of sensors is less than the number of impact forces. The force vector could be grouped based on the potential force locations. The proposed method could obtain stable and accurate results based on the structured group sparsity in the force vector. The group sparse regularisation method based on the $l_{2,1}$-norm penalty is validated and compared with the l_1-norm regularisation method and the l_2-norm regularisation method numerically and experimentally. In the numerical study, determination of the submatrix, noise effect and multiple impacts identification are investigated using one single sensor response. Suitable submatrix is determined. Comparing with the l_1-norm and l_2-norm regularisation methods, the proposed transfer submatrix-based group sparse regularisation method has the best performance on the multiple impact force localization and time history reconstruction.

Chapter 5 Moving force identification via equivalent nodal force based on group weighted regularisation

5.1 Overview

Most existing methods on moving force identification are usually based on modal decomposition and are subject to modal truncation error in the dynamic responses. These methods are all based on the continuous system and modal superposition technique, and they cannot be applied to complicated structures directly (Zhu and Law, 2016). To solve this problem, one group weighted Tikhonov regularisation method is proposed for moving force identification via equivalent nodal force. The moving force could be transferred into equivalent nodal force, which has the group sparse feature. A new method will be developed for moving force identification. Its effectiveness and applicability are studied numerically on a simply supported beam in comparison with the standard sparse regularisation method and the classical Tikhonov regularisation method. The method could be further extended for complicated bridge structures.

5.2 Governing equation of moving force identification via equivalent nodal force

Figure 5.1 shows a simple supported beam subjected to one moving force. Suppose a simply supported beam bridge is assumed to be an Euler-Bernoulli beam and discretised into n equally spaced elements with $n + 1$ nodes.

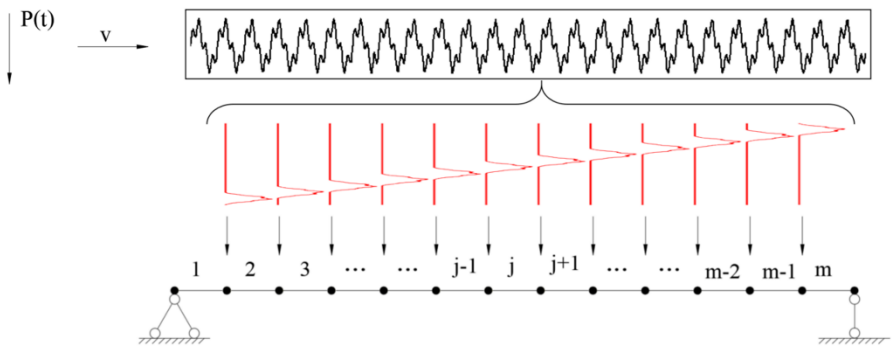

Figure 5.1 Simply supported beam subjected to equivalent nodal force transferred from one moving force

Thus, the equation of motion of the bridge under moving forces can be written as:

$$\boldsymbol{M}\ddot{\boldsymbol{x}}(t) + \boldsymbol{C}\dot{\boldsymbol{x}}(t) + \boldsymbol{K}\boldsymbol{x}(t) = \boldsymbol{F}(t) \tag{5.1}$$

$$\boldsymbol{F}(t) = \boldsymbol{L}(t)\boldsymbol{P}(t) \tag{5.2}$$

where $\boldsymbol{M}$, $\boldsymbol{M}$ and $\boldsymbol{K}$ are the mass, damping and stiffness matrices of the bridge, respectively; $\ddot{\boldsymbol{x}}(t)$, $\dot{\boldsymbol{x}}(t)$and $\boldsymbol{x}(t)$ are vectors of the acceleration, velocity and displacement responses of the bridge at each time instant, respectively; and $(\boldsymbol{L}(t)\boldsymbol{P}(t))_{n_{dof}\times 1}$ is the equivalent global force vector at each time instant, n_{dof} is the number of degrees-of-freedom of the bridge after considering the boundary condition, $\boldsymbol{P}(t) = \{P_1(t), \cdots, P_{Np}(t)\}^T$ is the moving forces vector on the bridge, $\boldsymbol{L}(t)$ is a $n_{dof} \times Np$ time-varying matrix to transfer the moving force to equivalent nodal force.

According to the beam element type, Hermitian cubic interpolation shape functions are used here to construct the transformation matrix $\boldsymbol{L}(t)$. The shape functions of the *i*th element in its local coordinate can be obtained as follows:

$$N_i = \left[1 - 3\left(\frac{x}{l}\right)^2 + 2\left(\frac{x}{l}\right)^3, x\left(\frac{x}{l} - 1\right)^2, 3\left(\frac{x}{l}\right)^2 - 2\left(\frac{x}{l}\right)^3, x\left(\frac{x}{l}\right)^2 - \frac{x^2}{l}\right]^{\boldsymbol{T}} \tag{5.3}$$

where l is the length of the beam element; x is the moving force location in the element.

When the number of moving force Np is 2 and the moving forces are acting on ith and jth element respectively, the transformation matrix $\boldsymbol{L}(t)$ can be expressed as

$$\boldsymbol{L}(t) = \begin{bmatrix} 0 \cdots 0 \cdots N_i\big(x(t)\big) \cdots 0 \\ 0 \cdots N_j\big(x(t)\big) \cdots 0 \cdots 0 \end{bmatrix}^T \tag{5.4}$$

The equation of motion of the bridge system in Eq. (5.1) can be expressed in the state space as Eq. (4.2). The equivalent nodal force identification has the same derivation process with chapter 4. This inverse problem of equivalent nodal force identification could be expressed in Eq. (4.10).

It is noticed that in most practical applications, a noiseless measurement process rarely occurs and actual measurements are invariably contaminated by some noise. The inverse problem of equivalent nodal force identification with noisy response takes the following form

$$\mathbf{Y} = \mathbf{HF} + \mathbf{e} \tag{5.5}$$

where the vector $\mathbf{e}$ represents the inevitable measurement error that corrupts the actual response $\mathbf{Y}$. As for this kind of inverse problem, some regularisation strategies can be used. To stabilize the results of this equivalent nodal force identification, the feature of the force vector $\mathbf{F}$ could be considered in the regularisation methods.

5.3 Group weighted Tikhonov (GWT) regularisation model for equivalent force identification

In this section, we will discuss the proposed regularisation model for the inverse problem of equivalent nodal force identification.

Tikhonov regularisation seeks for a stable solution by introducing an l_2-norm penalty with controlling highly oscillating components. Hence, the regularized force identification problem defining a trade-off between the residual and regularized norms is written as

$$\underset{\boldsymbol{F}}{\text{Minimize}} \qquad \|\mathbf{HF} - \mathbf{Y}\|_2^2 + \|\boldsymbol{\Gamma}\mathbf{F}\|_2^2 \tag{5.6}$$

For some suitably chosen Tikhonov matrix $\boldsymbol{\Gamma}$. In many cases, this matrix is chosen as a scalar multiple of the identity matrix ($\boldsymbol{\Gamma} = \lambda \boldsymbol{I}$) giving preference to solutions with smaller norms; this is known as l_2 regularisation.

$$\underset{\boldsymbol{F}}{\text{Minimize}} \qquad \|\mathbf{HF} - \mathbf{Y}\|_2^2 + \lambda \|\mathbf{F}\|_2^2 \tag{5.7}$$

where $\lambda > 0$ is named the regularisation parameter. The l_2-norm of the force $\|\boldsymbol{F}\|_2^2$ is called the regularisation term or the penalty term. Here, the ill-posed model in Eq. (5.5) is improved thanks to the introduction of an additional term in Eq. (5.7), rendering the problem less sensitive to perturbations. Due to the convexity of Eq. (5.7), Tikhonov regularisation always has an analytic solution with any fixed λ

$$\boldsymbol{F} = (\mathbf{H}^T\mathbf{H} + \lambda \mathbf{I})^{-1}\mathbf{H}^T\mathbf{Y} \tag{5.8}$$

Since Eq. (5.8) treats each variable equally, it will introduce more errors especially in the zero entries of equivalent nodal force. To better utilize the intrinsic feature of equivalent loads shown in Figure 5.2, one group weighted matrix $\mathbf{W}$ is introduced to eliminate the effect of zero entries. The equivalent load could be expressed in Eq. (5.9).

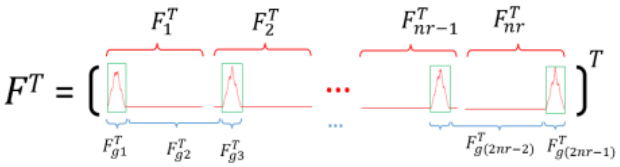

Figure 5.2 Equivalent nodal force features

$$\boldsymbol{F} = \mathbf{W}\boldsymbol{F} \tag{5.9}$$

where $\mathbf{W} = \text{diag}(\mathbf{w}_{g1}, \mathbf{w}_{g2}, \mathbf{w}_{g3}, \ldots, \mathbf{w}_{g(2nr-1)})$; $\mathbf{w}_{g(2i-1)} = diag(1,1,1,\cdots,1); i = 1,2,\cdots,\text{nr}$; $\mathbf{w}_{g(2i)} = diag(0,0,0,\cdots,0); i = 1,2,\cdots,\text{nr}$;

Then the Eq. (5.7) could be expressed as,

$$\underset{\boldsymbol{F}}{\text{Minimize}} \qquad \|\mathbf{HWF} - \mathbf{Y}\|_2^2 + \lambda \|\mathbf{WF}\|_2^2 \tag{5.10}$$

Eq. (5.10) has the analytic solution as,

$$\boldsymbol{F} = ((\mathbf{HW})^T(\mathbf{HW}) + \lambda\mathbf{I})^{-1}(\mathbf{HW})^T\mathbf{Y} \tag{5.11}$$

Eq. (5.11) can be analyzed in a special way using the singular-value decomposition. Given the singular value decomposition

$$\mathbf{HW} = \mathbf{U\Sigma V}^T \tag{5.12}$$

where $\mathbf{U} = [\boldsymbol{u}_1, \cdots, \boldsymbol{u}_m]$; $\mathbf{V} = [\boldsymbol{v}_1, \cdots, \boldsymbol{v}_n]$; $\mathbf{\Sigma} = \mathrm{diag}(\sigma_1, \cdots, \sigma_r)$, r is the rank of matrix $\mathbf{HW}$ with singular value decomposition, the regularized solution can be expressed as

$$\boldsymbol{F} = (\mathbf{V\Sigma U}^T\mathbf{U\Sigma V}^T + \lambda\mathbf{I})^{-1}\mathbf{V\Sigma U}^T\boldsymbol{Y} \tag{5.13}$$

with singular values,

$$\boldsymbol{F} = \sum_{i=1}^{r} \frac{\sigma_i}{{\sigma_i}^2+\lambda} \boldsymbol{u}_i{}^T\boldsymbol{Y}\boldsymbol{v}_i \tag{5.14}$$

As above procedure, the equivalent loads can be identified from the measured structural responses. After that, the vehicle moving load is expected to be estimated from the identified equivalent loads as follows,

$$\boldsymbol{F}_{sum} = \sum_{i=1}^{Np} \boldsymbol{P}_i = \sum_{i=1}^{Nr} \boldsymbol{F}_i \tag{5.15}$$

where $\boldsymbol{F}_{sum}$ is a vector representing the sum of the identified equivalent loads; Nr is the number of equivalent loads; Np is the number of moving force

5.4 Numerical study

5.4.1 Simulation parameters

To evaluate the performance of the proposed algorithm method, a simple supported beam model is adopted. The beam model is concerned with a one-dimensional structure with length of 32 m, cross section of 1m×0. 3m and mass density of 3500 kg/m^3. The Young's modulus E of the beam material is 2.05×10^{11}N/m^2, and the structural damping is considered as Rayleigh damping in the beam model with α=0.5, β=1. The beam model is divided into 300 equal Euler-Bernoulli finite elements. The dynamic response of the beam is calculated with a time interval of 0.001s and measurement duration of 4s. A vehicle with one axle moves across the bridge

with a constant speed such as 4 m/s. The time history of one axle induced moving force is simulated as a sum of an axle weight and a time-varying component such as:

$$p(t) = 20000 * (1 + 0.1\sin(10\pi t) + 0.05\sin(40\pi t)) \tag{5.16}$$

where $p(t)$ represent the time history of moving force.

The effects of number of measuring points, number of equivalent load and noise level on the accuracy of the identified results are investigated. Cases are listed in Table 5.1. As shown in the table, as the speed of the moving force is constant, the position of equivalent loads are constant. The calculated responses are polluted with white noise to simulate the polluted measurement as:

$$\mathbf{Y}_n = \mathbf{Y} + lev \times \frac{1}{n}\sum_{i=1}^{n}|\mathbf{Y}| \times \boldsymbol{rand} \tag{5.17}$$

where $\mathbf{Y_n}$ and $\mathbf{Y}$ are the structural responses corresponding to noise and noiseless, respectively. n is the total number of elements in the vector $\mathbf{Y}$. lev is the noise level. $\boldsymbol{rand}$ is a standard normal distribution vector.

Table 5.1 Cases for moving force identification

Cases	Position of sensors	Positions of equivalent loads
1	L/4, 2L/4, 3L/4	L/6, 2L/6, 3L/6, 4L/6, 5L/6
2	L/6, 2L/6, 3L/6, 4L/6, 5L/6	L/6, 2L/6, 3L/6, 4L/6, 5L/6
3	L/8, 2L/8, 3L/8, 4L/8, 5L/8, 6L/8, 7L/8	L/6, 2L/6, 3L/6, 4L/6, 5L/6
4	L/6, 2L/6, 3L/6, 4L/6, 5L/6	L/4, 2L/4, 3L/4
5	L/6, 2L/6, 3L/6, 4L/6, 5L/6	L/8, 2L/8, 3L/8, 4L/8, 5L/8, 6L/8, 7L/8
6	L/6, 2L/6, 3L/6, 4L/6, 5L/6	L/10, 2L/10, 3L/10, 4L/10, 5L/10, 6L/10, 7L/10, 8L/10, 9L/10

To evaluate the identified equivalent load accuracy, a relative percentage error for each location between actual force vector $\mathbf{F}_i$ and the estimated one $\widetilde{\mathbf{F}}_i$ is defined as

$$RE_i = \frac{\|\mathbf{F}_i - \widetilde{\mathbf{F}}_i\|_1}{\|\mathbf{F}_i\|_1} \times 100\% \tag{5.18}$$

where $\widetilde{\mathbf{F}}_i$ and $\mathbf{F}_i$ is ith identified and true equivalent load respectively.

To evaluate the global accuracy of identified moving force, a global relative percentage error is defined as

$$GRE = \frac{\|\mathbf{P} - \tilde{\mathbf{P}}\|_1}{\|\mathbf{P}\|_1} \times 100\% \tag{5.19}$$

where $\tilde{\mathbf{P}}$ and $\mathbf{P}$ is identified and true moving force respectively. The GRE value could be calculated by the ration between the l_1 norm of the difference between the predicted and true forces and that of the true force.

Since the sum of equivalent loads has the drawbacks to identify the moving force at the boundary position. In order to have a better evaluation for the accuracy of identified moving force, A relative percentage error for middle part moving force is defined as

$$MRE = \frac{\|\mathbf{P}_m - \tilde{\mathbf{P}}_m\|_1}{\|\mathbf{P}_m\|_1} \times 100\% \tag{5.20}$$

where $\tilde{\mathbf{P}}_m$ and $\mathbf{P}_m$ is identified and true middle part moving force respectively.

5.4.2 The effect of the number of measurements

Five equivalent loads are considered, and their positions are set as L/6, 2L/6, 3L/6, 4L/6, 5L/6, respectively. As listed in Table 5.1, three cases (Case1, Case2, Case3) with considering different number of sensors are used for analysis. 5% noise level is considered. The proposed group weighted regularisation method is implemented for the equivalent loads identification. The results are compared by the Tikhonov regularisation method and l_1-norm regularisation method. The acceleration responses induced by the moving force include the high-frequency components and the signal-to-noise ratio for the high frequency components is low. So the identified results by the acceleration response will be very sensitive to the measurement noise. In this study, the measured strain response is used for moving force identification.

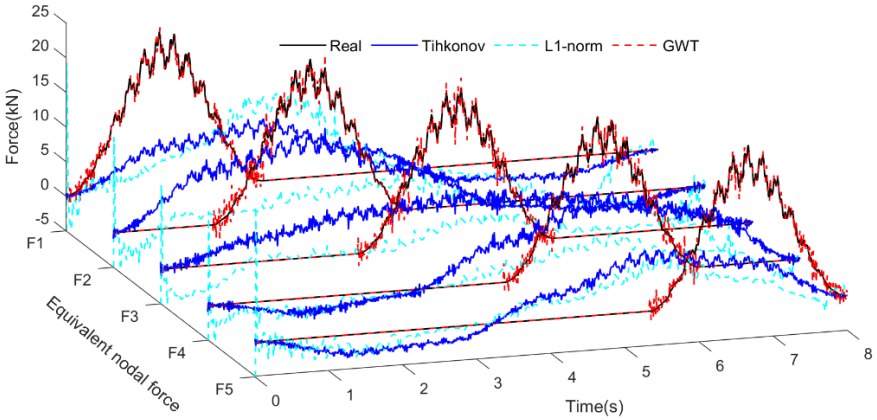

(a) Identified equivalent loads in Case 1

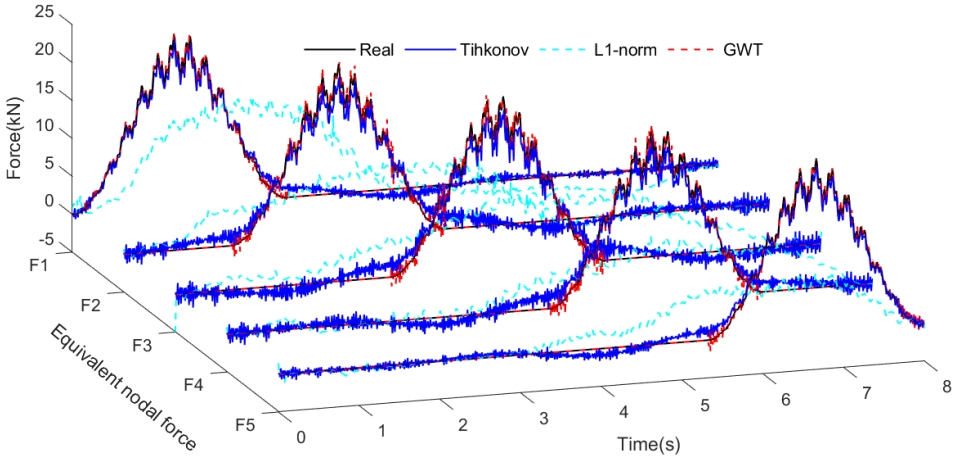

(b) Identified equivalent loads in Case 2

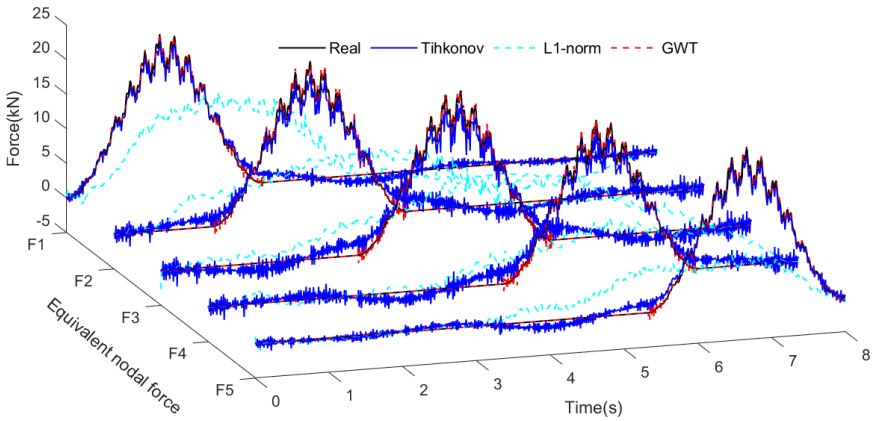

(c) Identified equivalent loads in Case 3

Figure 5.3 Identified equivalent loads

Figure 5.3 shows the equivalent loads estimated by using the measured strain with considering 5% noise level. From Figures 5.3(a) to 5.3(c), there are some obvious differences among the equivalent loads that are identified with considering different numbers of sensors. Figure 5.3(a) shows the case1 equivalent loads identification results using different regularisation methods. In this case, the number of sensors is less than the number of equivalent loads, which makes the inverse problem equation under-determined. From the Figure 5.3(a), it is clear that Tikhonov regularisation method and l_1-norm regularisation method both fail to reconstruct the equivalent loads. Only proposed GWT method could identify the equivalent loads in this case. The accuracy index REs are listed in Table 5.2. The errors by the proposed Group Weighted Tikhonov regularisation (GWT) method are all below 10%. There are large errors by the Tikhonov regularisation method and L1-norm regularisation method. For case2 and case3, the number of sensors is equal or more than the number of equivalent loads. Figure 5.3(b) and Figure 5.3(c) show the case 2 and case3 equivalent loads identification results using different regularisation methods. It is clear that L1-norm regularisation method fails to reconstruct the equivalent loads due to the strong correlation of adjacent column vectors in the transfer matrix, Tikhonov regularisation method could identify the equivalent loads with large errors. The RE values using Tikhonov regularisation method corresponding to these two cases are all greater than 15%. While the RE values using proposed GWT method corresponding to these two cases are less than 8%. These results indicate the number of measured points would affect Tikhonov regularisation method identified results, especially in the case where the number of sensors is less than the number of equivalent loads. However, the number of measured points do not have that much influence on the proposed method identified results. This means that we could use less sensors to identify more equivalent loads to increase the moving force identification accuracy.

Table 5.2 Identification accuracy index RE (%) for each equivalent load

RE	Case1			Case2			Case3		
	Tikhonov	L1-norm	GWT	Tikhonov	L1-norm	GWT	Tikhonov	L1-norm	GWT
RE1	125.98	166.37	7.69	15.15	114.27	3.47	16.53	111.24	4.60
RE2	96.98	111.96	7.59	24.83	98.69	4.96	27.53	99.01	6.40
RE3	127.93	113.85	8.29	28.07	113.68	6.10	31.52	114.02	7.70
RE4	97.21	98.29	7.23	25.39	90.13	4.91	27.87	89.84	6.43
RE5	125.93	123.65	6.61	15.41	91.32	2.88	16.80	90.44	3.86

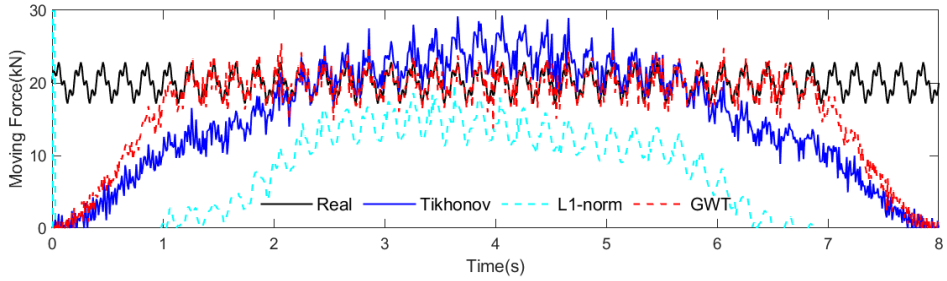

(a) Identified moving force in Case 1

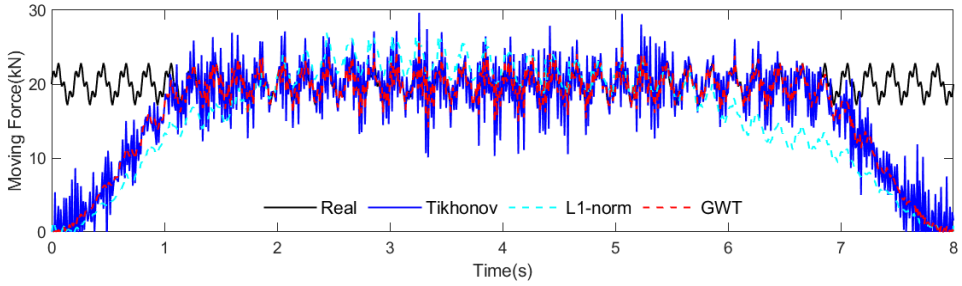

(b) Identified moving force in Case 1

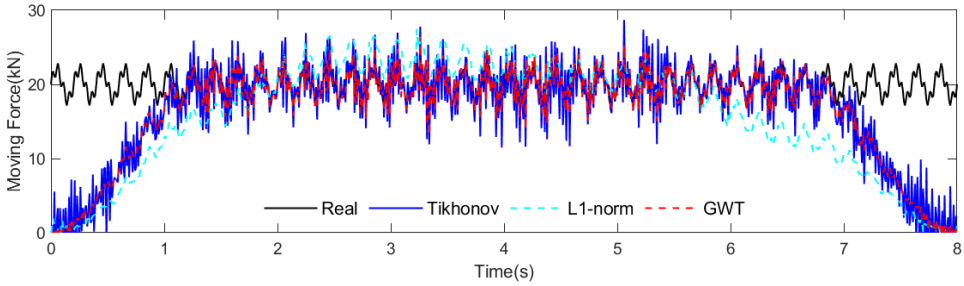

(c) Identified moving force in Case 3

Figure 5.4 Identified moving force

Figures 5.4(a) to 5.4(c) show the identified moving force in case1, case2 and case3 using these three regularisation methods. Since the identified moving force is the sum of the identified equivalent loads. The moving force identification accuracy is consistent with the equivalent loads identification accuracy. From these results, it is clear to see that the moving force at boundary position is not identified well with GRE more than 20%, but the moving force in the middle interval could be reconstructed well using proposed method with MRE less than 6%. This middle part information of the identified moving force could be used for the vehicle weight estimation.

Table 5.3 Identification accuracy index GRE and MRE results under different number of sensors

Case	GRE (%)			MRE (%)		
	Tikhonov	L1-norm	GWT	Tikhonov	L1-norm	GWT
Case1	34.64	74.69	20.16	21.57	70.17	5.09
Case2	24.61	31.65	20.78	12.91	17.82	5.04
Case3	24.77	31.37	19.97	12.73	17.41	3.98

5.4.3 The effect of the number of equivalent nodal force

Five measured points are considered, and their positions are set as L/6, 2L/6, 3L/6, 4L/6, 5L/6, respectively. As listed in Table 5.1, four cases (Case4, Case2, Case5, Case6) with considering different number of equivalent loads are used for analysis. 5% noise level is considered. The identification accuracy index GRE and MRE values are listed in Table 5.5. Since the Tikhonov regularisation method and l_1-norm regularisation method do not perform well for moving force reconstruction. Figures 5.5 and 5.6 only show the identified results using proposed GWT method.

From Table 5.4, GRE values reflect the identified moving force global accuracy decreasing with the number of equivalent loads increasing. Since the moving force in the boundary position interval will be decreased with the number of equivalent loads increasing. However,

for the Tikhonov regularisation method and l_1-norm regularisation method, this phenomenon only occurs in Case2 and Case4 where the number of measured points are more than the number of equivalent loads. GRE values increase from Case5 to Case6 using Tikhonov regularisation method and l_1-norm regularisation method. Similar circumstance for the identification accuracy index MRE. While for the proposed method, MRE values do not have fluctuation with the equivalent loads number increasing. This means that the middle part of proposed method identified moving force is stable and accurate. To have a better global moving force identification accuracy, the number of equivalent loads could be increased.

Table 5.4 Identification accuracy index GRE and MRE results under different number of equivalent loads

Case	GRE (%)			MRE (%)		
	Tikhonov	L1-norm	GWT	Tikhonov	L1-norm	GWT
Case4	30.03	34.00	28.08	11.01	12.08	5.07
Case2	25.41	31.72	21.11	13.00	17.89	5.48
Case5	24.40	31.81	17.03	15.20	22.01	5.73
Case6	25.04	33.33	14.60	17.57	25.89	5.43

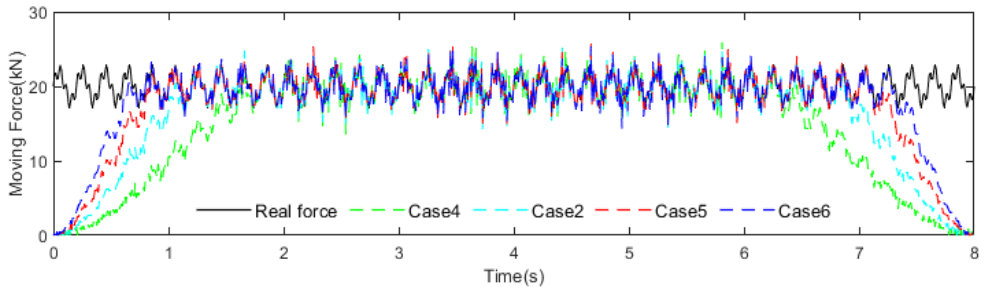

Figure 5.5 Identified moving force under different number of equivalent loads

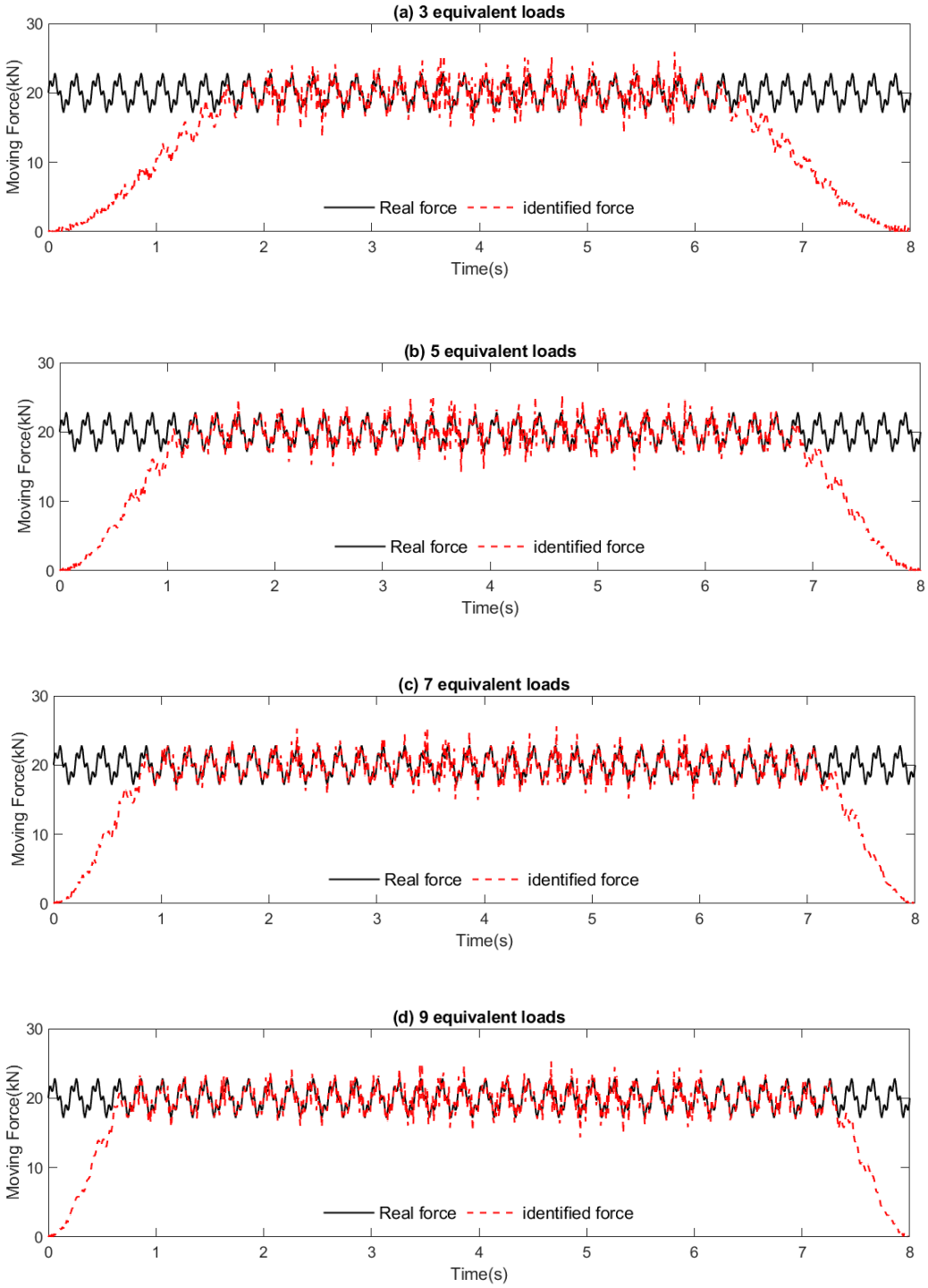

Figure 5.6 Identified moving force via different number of equivalent loads: (a) 3 equivalent loads; (b) 5 equivalent loads; (c) 7 equivalent loads; (d) 9 equivalent loads.

5.5 Summary

In this chapter, one group weighted sparse regularisation method is proposed for moving force identification via equivalent nodal forces. The moving force could be transferred into equivalent nodal forces, which have the group sparse feature. Its effectiveness and applicability are studied numerically on a simply supported beam in comparison with the standard sparse regularisation method and the classical Tikhonov regularisation method. The following points can be concluded.

1) The proposed GWT method is effective and accurate to identify the equivalent node forces even with limited sensors. The moving force can also be reconstructed by identified equivalent node forces with acceptable accuracy.
2) There are large errors in the identifed results of the moving force close to the supports and the identified results around the middle of the beam agree well with the true values.
3) The accuracy of the moving force identification is increased with the number of equivalent node forces.

Chapter 6 Interface monitoring in steel-concrete composite beams with a novel slip sensor

6.1 Overview

In this chapter, a new interface slippage monitoring system based on Ultra-flat Industrial Potentiometer Membrane (UIPM) sensor has been developed to measure directly the relative displacement between concrete slab and steel girder and assess the integrity of the shear connectors. The design, working principle and calibration of the slip sensor are summarised, then experimental studies have been conducted to demonstrate the sensitivity and performance of the developed slip sensor in condition monitoring of shear connectors in composite bridges. In this project, finite element models are established and validated based on experimental results. Subsequently, parametric studies are conducted to investigate the influence of different damage severities and locations on interface slippage between steel girder and concrete slab by changing the static loading position.

6.2 Experimental study

6.2.1 Interface monitoring system

Relative slip exists in steel-concrete composite beam due to the difference in longitudinal deformation between the steel beam and the concrete at the interface during bending. This kind of interface slip will make a difference on the bearing capacity, deformation, stiffness and seismic performance of composite beams. So accurately measuring the relative slip displacement during test is important. For this aim, Ultra-flat Industrial Potentiometer Membrane slip sensor is used in our tests. The detail dimensions could be found in Sadeghi et al. (2021).

6.2.1.1 Detailed design of the slip sensor system

The slip sensor is a potentiometric linear displacement sensor including active area, flat flex cable and connector berg three parts. Detailed information for this type sensor is shown in Figure 6.1.

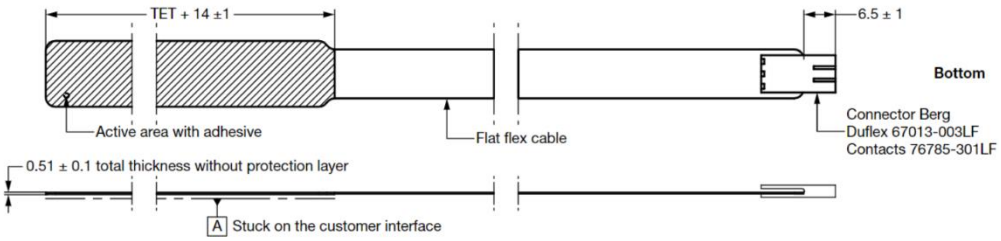

Figure 6.1 UIPM slip displacement sensor

The active area of the sensor consists of resistive and collector tracks separated by a spacer as shown in Figure 6.2. In the active area, ultra-flat potentiometer membrane is used to convert a mechanical position into an electrical signal through the contact between the collector track and resistive track. We can obtain the exact position of the wiper by the voltage value because the voltage varies depending on the position of the presser on the deformable membrane.

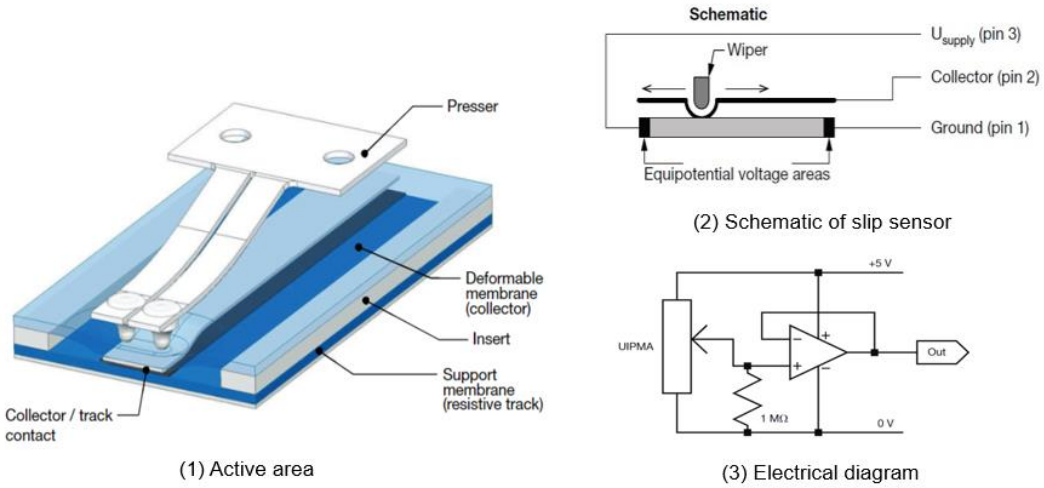

Figure 6.2 Schematic of slip sensor

In the operating condition, this sensor will deliver a linear voltage between 0 V and the supply voltage as a function of the position of the wiper on the track. From the electrical diagram

shown in Figure 6.2, it can be concluded that the voltage obtained from collector and the wiper slip displacement x are linear. Since the resolution of this sensor is infinite, it is important to have an accurate sensitivity. According to the relationship between voltage and displacement, we can obtain

$$y(x) = Rx + e(x) \tag{6.1}$$

where $y(x)$, is the output of slip sensor, R is the sensitivity, $e(x)$ is the error, and x is the measured relative displacement from calibration.

6.2.1.2 Sensor Calibration

The sensor calibration refers to the process of establishing the relationship between sensor output and input through experiments and determining the error under different conditions of use. In this section, the sensitivity and linearity are tested in the process of displacement-voltage (x−u) calibration. Moreover, the calibration apparatus is shown in Figure 6.3, where a high-precision linear translation stage (universal testing machine (UTM)) is employed for producing absolute displacement with the repeatability of 0.1μm, and a voltage acquisition module is employed to measure the sensor output voltage with the absolute accuracy of 2 mV. Two L-shape steel plates have been fabricated, and they are installed on the top and bottom part of UTM. The sensor film is stick on the bottom plate, and the 3D-printed wiper mounted on the top part is used as the contact point moving along the sensor film. The pin of the wiper is flexible in the up and bottom direction as connected by a spring. The recording data are in voltage obtained from UTM and measured data from slip sensor which are collected and interpreted in LabVIEW software.

In the experiments, the displacement variation interval is 0.1 mm during the range of 0–2 mm, and the corresponding output voltages are collected at the same time. In this thesis, all slip sensors are tested in order to avoid individual contingency. The calibration is conducted using the testing machine as shown in Figure 6.3. The relative displacement between two parts is

monitored using the slip sensor. Consequently, the slip sensor 1 calibration data is shown in Figure 6.4. The calibration results demonstrate that the sensors are very sensitive to the slip. The slope, that is the coefficient R, can be used to convert measured voltage from the sensor as relative displacement when installed on a structure. Most points are fitted well with a clear linear relationship as shown in Figure 6.5.

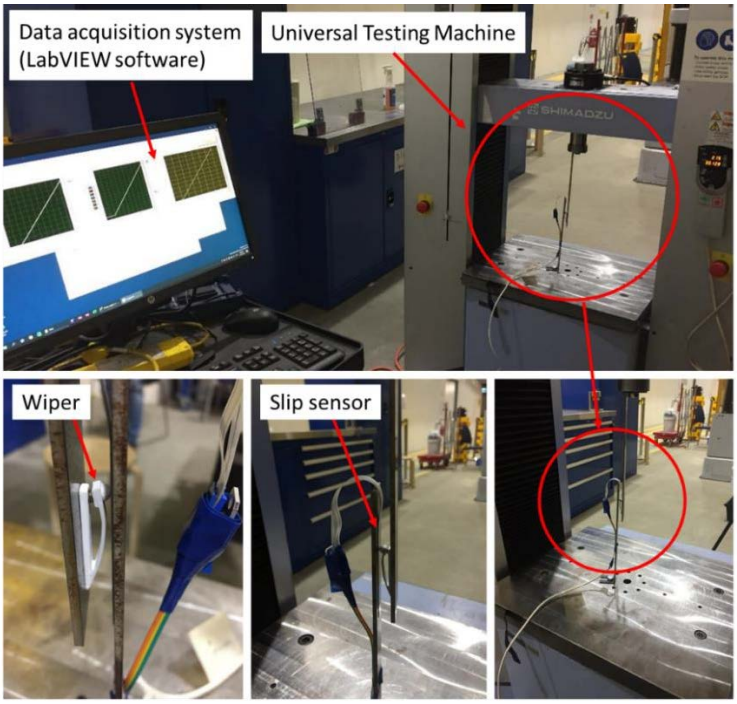

Figure 6.3 Calibration apparatus

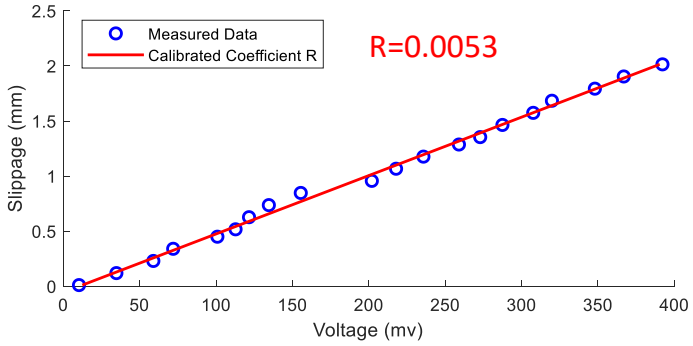

Figure 6.4 Sensor no. 1 calibration between relative displacement (slip) and voltage

6.2.2 Experiment setup

The bridge model is a three-span simply supported steel-concrete composite beam bridge (10000mm long, 1000mm wide and 300mm thick). The bottom of main beam for the bridge model include four short I beams with length 1982mm and two long I beams with length 6000mm, These I beams has the same section. The concrete slab is on the top with thickness 100mm and width 1000mm. Concrete grade 40 was used to construct slabs and connected to the steel girders by shear connectors marked as SC32. Test is studied on the middle beam shown in Figure 6.5. Two types of connections were made in this model: headed studs and removable bolts. For the two side main beam headed stud is welded to its flange and standard-type headed studs with nominal shank diameters of 19mm is used. For the middle main beam, removable bolts (M16) are used as the shear connectors to simulate the bridge damage and the length embedded into concrete slab is 70mm. Due to the availability of slip sensors, seven calibrated slip sensors are installed equally from S1 to S7 along the half of one girder. Alignment of slip sensors is shown in Figure 6.5.

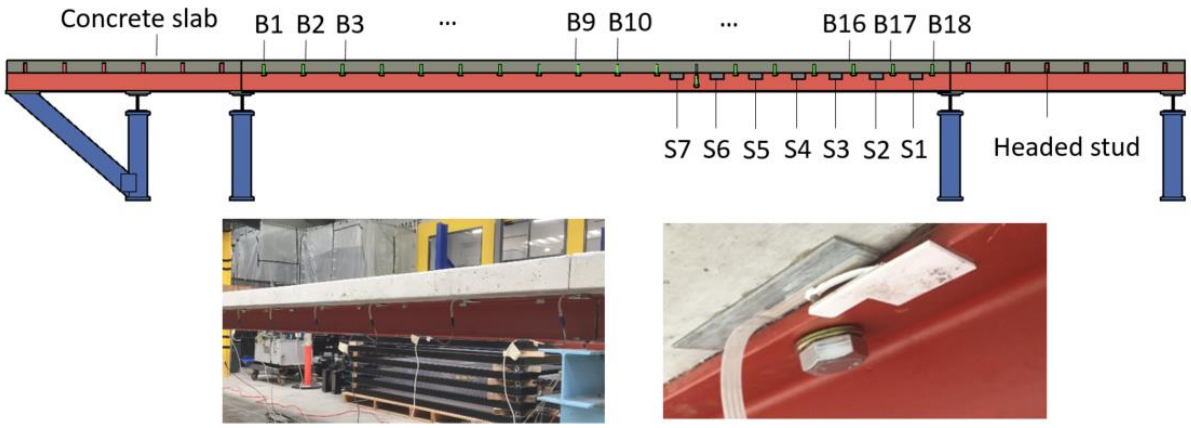

Figure 6.5 Experimental bridge model

6.2.3 Experimental procedure

To investigate the sensitivity of slip sensors to inherent interlayer slip in composite beam and verify the finite element model built in next section, three main levels of load increments, including 375, 750, and 1100kg, are considered for tests. At the first stage, the composite bridge

without damage is considered for testing to study the inherent interlayer slip under loading. The time-domain data obtained from the slip-sensors were collected through 7-channels in the National Instrument data acquisition system using LabVIEW software.

6.2.4 Test results and discussion

The performance of the slip sensors for inherent interlayer slip when there is no damage on the shear connectors is studied. Loads are applied on the mid-span of the bridge in three main increments. Figure 6.6 shows the bridge subjected to loads by concrete blocks placed on the mid-span. The first load was applied by putting six concrete blocks (The dimension and weight of each concrete block are 300×300×300mm and 62.5kg, respectively) on the bridge deck with an overall weight of 375kg. In the second load increment, six more similar concrete blocks were added to increase the overall load to 750kg. In the last increment, a 350kg concrete block (550×550×550mm) was added to reach the maximum load. The considered loads are much less than the load-bearing capacity of the bridge. The reason is to explore the sensitivity of the slip sensor to tiny slides of composite layers, which can be due to damage in a shear connector. Traditional methods may not monitor this small damage. Besides, extreme loads are not practical in SHM tests as it may lead to large damage or failure in the structure.

(1) (2) (3)

Figure 6.6 Bridge subjected to loads: (1) first load 375kg, (2) second load 740kg and (3) third load 1100kg

Figure 6.7 shows the interlayer slip (relative displacement between the layers) of composite beam under loads collected from seven sensors. The sensors are labelled with numbers 1 to 7 from the support to the mid-span (right to left-hand-side). The interlayer slips are expected to start from zero at the mid-span to a maximum value at the supports. At the first load increments, this expectation was not achieved as the quantity of load is small. However, the sensors near support recorded the maximum interlayer slip by increasing load. The trend of the graph for sensor number 1 is smooth until the end of the second increment. But after that, a noticeable increase occurs by increasing the load, demonstrating that when the mid-span deflection increase, the slip will also raise with the maximum values in the boundary condition.

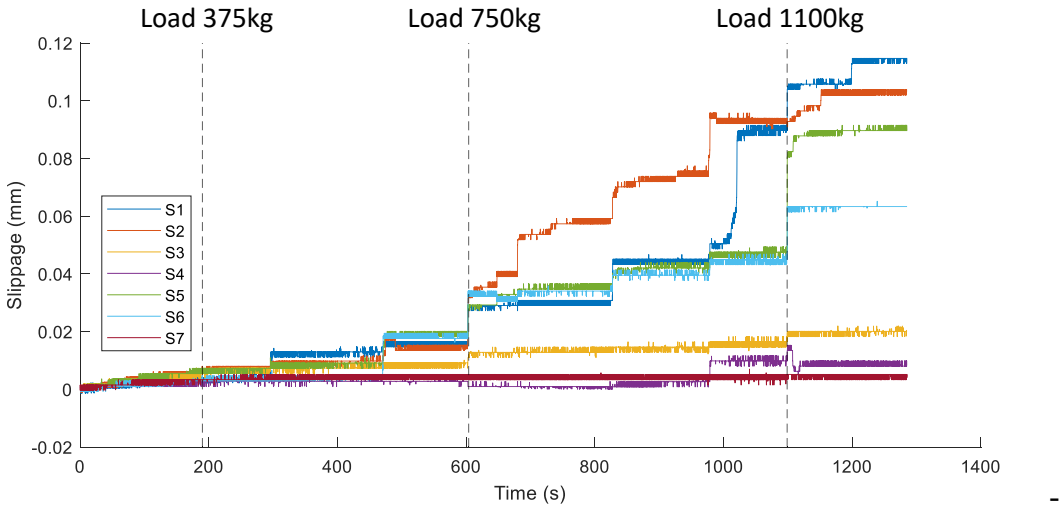

Figure 6.7: The interlayer slip of composite beam without damage under loading

6.3 Finite element model

6.3.1 General

Finite element (FE) model analysis was carried out using ANSYS. The convergence study has been carried out to determine the mesh. All components including concrete slab, shear connectors, steel beam were properly modelled, as shown in Figure 6.8. In the finite element model, the shell element with four nodes (Shell 63) was used for simulating the concrete slab and the steel girders. Since the steel girder and concrete slab are connected via bolts as shear

connectors, which are used to transmit the longitudinal shear force between the steel girder and concrete slab, A non-linear spring element (Combin39) was employed to model the shear connector characteristic. The positions of the spring elements coincide with the positions of the shear connectors used in the composite beam. The elastic Young's modulus of 205 GPa and Poisson's ratio of 0.3 are defined for steel girder. The elastic Young's modulus of 30 GPa and Poisson's ratio of 0.3 are defined for Concrete slab. The load-slip characteristics of the shear connector are obtained from the corresponding FE-models of push-off test. The bottom of the steel girder both ends are restricted to move in the X, Y, Z directions as shown in Figure 6.8 for simulating the real boundary conditions, and the effect of frictional contact between steel girders and concrete slab is ignored in this model.

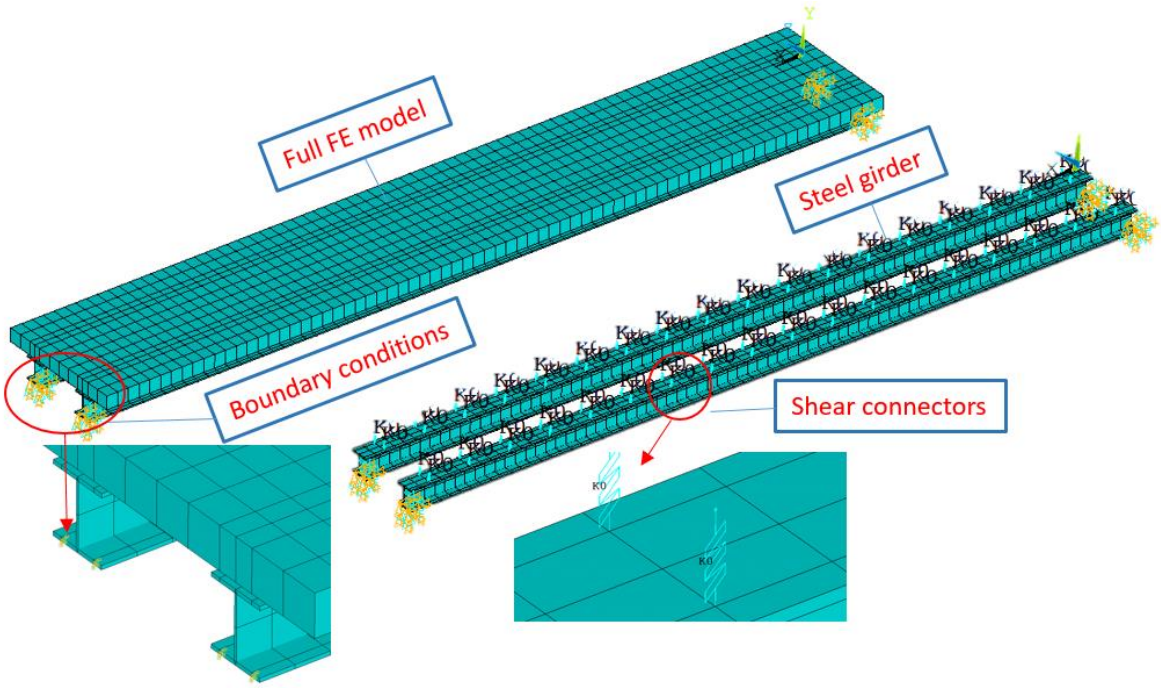

Figure 6.8. Finite element model

6.3.2 FE model Validation

The interface slippage obtained from the FE model are compared with the corresponding experimental results in Figure 6.9. The comparison results show the agreement between finite element results and test results. The slippage measured by slip sensor NO.3 and slip sensor

NO.4 always has a big weird deviation with the finite element results, and this situation does not fit the slippage change trend calculated by theory, in which the interlayer slips are expected to start from zero at the mid-span to a maximum value at the supports. So we assume these two measurement points as bad points. The results of other measurement points tend to be consistent with the simulation results with small discrepancy. Therefore, it can be concluded from these comparisons that the finite element model developed is capable to do the next parametric study.

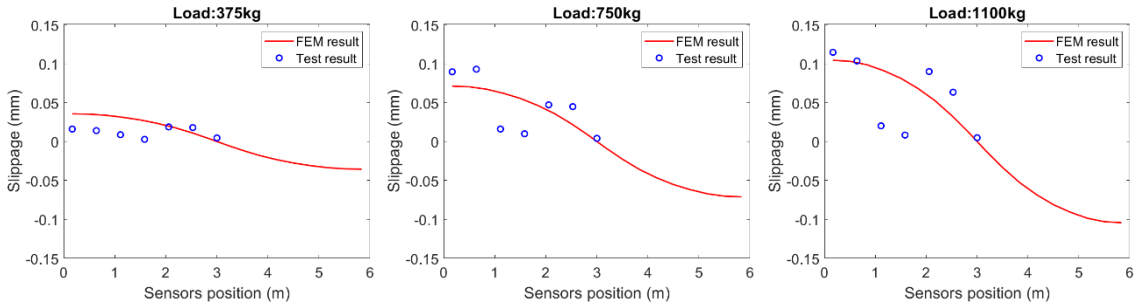

(1) (2) (3)

Figure 6.9 Interlayer slippage from finite element and experimental results (1) Load:375kg; (2) Load:750kg; (3) Load:1100kg

6.4 Numerical study

In the section, parametric studies are conducted to investigate the influence of different damage severities and locations on interface slippage between steel girder and concrete slab by changing the static loading position. Since there is still some limitations using experimental test to do the parametric study, and it is demonstrated in the above Section that the FE modeling approach can accurately describe the bolt shear capacity and interface slippage, parametric studies are conducted on the FE model. According to the comparison results between experimental test slippage and FE model slippage, 1100kg employed could obtain the better agreement. So in following cases 11kN is conducted from left end of the beam and move to right end with 18 load positions. The load positions are marked from left to right from 1 to 18

corresponding with B1 to B18. Meanwhile, these positions are also used as measurement points to obtain the interface slippage between concrete slab and steel girder. Measurement point is also marked from left to right from 1 to 18.

6.4.1 Influence of damage severities

In this investigation, there are 4 cases including undamaged state (Case0), B4 bolts removed state (Case1), B4, B5 bolts removed state (Case2), B3, B4, B5 bolts removed state (Case3). These cases are used to study the influence of different damage severities on interface slippage.

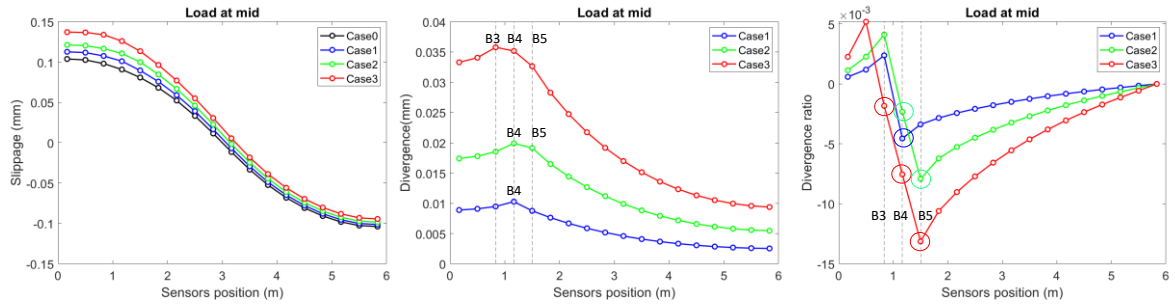

(1) (2) (3)

Figure 6.10 Results comparison in Case0, Case1,Case2 and Case3: (1) Slippage comparison (2) Slippage divergence comparison (3) Divergence ratio comparison

When the static load is applied on the mid of the beam, all measurement points are used to study the influence of different damage scenarios on interlayer slippage. The results obtained from Case0, Case1, Case2 and Case3 are presented in Figure 6.10. It can be seen in Figure 6.10(1) that the slippage increases as damage severity increase and in Figure 6.10(2) the biggest slippage divergence in these three damage scenarios always occurs at the far left removed bolts point. But it is not able to identify all removed bolts positions using the slippage and slippage divergence. So the divergence ratio in these three damage scenarios is calculated for further analysis. As can be seen from Figure 6.10(3), great changes of divergence ratio have taken place at the removed bolts positions, and the number and position of abnormal value are

corresponding to the removed bolts in Case1 (B4), Case2 (B4, B5) and Case3 (B3, B4, B5). This parameter could be regarded as a good indicator for detecting the damage scenarios. Through changing the static load position, the slippage measured at position 4, position 9 and position 12 and influenced by different damage scenarios is studied. Position 4, position 9 and position 12 represent left part, middle part and right part of the beam respectively. In these cases, 11kN is conducted from left end of the beam and move to the right end with 18 load positions. Since damage simulated in Case1, Case2 and Case3 is at the left part of the beam, the slippage measured at position 4 shown in Figure 6.11(1) increases as the damage severity increases. While the absolute value of slippage measured at position 12 shown in Figure 6.11(3) decreases as the damage severity increases. This trend at position 12 is opposite to position 4. The comparison result indicates that the damage on the left will increase the left part slippage of the beam and reduce the right part slippage, and this corresponding effect will increase as the damage severity increases. The middle measurement point 9 shows that the direction of slippage near the mid beam changes when the load moves from left part to right part. When the load is conducted at left part, the absolute value of slippage measured at position 9 decreases as the damage severity increases. While when the load moves to the right part, the trend becomes opposite.

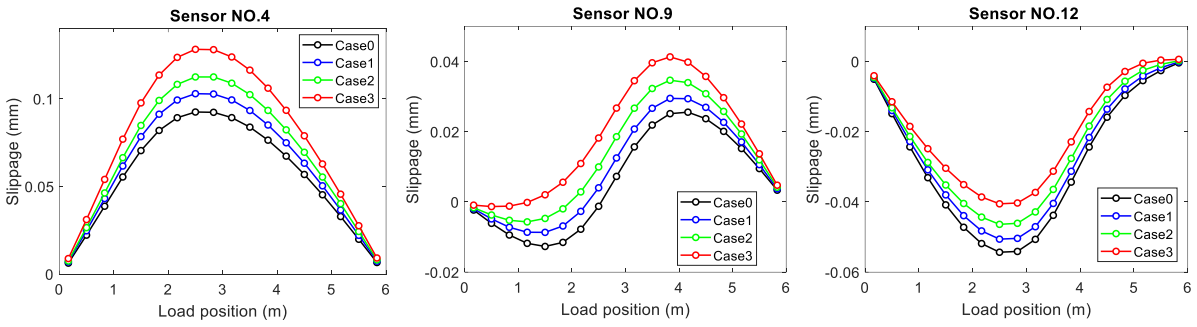

(1) (2) (3)

Figure 6.11 Slippage comparison in Case0, Case1,Case2 and Case3: (1) Slippage measured at position 4; (2) Slippage measured at position 9; (3) Slippage measured at position 12

The slippage divergence that is the difference between two adjacent slippages is also calculated for further analysis shown in Figure 6.12. Comparing among Figure 6.12(1), Figure 6.12(2) and Figure 6.12(3), the divergence value decreases from left to right, which shows that right measurement points have less sensitivity to the left damage scenarios. It can be seen that the divergence value increases with the increasing of damage severity. This parameter could be used to detect damage severities, but not able to identify the damage location.

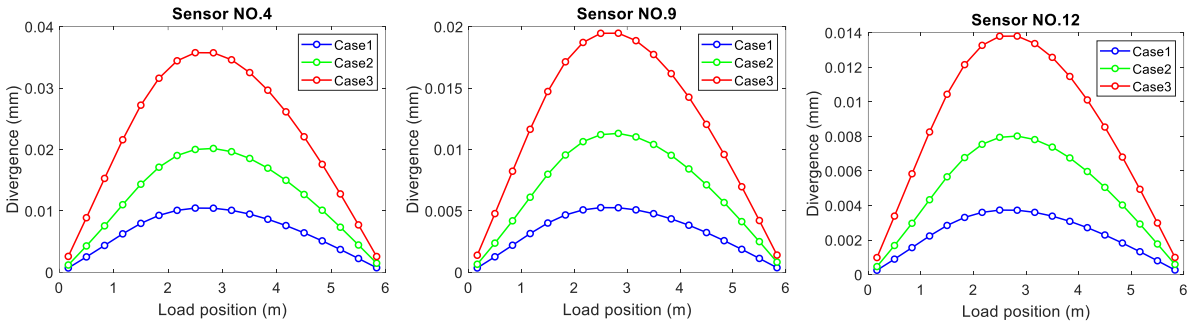

(1) (2) (3)

Figure 6.12 Slippage divergence comparison in Case1, Case2 and Case3: (1) Divergence at position 4; (2) Divergence at position 9; (3) Divergence at position 12

6.4.2 Influence of multiple damage severities and multiple damage locations

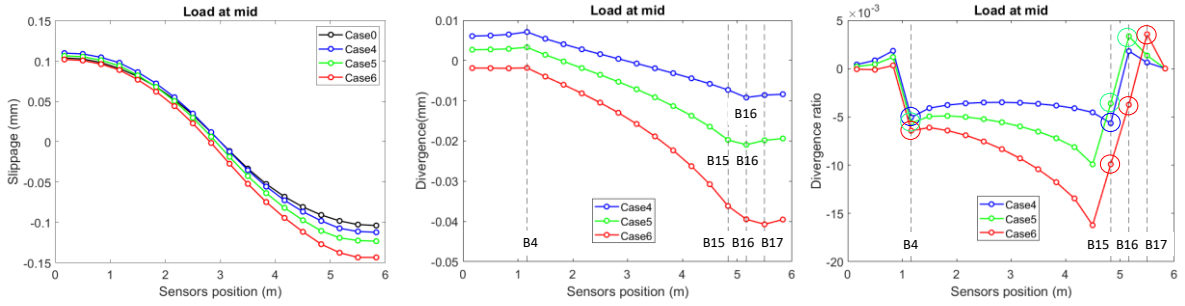

(1) (2) (3)

Figure 6.13 Results comparison in Case0, Case4, Case5 and Case6: (1) Slippage comparison (2) Slippage divergence comparison (3) Divergence ratio comparison

In this investigation, Case4 (B4, B16 bolts removed), Case5 (B4, B15, B16 bolts removed) and Case6 (B4, B15, B16, B17 bolts removed) are simulated using the finite element model, to study the influence of multiple damage severities and multiple damage locations on interface slippage.

When the static load is applied on the mid of the beam, all measurement points are used to study the influence of different damage scenarios on interlayer slippage. The results obtained from Case0, Case4, Case5 and Case6 are presented in Figure 6.13. It can be seen in Figure 6.13(1) that the absolute value of slippage increases as damage severity increase and in Figure 6.10(2) the absolute value of slippage divergence in Case 4, Case5 and Case6 has the similar trend with divergence in Case1, Case2 and Case3. Left slippage divergence at damage position is affected by the right damage scenarios and decreases with the right damage severity increase. It can be seen from Figure 6.10(3) that great changes of divergence ratio have taken place at the removed bolts positions, and the number and position of abnormal value are corresponding to the removed bolts in Case4 (B4, B16), Case5 (B4, B15, B16) and Case6 (B4, B15, B16, B17). This parameter could also be regarded as a good indicator for detecting multiple damage scenarios.

Slippage measured at position 4, position 9 and position 12 under different load positions is studied. As is shown in Figure 6.11, the slippage measured at position 4, position 9 and position 12 in Case 4, Case5 and Case6 has the opposite trend with slippage in Case1, Case2 and Case3 because of the different damage locations. The absolute value of slippage measured at position 4 shown in Figure 6.14(2) decreases as the damage severity increases. While the absolute value of slippage measured at position 12 shown in Figure 6.14(3) increases as the damage severity increases. The comparison result also indicates that the damage on the right will increase the right part slippage of the beam and reduce the left part slippage, and this corresponding effect will increase as the damage severity increases. This situation will increase the difficulty of

detecting multiple damages. The slippage divergence is also calculated for further analysis shown in Figure 6.15. It can be seen that the absolute value of divergence increases with the increasing of damage severity at measurement position 9 and 12. The divergence of measurement point 4 in these three cases shows that this parameter could not be used to detect multiple damage severities and identify the damage locations.

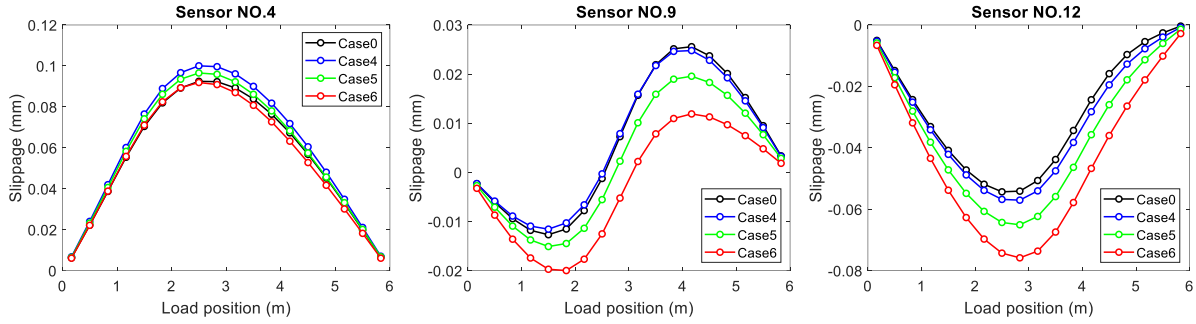

(1) (2) (3)

Figure 6.14 Slippage comparison in Case0, Case4, Case5 and Case6: (1) Slippage measured at position 4; (2) Slippage measured at position 9; (3) Slippage measured at position 12

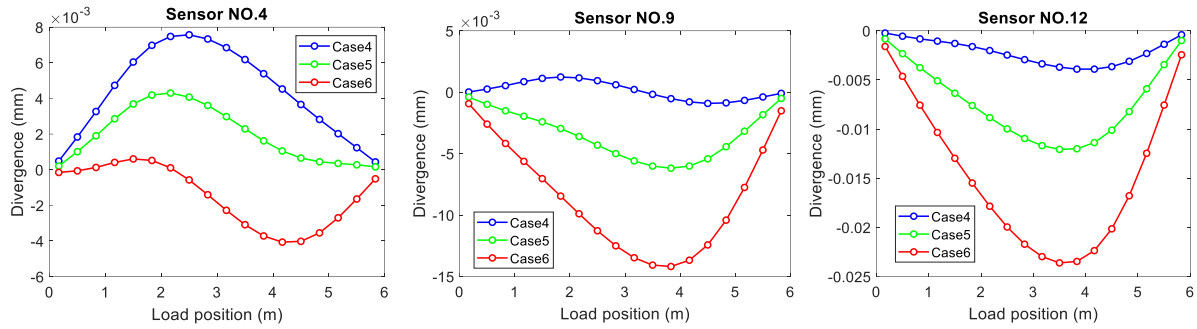

(1) (2) (3)

Figure 6.15 Slippage divergence comparison in Case4, Case5 and Case6: (1) Divergence at position 4; (2) Divergence at position 9; (3) Divergence at position 12

6.4.3 Influence of damage locations with one damage severity

In this investigation, Case7 (B2 bolts removed), Case1 (B4 bolts removed), Case8 (B6 bolts removed) and Case9 (B8 bolts removed) are simulated using the finite element model, to study the influence of damage locations on interface slippage.

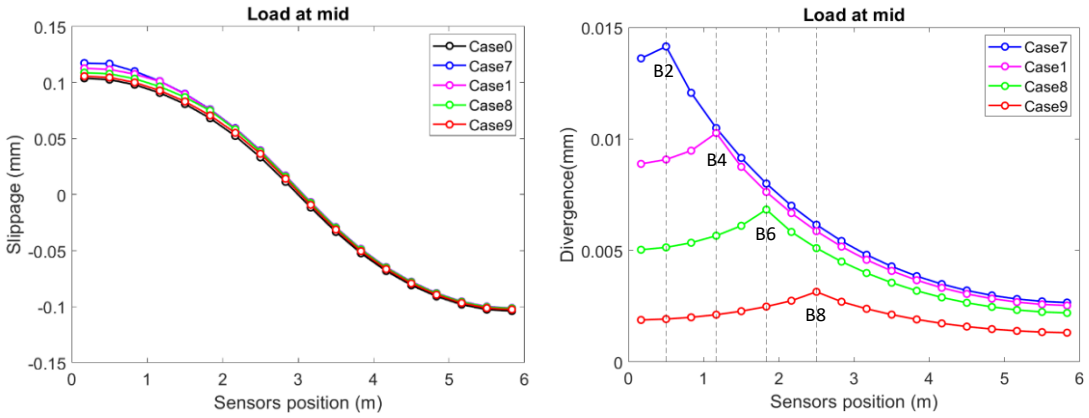

(1) (2)

Figure 6.16 Results comparison in Case0, Case7,Case1,Case8 and Case9: (1) Slippage comparison (2) Slippage divergence comparison

When the static load is applied on the mid of the beam, all measurement points are used to study the influence of different damage scenarios on interlayer slippage. The results obtained from Case0, Case7, Case1, Case8 and Case9 are presented in Figure 6.16. It can be seen in Figure 6.16(1) that the absolute value of slippage increases as damage location moves from left to right and in Figure 6.16(2) the slippage divergence in Case7, Case1, Case8 and Case9 shows a good trend, decreasing with the removed bolts from left to right. The biggest slippage divergence in these four damage scenarios always occurs at the removed bolts point. This shows that the damage near the support will have a greater impact on the interface slippage between concrete slab and steel girder.

6.5 Summary

This paper first carried out experimental test to study the sensitivity of the slip sensors we developed. 375kg, 750kg and 1100kg three load conditions were carried out, and the accuracy

of FE model was verified. Then extensive parametric studies are conducted to investigate the influence of different damage severities and locations on interface slippage between steel girder and concrete slab by changing the static loading position. From the experimental and numerical results, the following conclusions can be drawn:

(1) The slip sensor sensitivity and useability in monitoring the interface slippage between concrete slab and steel girder is investigated. An accurate calibration technique is carried out utilizing the testing machine and the deviation taken into account in data acquisition system programming. The calibration results demonstrate that the sensors are very sensitive to the slip. Experimental results under 750kg load and 1100kg load demonstrate that the slip sensors have a good performance for interface slippage measurement except the slip sensor NO.3 and slip sensor NO.4. The applied load 375kg is not large enough to overcome the friction force between the girders and slab.

(2) Interface slippage between concrete slab and steel girder increases with the increasing of damage severity. Damage scenario near the support position has a greater impact on the slippage. In multiple damage scenario conditions, the damage simulated at different locations will increase or weaken the corresponding position slippage. Slippage divergence ratio is very sensitive to the damage severities and damage locations, which could be regarded as a good indicator to detect the interface damage scenarios.

(3) The damage scenario could not be identified at a specific measurement point via moving the static load position from left end to right end. As for damage scenarios detection at left and right part of the beam, the optimal choice of load position is in the middle of the span. And the quarter of the beam is regarded as the optimal position for middle part interface damage scenarios detection.

Chapter 7 Cable damage detection of a bridge under traffic loading from bridge deck strain measurements using SVM based classification and regression

7.1 Overview

This Chapter develops a novel method to estimate the cable state using the bending strain changes when the vehicle travelling on the bridge deck. Firstly, the analytical formulations between the damaged cable force and the bridge deck bending strains are established in this paper. Then this identification method is introduced in two steps. The first step is to find the damage cable, which is considered as a multiple classification issue, and Support Vector Classification (SVC) is used to train the Damage Cable Identifier (DCI) to detect the damage cable. The second step is to identify the damage degree of the damage cable, which is considered as a nonlinear regression issue, and Support Vector Regression (SVR) is utilized to train the Damage Degree Identifier (DDI) to quantify the cable damage. At last, this method is applied in a real cable-stayed bridge to verify its feasibility and effectiveness.

7.2 Damage identification approach

7.2.1 The cable-stayed bridge

The cable-stayed bridge is one type of long-span bridges. A number of cable-stayed bridges have been constructed globally since the first modern cable-stayed bridge was completed in 1956 in Sweden because of their rigid stiffness, good aerodynamics, good seismic resistance, and desired esthetics. There has been many cable-stayed bridges constructed with centre-spans of over 1000 m, such as, the Sutong Bridge in Jiangsu, China (1088 m), the Stonecutters Bridge

in Hong Kong, China (1018 m), and Russky Island Bridge in Russia (1104 m). Since cable-stayed bridges suffer from various long-term loads (such as dead load, vehicle loads), environmental actions, and natural disasters. Up to 2010, cables in 56 bridges have been replaced in China. The average lifespan of cables is 11.8 years for these 56 bridges, which is much shorter than the design objective and the lifespan of the bridges (Li and Ou 2016).

(a) An illustration of the bridge (b) The beam array

Figure 7.1 The real cable-stayed bridge

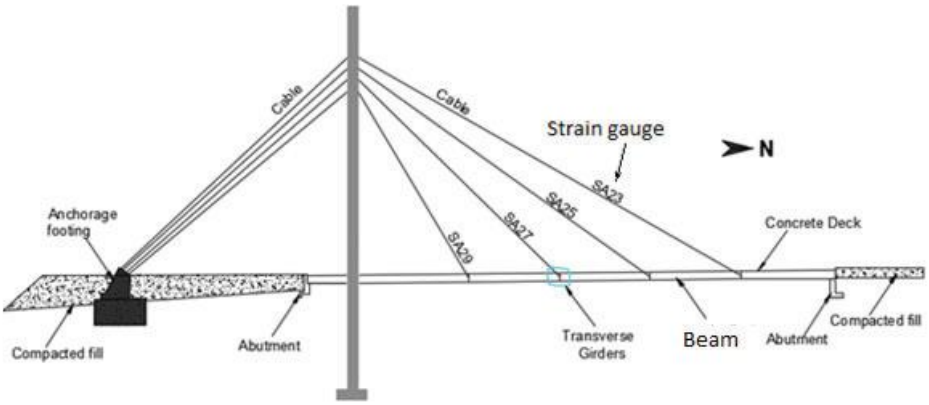

Figure 7.2 Schematic view of the cable-stayed bridge

In this chapter, a real cable-stayed bridge over the Great Western Highway in the state of New South Wales, Australia (33°45′50.49″S, 150°44′31.14″E) was considered as a case study to test and validate the proposed method. Figure 7.1(a) shows an illustration of the bridge (Alamdari

et al. 2019; Kalhori, Makki Alamdari, et al. 2018; Sun et al. 2017). The cable-stayed bridge has a single A-shaped steel tower with a composite steel-concrete deck. The bridge is composed of 16 stay cables with a semi-fan arrangement. The bridge span and the tower height are 46 and 33 m, respectively. This bridge provides a connection between two Western Sydney University campuses over the Great Western highway and carries one traffic lane and one sidewalk. The deck has a thickness of 0.16 m and a width of 6.3 m, and it is supported by four I-beam steel decks. These decks are internally attached by a set of equally spaced floor beams, as depicted in Figure 7.1(b). The assigned numbers of the cables and the decks are shown in Figure 7.2.

7.2.2 The relationship between the cable force and the bending strains of the bridge deck

In establishing the damage identification approach, formulations involve the effect of individual cable forces on the bending strain of the bridge deck. Based on the aforementioned real cable-stayed bridge in the state of New South Wales, a simple plane calculation diagram shown in Figure 7.3(a) is employed for deriving the equations between the cable forces and the bridge deck bending strains. In practice, the cable forces change with the vehicle location x when traveling on the bridge. To simplify the model, the cables can be removed and replaced by concentrated forces, as shown in Figure 7.3(b). A roller support is used to represent the pylon to simplify the bridge as a continuous beam with two spans. Then using Finite Element Method (FEM), the continuous beam is divided into 6 elements with 7 nodes shown in Figure 7.3(b). The final calculation diagram is shown in Figure 7.3(c) with horizontal and vertical components of cable forces $F_{i\mathrm{h}}$ and $F_{i\mathrm{v}}$ as follows,

$$F_{i\mathrm{v}} = F_i \sin\theta_i \quad F_{i\mathrm{h}} = F_i \cos\theta_i \tag{7.1}$$

where, θ_i is the angle between the deck and the ith cable.

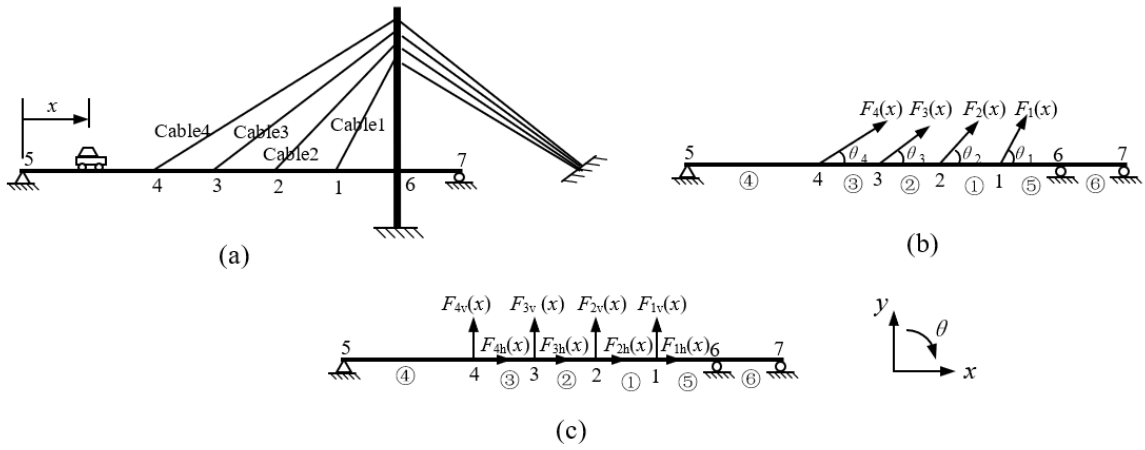

Figure 7.3 The cable-stayed bridge calculation diagram

The equilibrium equation can be obtained as follows:

$$F(x) = K \cdot \Delta \tag{7.2}$$

where, F is the load vector,

$$F(x) = (F_{1\mathrm{h}}(x) \quad F_{1\mathrm{v}}(x) \quad 0 \quad F_{2\mathrm{h}}(x) \quad F_{2\mathrm{v}}(x) \quad 0 \quad F_{3\mathrm{h}}(x) \quad F_{3\mathrm{v}}(x) \quad 0 \quad F_{4\mathrm{h}}(x) \quad F_{4\mathrm{v}}(x) \quad 0 \quad \cdots$$
$$\ldots \quad 0 \quad 0 \quad 0 \quad 0 \quad 0)^{\mathrm{T}}_{1\times 17} \tag{7.3}$$

where v is the vertical direction of load, h is the horizontal direction of load.

K is the beam stiffness matrix that has considered the boundary conditions,

$$K = \begin{bmatrix} k_{1,1} & \cdots & k_{1,17} \\ \vdots & \ddots & \vdots \\ k_{17,1} & \cdots & k_{17,17} \end{bmatrix} \tag{7.4}$$

where, $k_{i,j}$ is the stiffness coefficient, which means the ith load when the jth displacement equal to 1 and other displacements are all equal to 0. Δ is the nodes displacements vector,

$$\Delta(x) = (u_1(x) \quad v_1(x) \quad \varphi_1(x) \quad u_2(x) \quad v_2(x) \quad \varphi_2(x) \quad u_3(x) \quad v_3(x) \quad \varphi_3(x) \quad \cdots$$
$$\cdots \quad u_4(x) \quad v_4(x) \quad \varphi_4(x) \quad \varphi_5(x) \quad u_6(x) \quad \varphi_6(x) \quad u_7(x) \quad \varphi_7(x))^{\mathrm{T}}_{1\times 17} \tag{7.5}$$

where, u_i is the ith node horizontal displacement, v_i is the ith node vertical displacement, φ_i is the ith node rotation displacement.

From Eq. (7.2), Δ can be obtained as

$$\Delta(x) = K^{-1} \cdot F(x) \tag{7.6}$$

where, K^{-1} is the inverse matrix of K as follows

$$K^{-1} = \begin{bmatrix} s_{1,1} & \cdots & s_{1,17} \\ \vdots & \ddots & \vdots \\ s_{17,1} & \cdots & s_{17,17} \end{bmatrix} \tag{7.7}$$

After obtaining the displacement of all nodes, each node's moment and bending strain can be obtained by analyzing the element. Here, element ⓔ is taken as an example to calculate the bending strain. The both ends force vector of element ⓔ can be represented as

$$\bar{F}(x)^{ⓔ} = \bar{K}^{ⓔ} \cdot \delta(x)^{ⓔ} \tag{7.8}$$

where,

$$\bar{F}(x)^{ⓔ} = \begin{pmatrix} F_{Ni}(x) & F_{si}(x) & M_i(x) & F_{Nj}(x) & F_{sj}(x) & M_j(x) \end{pmatrix}^{T}$$

(7.9)

where, F_{Ni}, F_{Nj}, F_{si}, F_{sj} and M_i, M_j are the axial forces, shearing forces and bending moments of node *i* and node *j* on element ⓔ, respectively.

The stiffness matrix of element ⓔ is

$$\bar{K}^{ⓔ} = \begin{bmatrix} k_{11} & k_{12} & k_{13} & k_{14} & k_{15} & k_{16} \\ k_{21} & k_{22} & k_{23} & k_{24} & k_{25} & k_{26} \\ k_{31} & k_{32} & k_{33} & k_{34} & k_{35} & k_{36} \\ k_{41} & k_{42} & k_{43} & k_{44} & k_{45} & k_{46} \\ k_{51} & k_{52} & k_{53} & k_{54} & k_{55} & k_{56} \\ k_{61} & k_{62} & k_{63} & k_{64} & k_{65} & k_{46} \end{bmatrix} \tag{7.10}$$

$\delta^{ⓔ}$ is the displacements of node *i* and node *j* on element ⓔ,

$$\Delta(x)^{ⓔ} = \begin{pmatrix} u_i(x) & v_i(x) & \varphi_i(x) & u_j(x) & v_j(x) & \varphi_j(x) \end{pmatrix}^{T}$$

(7.11)

Then the bending strain ε_i can be obtained from the formula

$$\varepsilon_i(x) = \frac{M_i(x)y}{EI} \tag{7.12}$$

where, y is the distance from the neutral axis to the outmost cross-section fiber. E is the modulus of elasticity of the deck. I is the moment of inertia of the deck cross section.

Here, element② is taken as an example to calculate the bending strains. If the local coordinate system is consistent with the global coordinate system, the nodes' displacement vector of element② is

$$\Delta(x)^{②} = (u_3(x) \quad v_3(x) \quad \varphi_3(x) \quad u_2(x) \quad v_2(x) \quad \varphi_2(x))^{\mathrm{T}} \tag{7.13}$$

Using Eq. (7.3), Eq. (7.6) and Eq. (7.7), $\delta(x)^{②}$ can be obtained as following

$$\Delta(x)^{②} = [\mathrm{s}]'(F)' = \begin{bmatrix} s_{71} & s_{72} & s_{74} & s_{75} & s_{77} & s_{78} & s_{7,10} & s_{7,11} \\ s_{81} & s_{82} & s_{84} & s_{85} & s_{87} & s_{88} & s_{8,10} & s_{8,11} \\ s_{91} & s_{92} & s_{94} & s_{95} & s_{97} & s_{98} & s_{9,10} & s_{9,11} \\ s_{41} & s_{42} & s_{44} & s_{45} & s_{47} & s_{48} & s_{4,10} & s_{4,11} \\ s_{51} & s_{52} & s_{54} & s_{55} & s_{57} & s_{58} & s_{5,10} & s_{5,11} \\ s_{61} & s_{62} & s_{64} & s_{65} & s_{67} & s_{68} & s_{6,10} & s_{6,11} \end{bmatrix} \begin{pmatrix} F_{1\mathrm{h}}(x) \\ F_{1\mathrm{v}}(x) \\ F_{2\mathrm{h}}(x) \\ F_{2\mathrm{v}}(x) \\ F_{3\mathrm{h}}(x) \\ F_{3\mathrm{v}}(x) \\ F_{4\mathrm{h}}(x) \\ F_{4\mathrm{v}}(x) \end{pmatrix} \tag{7.14}$$

where, $(F)'$ is the cable force vector composed of non-zero forces, $[\mathrm{s}]'$ is the corresponding sub-matrix of K^{-1}.

Substituting Eq. (7.14) to Eq. (7.8) and Eq. (7.12), ε_3 and ε_2 can be obtained as

$$\begin{pmatrix} \varepsilon_3(x) \\ \varepsilon_2(x) \end{pmatrix} = \begin{pmatrix} \frac{M_3(x)y}{EI} \\ \frac{M_2(x)y}{EI} \end{pmatrix} = \frac{y}{EI} \begin{pmatrix} k_{31} & k_{32} & k_{33} & k_{34} & k_{35} & k_{36} \\ k_{61} & k_{62} & k_{63} & k_{64} & k_{65} & k_{66} \end{pmatrix} \begin{pmatrix} u_3(x) \\ v_3(x) \\ \varphi_3(x) \\ u_2(x) \\ v_2(x) \\ \varphi_2(x) \end{pmatrix} \tag{7.15}$$

The Eq. (7.15) is the relationship between cable forces and the bending strains of the bridge deck. From this equation, it can be found that each bending strain will be changed with different cable forces. This conclusion also applies to the three-dimensional model, but the expression

is more complicated. It is well known that the cable forces are different with different vehicle load and different vehicle location, and when one of the cables is damaged, all of the cable forces will be redistributed. Therefore, the bending strains are time-varying variable and can reflect the damage of the cables.

7.2.3 Damage identification approach

This section introduces the cable damage define and cable damage identification approach about the damage cable identification and the damage degree identification.

Damage in cables as a result of corrosion changes the cable cross-section and potentially mass per unit length. So the cable damage will affect the cable tensile stiffness *EA,* furthermore affect the cable tension forces. Therefore, in this paper, the cable damage is described using the cable tensile stiffness *EA* decreasing, and damage degree is calculated as following,

$$de = \frac{EA_{\text{in}} - EA_{\text{da}}}{EA_{\text{in}}} \times 100\% \tag{7.16}$$

where, *de* is the cable damage degree, EA_{in} is the intact cable tensile stiffness, EA_{da} is the damage cable tensile stiffness.

From the previous section, the bridge deck bending strains can reflect the damage of the cables, and are able to be measured easily with good accuracy, so the damage identification indexes will be extracted from measured bending strains. However, the amount of strain data is very large because of the variation with vehicle location. In order to reduce the large amount of data, this paper will extract the maximum bending strains of the measure points as the main features of the data. In a beam structure, the position concentrated force acting is usually the extreme point of the bending moment, equally, is also the extreme point of the bending strain. So in this paper, the measurement points only include 8 points which are on the bridge deck underside and corresponding to each cable anchor in this real cable-stayed bridge. Then the damage identification indexes are the difference between the maximum intact bending strains and the maximum damage bending strains, as following,

$$X = (\Delta\varepsilon_1 \quad \cdots \quad \Delta\varepsilon_i \quad \ldots \quad \Delta\varepsilon_n)^{\mathrm{T}} \tag{7.17}$$

where, X is the damage identification index column vector, $\Delta\varepsilon_i$ is the damage identification index at the No. 1 measure point, and the index is calculated by

$$\Delta\varepsilon_i = \max(\varepsilon_{i\mathrm{in}}) - \max(\varepsilon_{i\mathrm{da}}) \tag{7.18}$$

where, $\max(\varepsilon_{i\mathrm{in}})$ and $\max(\varepsilon_{i\mathrm{da}})$are the maximum bending strains of intact bridge and damage bridge at *i*th measure point under the same vehicle loads, respectively.

Each damage identification index vector X should correspond to a unique damage cable. In other words, when different cable is damaged or one cable is damaged in different degrees, the damage index vectors are different. Moreover, one damage cable *ic* may correspond to *num* damage identification index column vectors $\{X_{ic,1}, X_{ic,2}, \ldots, X_{ic,num}\}$. Although a certain damage cable has different damage degrees, the damage identification column vectors have the same characteristics that are different from other damage cables. So it can be determined that these different damage identification index vectors belong to the same category. If the total number of the cables on cable-stayed bridge is *nc*, the number of categories should be *nc*. Therefore, the damage cable identification problem is considered as a multiple classification problem. One of the machine learning methods, SVM, can be used to train a Damage Cable Identifier (DCI), as the following function

$$ic(X) = \arg\max\{\mathrm{sgn}(f_1(X)), \quad \cdots, \quad \mathrm{sgn}(f_{nc}(X))\} \tag{7.19}$$

where, X is the damage identification index vector. $\mathrm{sgn}(f_{nc}(X))$ is a two-class classifier, when X is corresponding to the damage cable of *nc*, $\mathrm{sgn}(f_{nc}(X))=1$, otherwise, $\mathrm{sgn}(f_{nc}(X))=-1$. $ic(\mathrm{X})$ equals the number of the damage cable which is corresponding to the maximum of the two-class classifiers. So $ic(\mathrm{X})$ is a multi-class classifier, in fact, that is the Damage Cable Identifier (DCI). Consequently, the damage cable can be identified by substituting any damage identification index column vector into Eq. (7.19).

After getting the damage cable, the next step is to identify the cable damage degree. The Damage Degree Identifier (DDI) will be trained using the damage degree identification index datasets which only includes the data of one damage cable situation. So corresponding to the number of the bridge cables, the number of DDIs should be *nc*, here it is 8. Because the damage degree is a continuous variable, it is impossible to prepare the training data corresponding all of the damage degree. This paper suggests that the damage degrees be 5%, 10%, 15%, 20%, etc. to prepare the training data. Then one of the regression methods, Support Vector Regression (SVR), is utilized to train DDIs. In DDI, the damage identification index column vector X is the independent variable, the damage degree *de* is the dependent variable. DDI is a nonlinear higher dimensional function as following,

$$de = f_{de,ic}(X) = \mathrm{A} \cdot X + b \tag{7.20}$$

where, $f_{de,ic}(\ )$ is DDI_{ic} for damage cable *ic*, $\mathrm{A} = \{a_1 \quad \cdots \quad a_\mathrm{n}\}$ is weight coefficient row vector, b is constant. Substituting any damage identification index column vector into Eq. (20), the result *de* is the damage degree.

In summary, this cable damage identification approach should be separated into two identifiers, because damage cable detection and the cable damage degree identification are absolutely different using different data mining method. In practical, this approach including three modules, Training module, Field data collection module and the bridge situation assessment module that can be applied as the following flow charts,

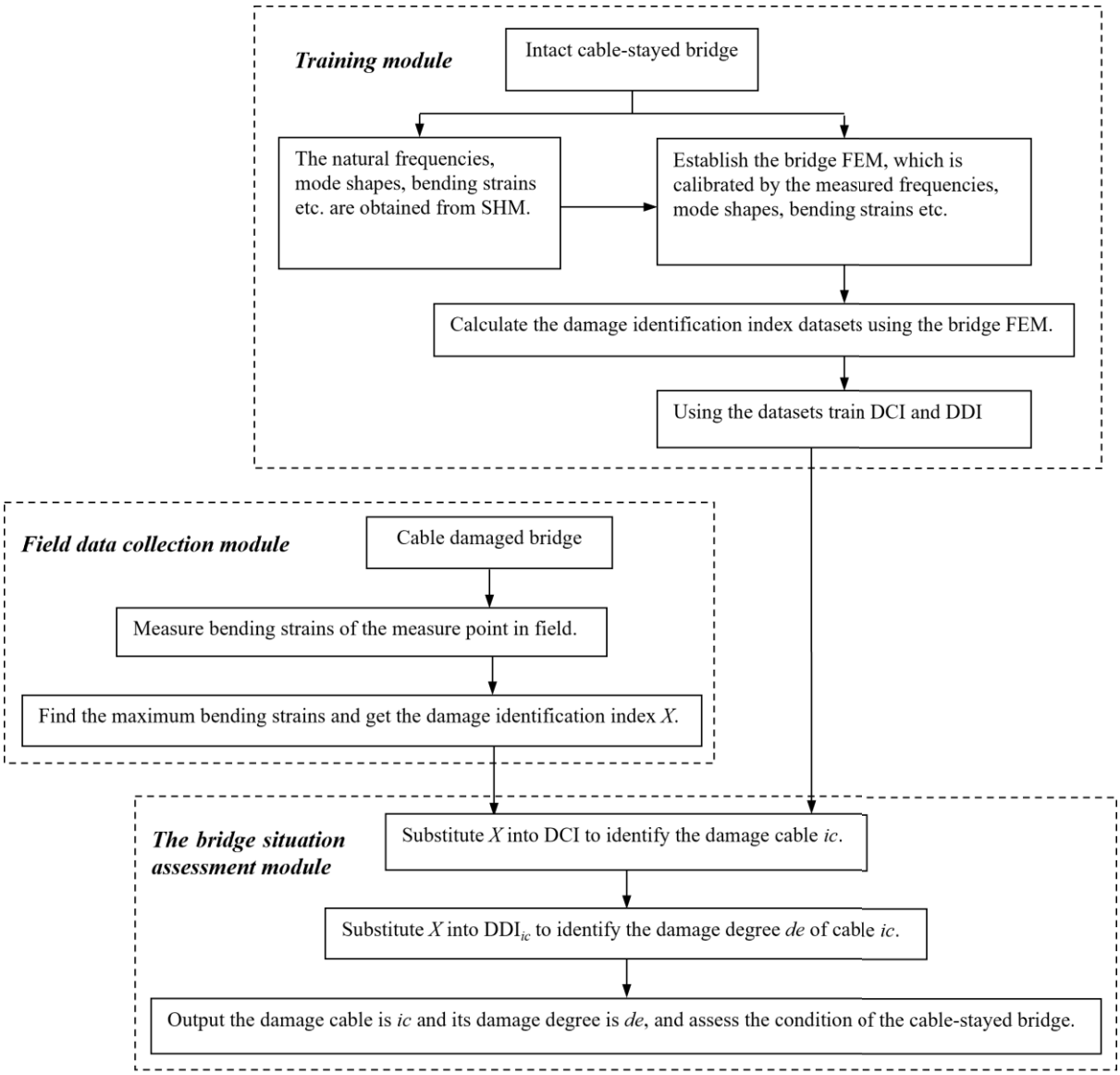

Figure 7.4 The flow chart of cable damage identification of cable-stayed bridge

7.3 The cable-stayed bridge SHM system and FEM

7.3.1 Description of the cable-stayed bridge SHM system

Structural health monitoring (SHM), having emerged since the early 1990s, is regarded as an important field experimental technique to understand the behaviours and performance of real, full-scale bridges under real loads and environmental conditions, and to further ensure the safety, service ability, durability, and sustainability of bridges.

In this paper, the real cable-stayed bridge is fully instrumented SHM to integrate structural health monitoring data with a numerical model of the bridge to assess structural capacity and to predict bridge deterioration over time. The monitoring system include 31 accelerometers for accelerations, 24 strain gauges for shear strains, 8 strain gauges on cables for cable tension strains, 6 uni-axial gauges under deck and 4 uni-axial gauges under the girders for bending strains, 1 temperature gauge and 1 dummy gauge. A grid of 24 timely-synchronized uni-axial accelerometers has been permanently installed under the bridge deck at the intersection of the girders and floor beams, and 4 uni-axial accelerometers installed on cable 1 to cable 4. They are used to capture vibration response of the structure and to identify natural frequencies, mode shapes, damping factors and identify any change in the dynamic characteristics of the bridge. Furthermore, the obtained modal parameters will be utilized to calibrate the finite element model of the bridge. The 24 accelerometers low-noise Silicon Designs accelerometers and can detect acceleration up to 62 g with an output noise of 10 mg/Hz and sensitivity of 2000 mV/g. The locations of the accelerometers are indicated in Figure 7.5. The location of the strain gauge sensors is elaborated in Figure 7.6. Most of the sensors were located in between CG6 and CG7. All eight cables were instrumented with uni-axial strain gauges, denoted by SA*i*(*i* = 23 to 30) in Figure 7.6. Uni-axial strain gauges SU*i*(*i*= 17 to 22) were mounted under the deck in either the longitudinal or transverse direction between Cross Girders CG6 and CG7. Strain gauges SU*i*(*i* = 13 to 16) were installed under the flange of the longitudinal girders at the middle of the span between CG6 and CG7 to measure bending strains. These strain gauges were also located close to mid-span of the bridge, where large deflections are expected. Shear rosettes were mounted at three different longitudinal locations along the bridge: the north end of the span near Cross Girder CG2 (north end span of the entire bridge), bridge mid-span close to Cross Girder CG6 (this was also located at the north end of the span between CG6 and CG7), mid-span close to Cross Girder CG6, and halfway between Cross Girders CG6 and CG7. These

strain gauges are implemented to collect shear, bending and tension strains to characterize passing traffics (speed, number of axles, distance between axles) and to identify the vehicle gross and axle weights. An HBM Quantum-X data acquisition system (HBM, Darmstadt, Germany) was adopted for signal conditioning and data logging. The Quantum system provides an integrated and reliable device to log high-quality data with 24-bit resolution with a bandwidth capability of 0–3kHz. The response signals of the bridge were collected at 600Hz while various controlled test vehicles were traveling over the bridge, and, is recorded every 10 min in a file.

Figure 7.7(a), (b) shows typical 10-minute acceleration response obtained from sensor A19 (see Figure 7.5) and bending strain response obtained from sensor SS11 (see Figure 7.6). In Figure 7.7, the presence of passing traffic is obvious that two vehicles have passed over the bridge.

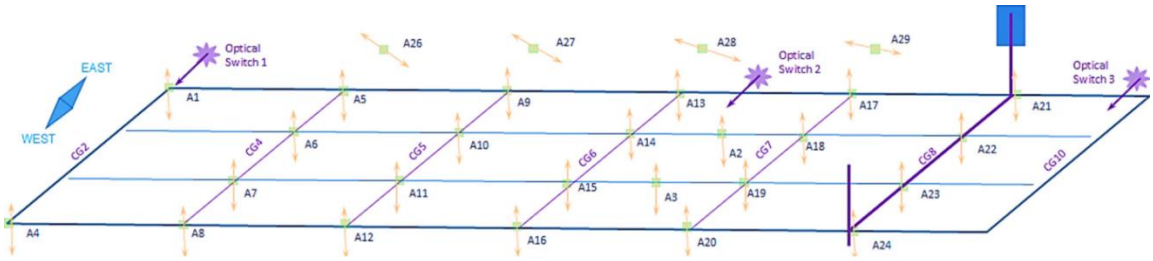

Figure 7.5 Illustration of the accelerometer sensor locations (A1:A24) on the cross girders (CGs)

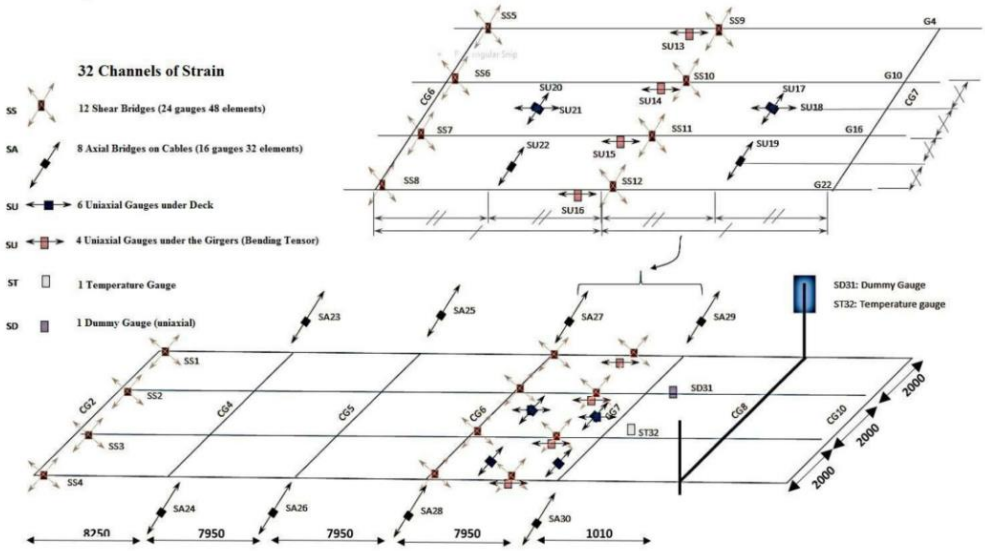

Figure 7.6 Illustration of the strain gauges array

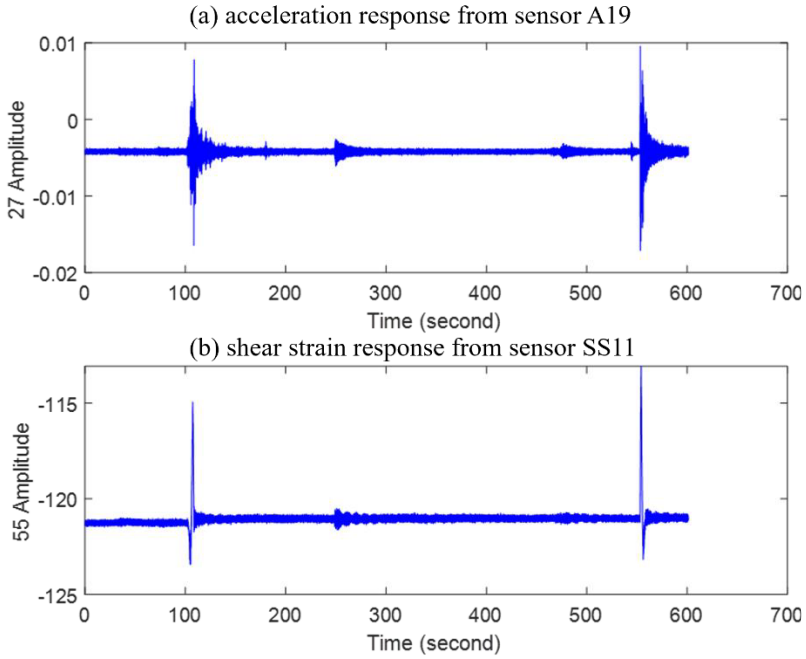

Figure 7.7 Illustration of 600 seconds response: (a) Acceleration response from sensor A19; (b) Shear strain response from sensor SS11

7.3.2 FEM of the cable-stayed bridge

The finite element model of the cable-stayed bridge was established utilizing ANSYS. The bridge deck is a composite steel-concrete deck, so the steel reinforced concrete part is simulated

by SHELL63 with 160 mm thickness, the under longitudinal and transverse girders are simulated by BEAM189 which have Universal Beam (410UB54) cross sectional properties. These two kinds of elements are coupled at their co-nodes. The cables are super grade circular bar with a diameter of 38 mm and are all pre-tensioned cables using LINK10 to simulate. At the cable anchorage footing, all of the degrees of freedoms are restrained. The bridge mast has a non-prismatic cross section, starting with a rectangular section of 700mm×800mm at the base and 500mm×800mm at the uppermost level. So in the cable-stayed bridge finite element model, BEAM189 with variable section is adopted to simulate the mast, and all degrees of freedoms of the mast base are restrained. At abutment A, there is a pin support under every longitudinal deck. On the other side of the deck, roller supports are used at abutment B. After meshing elements, the FEM consists of 35,112 SHELL63 elements and 4,176 BEAM189 elements and 16 LINK10 elements. The convergence study has been conducted and the FEM of the cable-stayed bridge is shown in Figure 7.8.

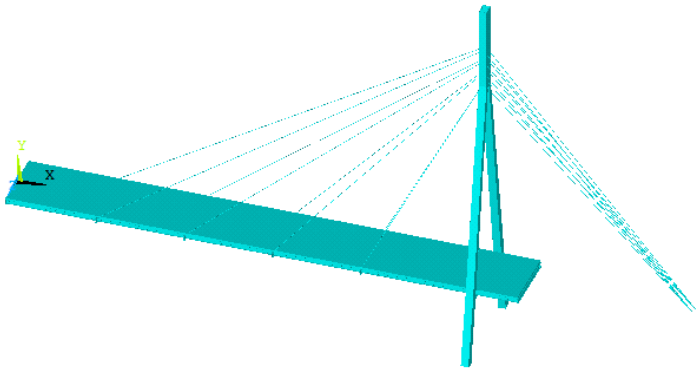

Figure 7.8 The FEM of the cable-stayed bridge

7.3.3 Verification of the FEM

Based on the SHM system monitoring dynamic data, the FEM of the cable-stayed bridge is updated. In the FEM, some parameters are uncertain. For instance, because the cross girders have many circular openings for service ducts (CG8 as an example shown in Figure 7.9), their

cross section areas and moment of inertia are uncertain. And because the deck has reinforced steels and pavement, its density and modulus of elasticity are uncertain. So a function for the first natural frequency of the cross-section properties can be established as,

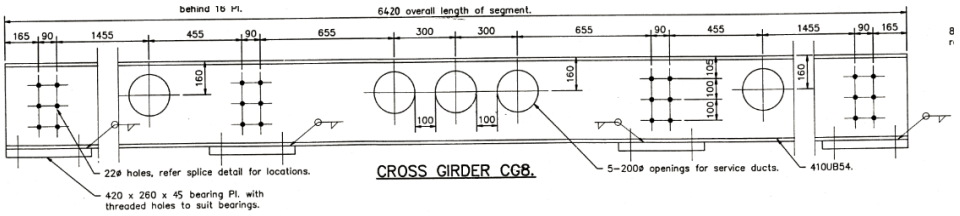

Figure 7.9 The cross girder CG8 details

$$f_1 = \mathrm{FEM}(A_\mathrm{c}, I_\mathrm{c}, E_\mathrm{d}) \tag{7.21}$$

where, f_1 is the monitoring first natural frequency. FEM() is the finite element model of the cable-stayed bridge. A_c and I_c are the updated cross section areas and moment of inertia of the cross girder, respectively. E_d is the updated modulus of elasticity of the deck. Because A_c and I_c effect the cross girder tension stiffness $E_\mathrm{c}A_\mathrm{c}$ and bending stiffness $E_\mathrm{c}I_\mathrm{c}$, the cross section can be the designed cross section Universal Beam (410UB54), then to modify the modulus of elasticity E_c. So the function for the first natural frequency is simplified as

$$f_1 = \mathrm{FEM}(E_\mathrm{c}, E_\mathrm{d}) \tag{7.22}$$

Based on practical experience, the modulus of elasticity E_d of the steel reinforced concrete can be 1~1.2 times of the plain concrete, here

$$E_\mathrm{d} = 1.2 \times E_P = 1.2 \times 3.6 \times 10^{10}\mathrm{Pa} = 43.2\mathrm{GPa} \tag{7.23}$$

where, E_p is the modulus of elasticity of plain concrete.

After calculating,

$$E_\mathrm{c} = 1.002 \times E_s \approx E_s = 210\mathrm{GPa} \tag{7.24}$$

where, E_s is the modulus of elasticity of steel.

Then the FEM modals and frequencies are calculated, and compared with the test data. Table 1 shows the first five FEM frequencies and the test frequencies, respectively. It can be found that the corresponding frequencies are close, and the maximum difference is -0.700 Hz which is the fourth frequency. Figure 7.10 shows the Comparison between the 1st FEM mode shape and the corresponding test mode shape (Zhu et al. 2017), it shows that these two mode shape are agreed well. Figure 7.11 shows the first five mode shapes of the cable-stayed FEM. From these results, it indicates that the FEM can represent the bridge global stiffness.

Table 7.1 Frequencies from the finite element model and filed measurements

Mode No.	FEM Frequency (Hz)	Test Frequency (Hz)	The difference (Hz)
1	2.039	2.014	0.025
2	3.301	3.510	-0.209
3	4.254	3.645	0.609
4	4.838	5.538	-0.700
5	5.611	6.068	-0.457

Note: the difference= FEM Frequency- Test Frequency

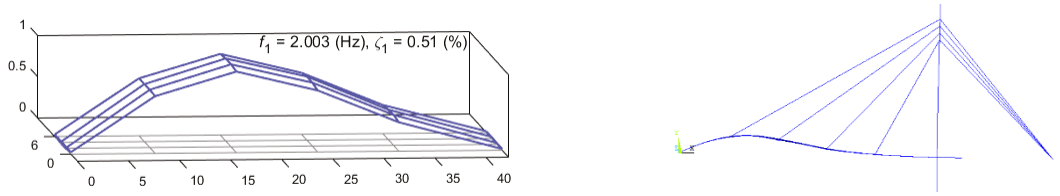

(a) the 1st test mode shape (b) the 1st FEM mode shape

Figure 7.10 The 1st mode shape: (a) identified from test; (b) obtained from FEM

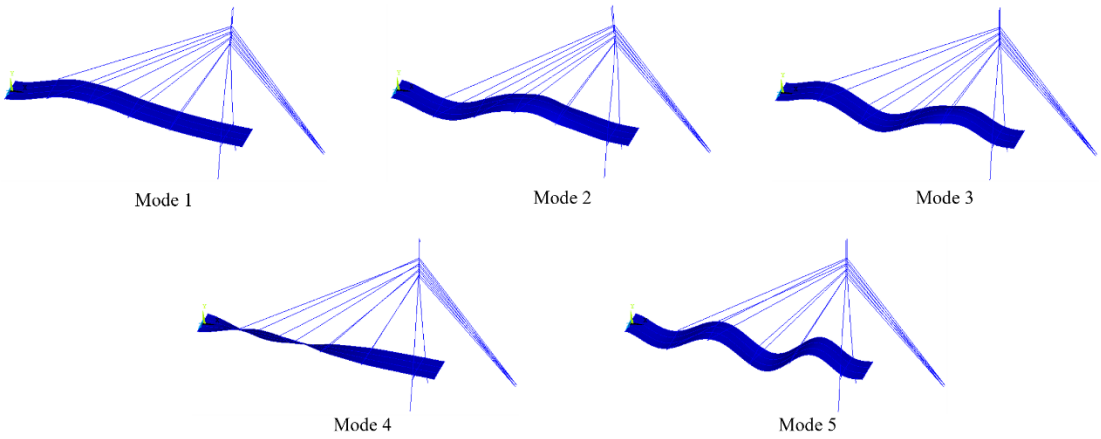

Figure 7.11 The first five mode shapes of the cable-stayed FEM

Figure 7.12 The test vehicle

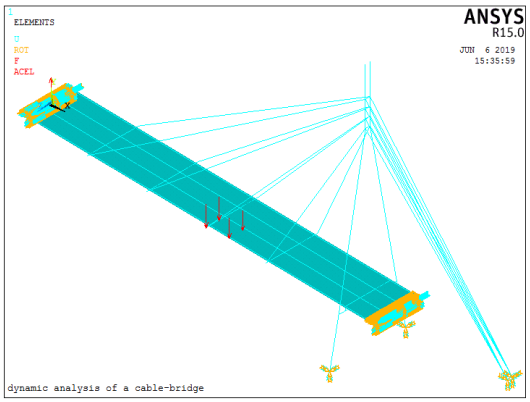

Figure 7.13 The vehicle load on the FEM of the cable-stayed bridge

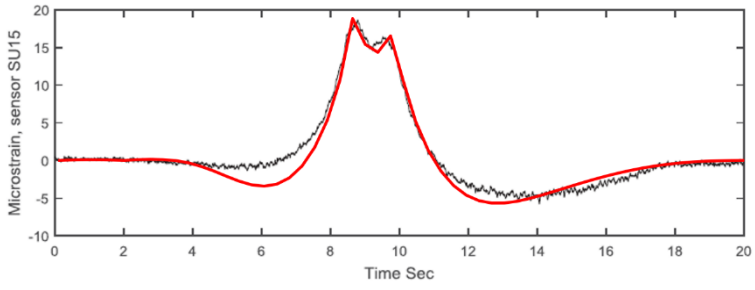

Figure 7.14 The measured strain response (black line) and the FEM strain response (red line)

Furthermore, there is also a comparison of the bending strain dynamic response between the FEM and the field measurements. The response measuring sensor is the SU15, which is located on the longitudinal deck just in between transverse beam CG6 and CG7 as indicated in Figure 7.6. The sensor time responses of the bridge are continuously measured at a sampling frequency of 600 Hz and, are recorded every 10 min in a file. In the field test experiment, a Holden Colorado Ute was used as a test vehicle, see Figure 7.12. The gross weight of the test vehicle was 2.2 t, with front and rear axle weights of P1 = 1.20 t and P2 = 1.00 t, respectively. The distance between the axles was d = 3.1m.The test vehicle was driving at approximately a constant speed of 10 km/h from the South to the North of the bridge along the centreline. Figure 7.13 is the vehicle load on the FEM of the cable-stayed bridge. Figure 7.14 illustrates the measured strain response (black line) and the FEM strain response (red line). The measured strain response is obtained from the sensor SU15 after removing the static component induced by non-traffic loading e.g., dead load. The presence of two peaks, corresponding to two axles with front axle being heavier than the rear axle, can be clearly seen in both the measured and calculated bending responses in Figure 7.14. From Figure 7.14, these two lines are very close, and the maximum values are almost the same. Therefore, the FEM can represent the cable-stayed bridge, and then its calculated results are reliable to research the cable damage identification.

7.4 Single cable damage identification

7.4.1The damage identification indexes

The damage identification indexes are obtained from the bending strain responses of the longitude deck which are near the cable anchor. The vehicle load also used the Holden Colorado Ute which travels along the bridge centreline. Figure 7.15 shows the bending strain response under the cables 1-4 and the cables 9-12, when the bridge is intact and the cross

section of the cable 4 is damaged 30% (calculated by Eq. (7.16)). And Figure 7.15 shows the same responses of the intact bridge and the damage bridge with the cable 8 damaged 30%.

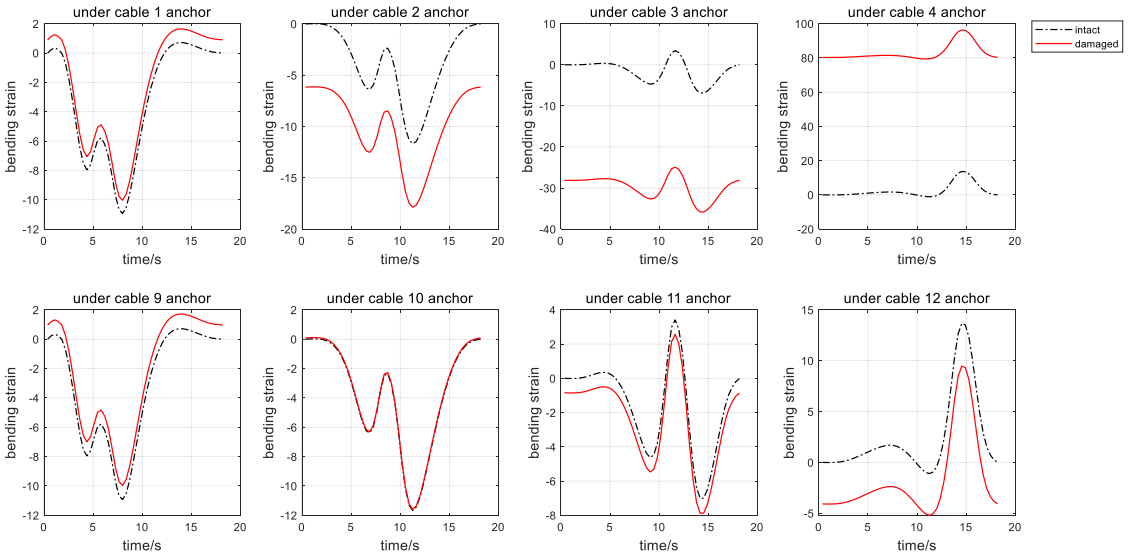

Figure 7.15 Bending strain response under the cables 1-4 and cables 9-12, when the bridge is intact and the cable 4 damaged 30%

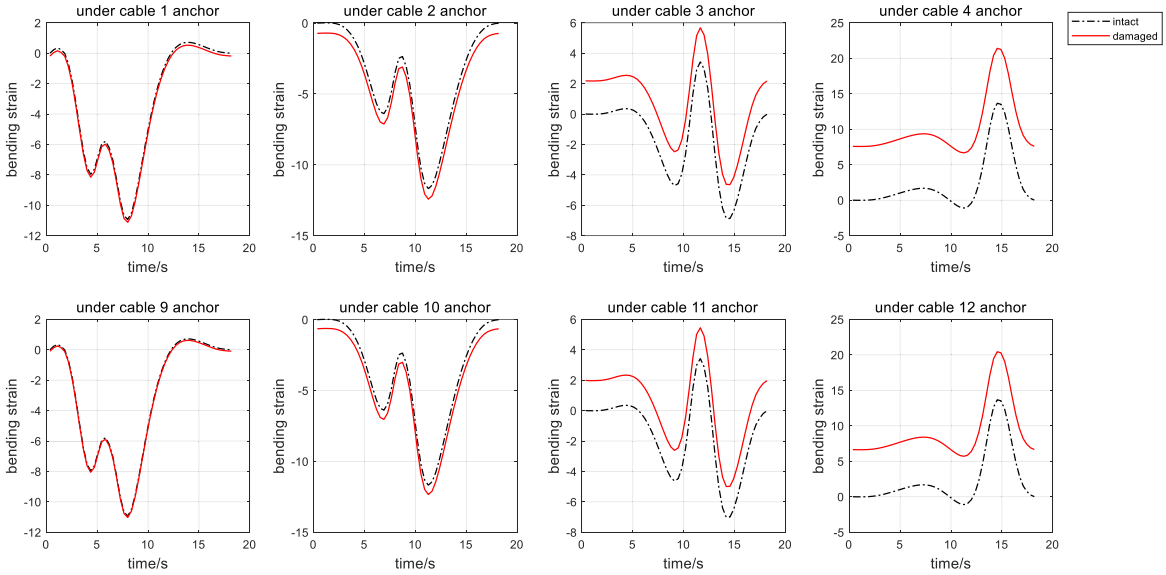

Figure 7.16 Bending strain response under the cables 1-4 and cables 9-12, when the bridge is intact and the cable 8 damaged 30%

From Figures 7.15 and 7.16, it is obviously that the deck bending strain would be changed when the cable is damaged, especially near the damaged cable or the corresponding cable, such

as the cable 8 corresponded with the cable 4. But only according to these curve lines cannot identify the damage cable or the damage degree. From Figure 7.16, for example, it is difficult to determine which cable is damaged, the cable 8 or the cable 16. In other words, these lines are not sensitive to the cable damage. Therefore, a new damage identification index is proposed in this paper.

Firstly, the bending strain differences between the intact bridge and the damaged bridge are calculated. Then corresponding to each cable anchor (cables 1-4, and cables 9-12), the difference between the maximum bending strains can be found (calculated by Eq. (7.18)). At last, a damage identification indexes vector is obtained, including 8 differences (corresponding to cables 1-4, and cables 9-12). Figure 7.17 shows the damage identification indexes poly line diagrams when the cables 1-8 cross sections are reduced 30%, respectively. The measure points 1-8 are respectively under the cable anchors of cables 1-4 and cables 9-12.

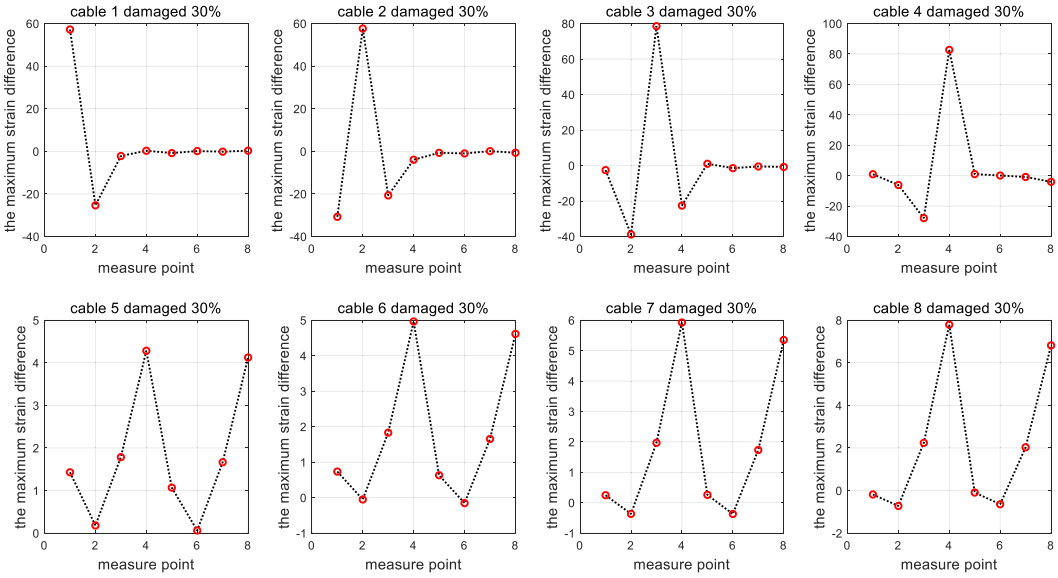

Figure 7.17 The damage identification indexes poly line diagrams when the cables 1-8 cross sections are reduced 30%

Figure 7.17 indicates that the poly line diagrams are significant unique from each other when the cables 1-4 are damaged, respectively. The poly line diagrams shapes of the cables 5-8 are

similar, but each corresponding measure point values are different. These damage identification indexes can be used to identify the cable damage. This problem could be considered as a multi-classification problem and can be solved by Support Vector Classifier (SVC).

Then according to symmetry, the other damage identification indexes of the cables 9-16 can be calculated based on the above damage identification indexes of the cables 1-8. Figure 7.18 is the corresponding damage identification indexes poly line diagrams which are calculated by symmetry.

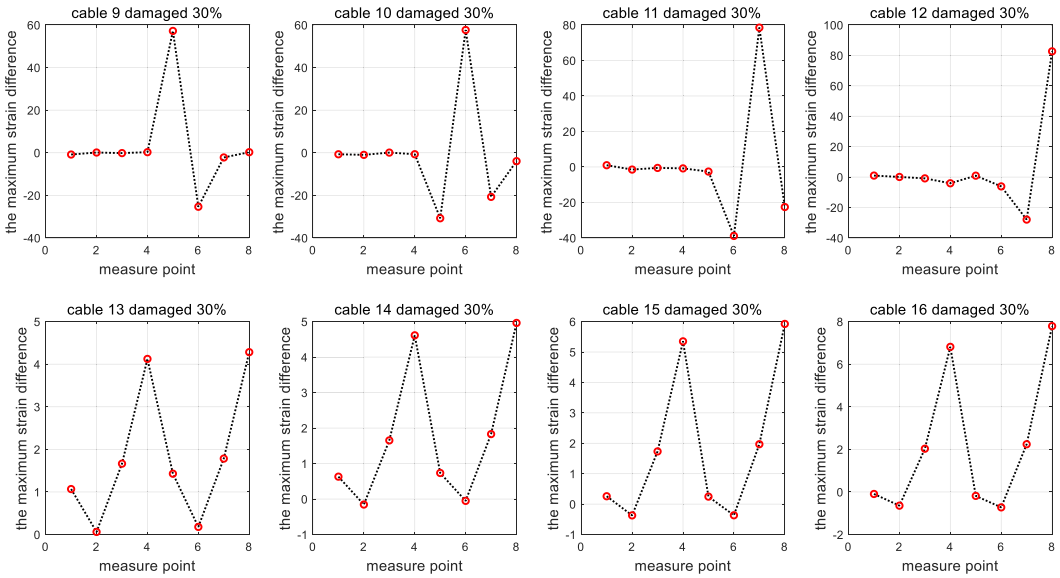

Figure 7.18 The corresponding damage identification indexes poly line diagrams which are calculated by symmetry

Furthermore, the feasibility of these damage identification indexes used to identify the damage severity is also studied. Using FEM, when the cable 4 cross section is reduce by 10%, 20% and 30% respectively, the corresponding damage identification indexes are calculated and their poly line diagrams are drawn in Figure 7.19.

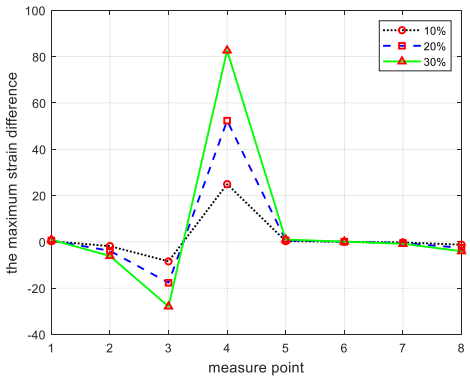

Figure 7.19 The damage identification indexes poly line diagrams when the cable 4 cross section is reduced 10%, 20% and 30%

Figure 7.19 shows that the absolute values of damage identification index increase as the damage degree increases in cable 4, and their shapes are similar. Therefore, the cable damage degree identification can be considered as a regression problem. In the later sections of this paper, the Support Vector Regression machines (SVR) will be utilized to establish DDI.

7.4.2 Training datasets and testing datasets

Before training DCI and DDI, the training datasets and the testing datasets should be prepared firstly. The validated numerical model has been used to generate a large amount of datasets. The datasets are split into 70% for training and 30% for testing.

(1) Training datasets

For the damage cable identification, the original training datasets contains 16 damage index vectors, when the cable 1-16 are damaged 30%, respectively. In order to increase the number and the randomness of the training datasets, there are three steps to process the original datasets. First of all, the original datasets are expanded by Eq. (7.25).

$$\{x\}_{ei} = \{x\}_c \times (1 + \varepsilon R_i)(i = 1,2,\cdots,n) \tag{7.25}$$

where, $\{x\}_{ei}$ is the ith expanded data vector. $\{x\}_c$ is the original calculated data vector. ε is the noise level. R_i is the ith datum of the normal distribution random data which the mean value is

0 and the mean square deviation is 1. Here n is 15 and ε is 0.1%, the number of original data is 16. So after expanding, the index vectors number of training datasets is 240.

The second step is to add white noise into each value of the expanded training datasets, using the following equation:

$$x_{tij} = x_{eij} \times \left(1 + \varepsilon R_j\right)(j = 1,2,\cdots,m) \tag{7.26}$$

where, x_{tij} is the jth value of the ith training vector. x_{eij} is the jth value of the ith expanded vector. ε *and* R_i are same with the meaning in Eq. (7.25). Here ε is 1%, m is 8, because the number of the measure points is 8.

At last, the training vectors should be normalized in [0,1] to increase the identification accuracy and reduce errors. In Matlab, it can be processed by the function "mapminmax ", and its algorithm is

$$f: x_{tij} \to X_{tij} = \frac{x_{tij} - x_{ti\min}}{x_{ti\max} - x_{ti\min}} \tag{7.27}$$

where, $x_{ti\min}$ is the minimum of the vector $\{x\}_{ti}$, $x_{ti\max}$ is the maximum of the vector $\{x\}_{ti}$. X_{tij} is the normalized value. Then the training datasets [X] for the damage cable identification is obtained, which is a 240×8 matrix.

For damage degree identification, the cable 2 is taken as an example. The damage identification indexes are calculated using the former FEM, when the cable 2 damage degrees are 10%, 20% and 30% respectively. So the original damage degree identification training datasets only contains 3 indexes vectors and their poly line diagrams have shown in Figure 7.19. They also are added white noise to simulate measure datasets. In Eq. (7.25), n is 40 and ε is 1%, the number of the expanded training datasets is 160. In Eq. (7.26), ε is 1%, m is 8. It must be mentioned that this training datasets do not need to be normalized. Finally, the training datasets [x] for the damage degree identification is obtained, which is a 160×8 matrix.

(2) Testing datasets

In order to test the damage identifier generalization capability and anti-noise capability, the hypothetical damage scenarios are listed in Table 7.2. The damage indexes in Table 7.2 are also calculated by FEM and not calculated using symmetry.

Table 7.2 The hypothetical damage scenarios

	Damage cable No.	Damage degree	Remarks
Damage cable identification test scenarios	1	10%, 20%	Not included in the training datasets
	2	10%, 20%, 25%	
	3	10%, 20%	
	4	10%, 20%	
Damage degree identification test scenarios	2	10%, 20%, 25%, 30%	25% is not included in the training datasets
Damage cable identification test scenarios	10	25%	Not included in the training datasets
	11	20%	
	14	20%	

Then the damage cable identification test dataset is a 12×8 matrix. And the damage degree identification test dataset is a 4×8 matrix. All of the testing datasets are not added into white noise.

At the following sections, the Support Vector Machine (SVM) will be utilized to train DCI and DDI, which are based on the above training datasets.

7.4.3 Damage cable identification

It has been mentioned that the damage cable identification is a multi-classification problem. Therefore, on the Matlab platform, the function "fitcecoc" is convenient to be used to train DCI. The identified damage cables and the actual damage cables are shown in Figure 7.20.

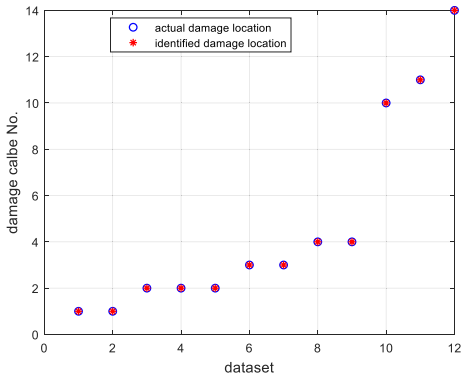

Figure 7.20 The identified damage cables and the actual damage cable

Although the testing datasets is not included in the training datasets, it can be observed from Figure 7.20 that the identified results are correct. Since there are many disturbances in the field experiment environment, studying the anti-noise capability of DCI is necessary. The following noise levels 1%, 3%, 5%, 10%, 15%, 20%, 25%, 30% are considered and added into the testing datasets using Eq. (7.26). These noised test datasets as input in DCI are calculated and the identification result is show in Figure 7.21.

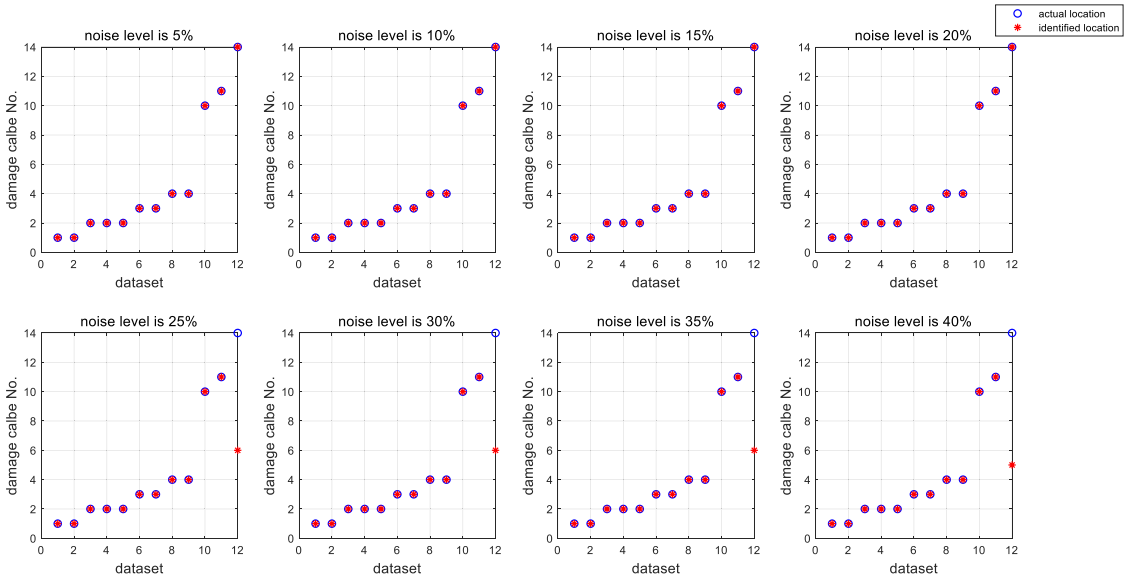

Figure 7.21 The comparison between the actual damage cable and the identified damage cable with different noise levels

From Figure 7.21, when the noise level is under 20%, the identification accuracy of DCI is 100%. And with the increasing of the noise level, even up to 40%, there is only one misidentification. The cable 16 is misidentified as the cable 6 or 5, they are all the backstay cables and the cable 6 is symmetry with the cable 14. But the damage cables of the cable 1-4 and the cable 10-11 are not misidentified. So this DCI has excellent anti-noise capability, especially for the main load bearing cables (cable 1-4, 9-12) in this cable stayed bridge.

7.4.4 Damage degree identification

After finishing the damage cable identification, damage degree recognition will be studied in this part. At first, the training datasets [x], which is obtained at section 7.4.2, is used to train DDI by Support Vector Regression machines (SVR) at Matlab platform. Then the testing dataset is input in the DDI, and the output results are the damage degree of cable 2. The output results and the actual damage degree are all shown in Table 7.3 and Figure 7.22. And Figure 7.23 shows the identified damage degree results when the test data is added in different noise levels, such as 5%, 10%, 15%, 20%, 25%, 30%, 35%, 40%. Table 7.4 lists the corresponding errors.

Table 7.3 The identified damage degrees of DDI

Actual damage degree/%	Identified damage degree/%	error/%	Remarks
10	10.0937	0.1999	Included in the training datasets
20	19.4116	-0.6198	
30	30.4295	0.2357	
25	24.6800	-0.4291	Not included in the training datasets

where, $\text{error} = \text{identified damage degree} - \text{actual damage degree}$

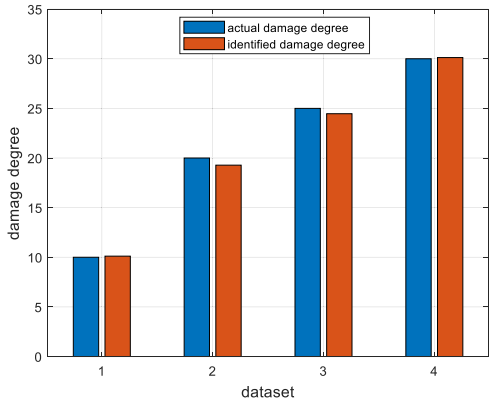

Figure 7.22 The comparison between the actual damage degrees and the identified damage degrees of DDI

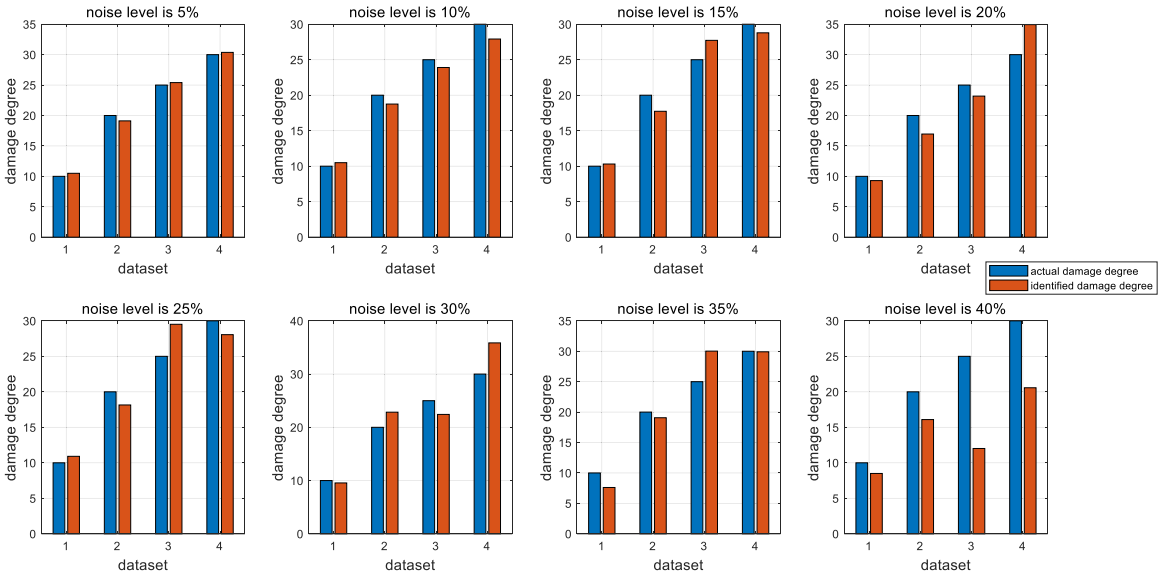

Figure 7.23 The comparison between the actual damage degrees and the identified damage degrees with different noise levels

Table 7.4 The damage identified degrees error with different noise levels (unit: %)

Noise level	5%	10%	15%	20%	25%	30%	35%	40%
Damage degree of 10%	0.49	0.49	0.30	-0.70	0.91	-0.44	-2.38	-1.50
Damage degree of 20%	-0.88	-1.24	-2.26	-3.04	-1.851	2.84	-0.92	-3.91
Damage degree of 25%	0.40	-1.09	2.72	-1.81	4.514	-2.57	5.02	-12.98
Damage degree of 30%	0.37	-2.08	-1.21	4.93	-1.946	5.85	-0.09	-9.42

From Table 7.3 and Figure 7.22, the identified damage degrees are very close to the actual damage degrees, the maximum absolute value of the error is only 0.61%, when the damage degree is 20%. The DDI can correctly identify the damage degree of 25%, which isn't included in the training datasets, and the identification error is only -0.42%. It is demonstrated that DDI can accurately identify the damage degree and have good generalization capability.

In Figure 7.23 and Table 7.4, with the noise level increasing, the identification errors of damage degree also have a tendency to increase. Except the noise level 40%, the identified damage degrees are closed to the actual damage degrees, the maximum error is 5.85% when the noise level is 30% and corresponding actual damage degree is 30%. Even the noise level is up to 30%, the identified damage degree is very close to the actual value when the damage degree is 10%, and the maximum error is just 0.91%. So the DDI can well identify the damage degree, have good generalization capability and strong anti-noise performance.

7.5 Double damage cables identification

7.5.1 The double damage cables identification datasets

(1) Training datasets

In real situation, there may be two damaged cables simultaneously. Based on the single cable damage identification indexes and superposition principle, the double cables damage indexes can be obtained as the following flow chart (Figure 7.24).

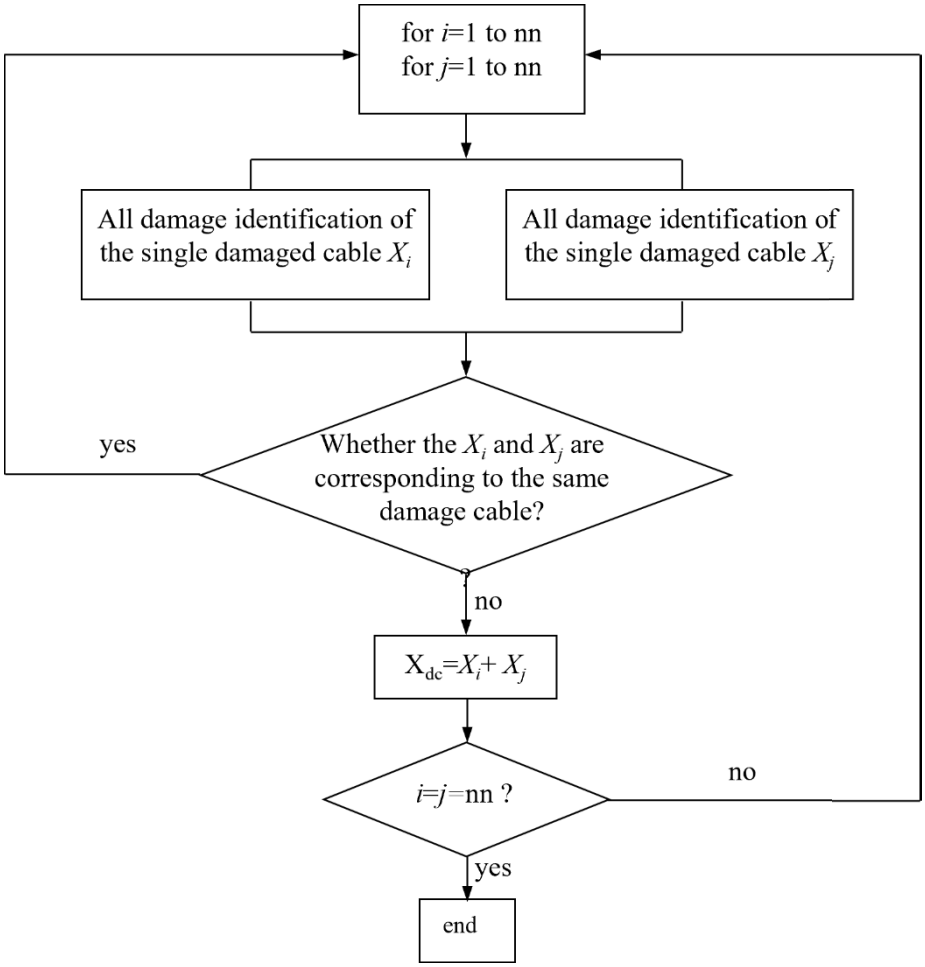

Figure 7.24 The flow chart of calculate training datasets for double damage

In Figure 7.24, X is the training datasets for single damage cable identification. So nn is the total number of the damage index vectors in X, here nn=16. X_{dc} is the double cables damage identification training datasets, its total number of index vectors is nd=120. It also can be expanded and added noise by Eq. (7.25) and Eq. (7.26), where n is 5 and ε is 0.1%, m is 8. So after expanding, the index vectors number of training datasets is 600.

For double damage cables damage degree identification, different DDIs should be trained for different damage cables. The training datasets can be obtained as the flow chart in Figure 7.25. Where, the $X_{cn,i}$ and $X_{cm,j}$ are corresponding to damage identification index vectors of the identified damage cables cn and cm with 10%, 20%, 30% damage degrees, respectively. In this paper, it is assumed that the cable 1 and the cable 2 are simultaneously damaged. So the damage

degree identification training datasets contains 9 indexes vectors. They also can be added white noise to simulate measure datasets. In Eq. (7.25), n is 20 and ε is 0.1%, the number of the expanded training datasets is 180. In Eq. (7.26), ε is 0.1%, m is 8.

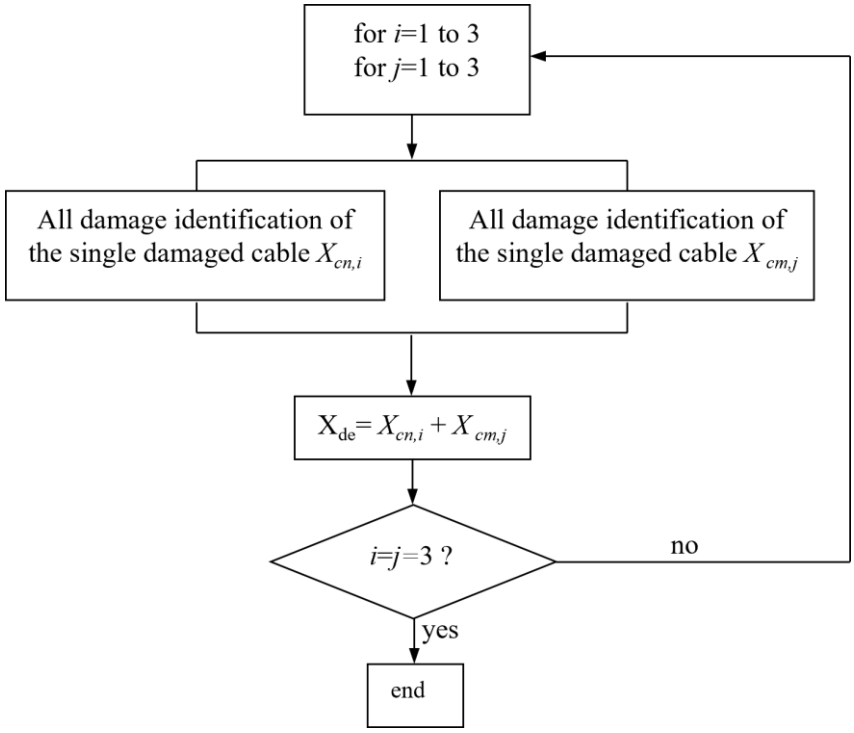

Figure 7.25 The flow chart of calculate training datasets for double damage cables

(2) Testing datasets

In order to test the identification results of DCI and DDI, the hypothetical damage scenarios are listed in Table 7.5. The damage identification indexes in Table 5 are fully calculated by FEM.

Table 7.5 The hypothetical damage scenarios of double damage cables

The number of damage scenarios	Damage cable	Damage degree	Damage cable	Damage degree
①	1	10%	2	20%
②	1	20%	11	10%

The damage identification index vectors, corresponding to the scenarios in Table 7.5, are added white noise by Eq. (7.26) to get the testing datasets $DATA_{td}$, the noise levels include 5%, 10%,

15%, 20%, 25%, 30%, 35%, 40%.Then, SVM will also be utilized to train DCI_d and DDI_d for double damage cables identification, which are based on the above training datasets.

7.5.2 The double damage cables identification

On the Matlab platform, DCI_d is trained using the function "fitcecoc". Then, the testing datasets $DATA_{td}$ are input into DCI_d to identify the damage cables. The identified damage cables and the actual damage cables are shown in Table 7.6.

Table 7.6 The double damage cables identification results

Noise level	0%		5%		10%		15%		20%		25%		30%		35%		40%	
Scenario ①	1	2	1	2	1	2	1	2	1	2	1	2	1	2	1	2	2	1
Scenario ②	1	11	1	11	1	11	1	11	1	11	1	11	1	11	1	11	1	11

Although the training datasets are just obtained by superposition principle, DCI_d can exactly identify the damage cables, even when the noise level is 40% (shown in Table 7.6). It is shown that the training datasets can be obtained by superposition principle based on single cable damage datasets for multiple damage condition, such as two cables damage or more. It is also indicate that DCI_d has good anti-noise capability.

7.5.3 Double damage degree identification

If damage scenarios ② in Table 7.5 has been identified, the training datasets X_{de} can be obtained as flow chart in Figure 7.25, where cn=1, cm=11. DDI_d is trained by Support Vector Regression machines (SVR) at Matlab platform. Then the testing datasets about damage scenarios ② is input in the DDI_d, and the output results are the damage degree of cable 1 and cable 11, respectively. The identified damage degree and the assumed damage degree with different noise levels and the errors are all shown in Table 7.7.

Table 7.7 The double damage cables damage degree identification results of damage scenarios

Noise level	The assumed damage cable	The assumed damage degree (%)	The identified damage degree (%)	error (%)
0%	1	20	19.21	-0.79
	11	10	10.08	0.08
5%	1	20	18.90	-1.10
	11	10	10.29	0.29
10%	1	20	18.18	-1.82
	11	10	10.66	0.66
15%	1	20	19.57	-0.43
	11	10	9.39	-0.61
20%	1	20	20.25	0.25
	11	10	8.86	-1.14
25%	1	20	16.93	-3.07
	11	10	9.84	-0.16
30%	1	20	22.93	2.93
	11	10	9.21	-0.79
35%	1	20	15.58	-4.62
	11	10	7.90	-2.10
40%	1	20	23.20	3.20
	11	10	9.75	-0.25

where, $\text{error} = \text{identified damge degree} - \text{assumed damage degree}$

From Table 7.7, the identified damage degrees are very close to the assumed damage degrees, the maximum error is just -4.62% of the damage cable 1 with the noise level of 35%. When the noise level is lower than 20%, the identified error is less than 2%. It can be found that the identified errors are increased with the noise level increasing, except some individual cases. This example also shows that the method of obtaining the training datasets using superposition principle based on single cable damage datasets for multiple damage condition is correct and can be used in real condition. DDI_d has good anti-noise capability.

7.6 Summary

Bending strain-based DCI and DDI are proposed to identify the damage cable and the cable damage degree in a cable-stayed bridge using SVM in this paper. A cable-stayed bridge FEM is established using ANSYS, and validated by the measured mode, frequencies and its bending strain responses. Then utilizing the FEM, numerical simulations are carried out for verification of the proposed method. DCI and DDI are respectively trained for damage cable identification and damage degree identification and checked using the testing datasets. Based on the single damage cable identification datasets, DCI_d and DDI_d are proposed to identify double damage cables. Some conclusions can be made as follows:

1) DCI can accurately identify the damage cable, when the test data isn't included in the training datasets. And even when the noise level is up to 40%, the identification error only appears on one cable. DDI also works well on identifying the damage degrees, the maximum error is only -12.98% when the noise level is 40%. Their identification results show that DCI and DDI both have good generalization capability and anti-noise capability.
2) In Double damage cables case study, DCI_d and DDI_d also both have good generalization capability and strong anti-noise performance.
3) The new idea that damage cable identification problem is a multi-classification issue and damage degree identification problem is a nonlinear regression issue, is correct. The proposed method has strong anti-noise performance and can be easily adapted to field health monitoring system.

Chapter 8 Conclusions and recommendations

8.1 Conclusions

The methods for structural operational load and damage identification have been developed in this thesis. The novelty of the load identification method lies in the use of the strong correlation of adjacent column vectors in the transfer matrix and the specific characteristics of the loads. Numerical and experimental studies were conducted to verify the proposed methods. The novel interface monitoring system solves the problem that the traditional slippage measurement cannot be applied in practice. And this new sensory system is suitable to use in the whole bridge life cycle. The new method for localization and quantitative identification of cable damage treats damage cable identification problem as a multi-classification issue and damage degree identification problem as a nonlinear regression issue. The proposed method has strong anti-noise performance and can be easily adapted to field health monitoring system. A detailed summary by this thesis ass below:

1) A truncated transfer matrix-based regularisation method is proposed for the impact force identification. This method includes two steps. First step is the force location identification. Once the force location is determined, the transfer matrix can be constructed. Then the second step is to identify the force values using a truncated transfer matrix-based regularisation technique. The validation of the proposed method is conducted numerically on a simply supported beam model and experimentally on a steel-concrete composite bridge. The results are compared with that by the classical Tikhonov ($l2$-norm) regularisation method and the standard sparse ($l1$-norm) regularisation method. The results show that the proposed method has the better accuracy and time efficiency on the impact force value identification. The effect of measurement noise, the number of modes and

sensors are also discussed. The results show that the proposed method has a good applicability and accuracy for practical applications.

2) A low-rank transfer submatrix-based group sparse regularisation method for impact force localization and reconstruction is proposed. With this technique, the localization and time history reconstruction of the impact force could be realized simultaneously in a determined situation with one sensor configuration. Its robustness and adaptivity with respect to different ranges of the partial matrix, the noise level and the number of the impact forces are numerically validated on a simple supported beam and compared with L1-norm regularisation method and L2-norm regularisation method numerically and experimentally. The proposed low-rank transfer submatrix based group sparse regularisation method has good robustness and identification accuracy in these cases and has the best performance on the impact force localization and time history reconstruction comparing with L2-norm regularisation method and L1-norm regularisation method.
3) A group weighted Tikhonov regularisation method is proposed for moving force identification via equivalent nodal forces. The moving force could be transferred into equivalent nodal forces, which have the group sparse feature. Its effectiveness and applicability are studied numerically on a simply supported beam in comparison with the standard sparse regularisation method and the classical Tikhonov regularisation method.
4) A new interface slippage monitoring system has been developed to measure directly the relative displacement between the concrete slab and steel girder. The detailed design, working principle and calibration of the slip sensor are presented. The calibration results demonstrate that the sensors are very sensitive to the slip, and experimental studies demonstrate that the slip sensor has a good performance for interface slippage measurement. An accurate finite element model is developed and validated against the experimental results, and parametric studies base on this numerical model were performed

to investigate the variation in shear connector damage severities, shear connector damage positions and load positions on the interface slippage performance. Further analysis on numerical results showed that slippage divergence ratio is very sensitive to the shear connector damage severities and locations, which could be regarded as a good indicator to detect the shear connector damage scenarios.

5) A new Damage Cable Identifier (DCI) and a new Damage Degree Identifier (DDI) are proposed for the cable damage situation in a cable-stayed bridge, based on deck bending strain responses and Support Vector Machine (SVM). The approach of training DCI and DDI is introduced firstly. Then a real cable-stayed bridge, which is located in Western Sydney University campus over the Great Western highway, is studied as an example to verify the proposed damage identification method. The three-dimensional Finite Element Model (FEM) of the cable-stayed bridge is established using ANSYS, and calibrated by the measured mode shape, natural frequencies and its bending strain responses, when a Holden Colorado Ute travels through the bridge. Then under the same vehicle loads, the FEM bending strains of the longitude deck near the cable 1-4 anchors and cable 9-12 anchors are obtained when the bridge is intact and each cable of the cable 1-16 is damaged with different damage degrees respectively. Based on damage identification indexes, the training datasets and testing datasets are acquired. Eventually, DCI is trained using Support Vector Classification (SVC) and DDI is trained using Support Vector Regression (SVR). The testing datasets are input in DCI and DDI to check their accuracy and generalization capability. Different noise levels including 5%, 10%, 15%, 20%, 25%, 30%, 35%, 40% are considered to study their anti-nose capability. The results show that DCI and DDI both have good generalization capability and anti-noise capability.

8.2 Recommendations

The research in this thesis for structural load identification and damage detection is an important part in the vehicle-bridge interaction (VBI) monitoring system. However, there are still many challenges in bridge health monitoring based on VBI. Further investigation on the following topics is recommended:

1) In the existing moving force identification (MFI) research, the effect of unknown initial conditions and uncertainties is generally not considered. This makes existing MFI methods greatly restricted in terms of practical applications. In bridge operational conditions, the vehicle may not be in a static state before it enters the bridge. There are various uncertain factors and the stiffness parameters, boundary conditions and damping parameters of the bridge are difficult to be determined accurately. These uncertain factors cause a large deviation between the actual dynamic characteristics of the structure and the nominal design value. Therefore, it is necessary to study the problem of MFI under the unknown initial conditions and uncertainties and develop new method for operational loads identification (OLI).
2) Structural damage generally occurs only at local positions of the bridge and appears sparse in the physical space. Due to the limited sensor arrangement, such local damage is difficult to detect. VBI based methods can extract this sparse feature from the response induced by moving vehicular loads.
3) In practice, the traffic excitation is unknown and the structural damage identification from dynamic measurements on the bridge without the traffic information. Both the bridge model and its operational load are unknown, and these two factors determine the dynamic behaviour of bridge structures. In order to accurately assess the service status of bridges, it is necessary to study the simultaneous identification of unknown structural damage and unknown operational loads. However, compared with moving load identification or

structural damage identification, the number of unknown parameters involved in the simultaneous identification problem increases. In the case of limited measurement data, the adverse effects from incomplete data and measurement noise will be more prominent.

References

Abdullah, A.H. & Achintya, H. 2015, 'Structural health assessment at a local level using minimum information', *Engineering Structures*, vol. 88, pp. 100-10.

Alamdari, M.M., Kildashti, K., Samali, B. & Goudarzi, H.V. 2019, 'Damage diagnosis in bridge structures using rotation influence line: Validation on a cable-stayed bridge', *Engineering Structures*, vol. 185, pp. 1-14.

Arjomandi, K., Araki, Y. & MacDonald, T. 2019, 'Application of a hybrid structural health monitoring approach for condition assessment of cable-stayed bridges', *Journal of Civil Structural Health Monitoring*, vol. 9, no. 2, pp. 217-31.

Bartlett, F.D. & Flannelly, W.G. 1979, 'Model Verification of Force Determination for Measuring Vibratory Loads', *Journal of the American Helicopter Society*, vol. 24, no. 2, pp. 10-8.

Bartoli, G., Facchini, L., Pieraccini, M., Fratini, M. & Atzeni, C. 2008, 'Experimental utilization of interferometric radar techniques for structural monitoring', *Structural Control and Health Monitoring: The Official Journal of the International Association for Structural Control and Monitoring and of the European Association for the Control of Structures*, vol. 15, no. 3, pp. 283-98.

Cantieni, R. 1984, 'Dynamic load testing of highway bridges', *Transportation Research Record*, vol. 2, no. 950, pp. 141-8.

Carden, E.P. & Fanning, P. 2004, 'Vibration based condition monitoring: a review', *Structural health monitoring*, vol. 3, no. 4, pp. 355-77.

Carrión, F.J., Quintana, J.A. & Crespo, S.E. 2017, 'SHM of a stayed bridge during a structural failure, case study: the Rio Papaloapan Bridge', *Journal of Civil Structural Health Monitoring*, vol. 7, no. 2, pp. 139-51.

Casas, J.R. & Moughty, J.J. 2017, 'Bridge Damage Detection Based on Vibration Data: Past and New Developments', *Frontiers in Built Environment*, vol. 3, p. 4.

Cebon, D. 1989, 'Vehicle-Generated Road Damage: A Review', *Vehicle System Dynamics*, vol. 18, no. 1-3, pp. 107-50.

Chan, T.H.T., Law, S.S., Yung, T.H. & Yuan, X.R. 1999, 'An Interpretive Method for Moving Force Identification', *Journal of Sound and Vibration*, vol. 219, no. 3, pp. 503-24.

Chen, S., Yang, Z.C., Li, B. & Dang, H.X. 2012, 'Semi-analytical method to identify dynamic load in time domain', *Journal of Vibration and Shock*, vol. 31, pp. 99-104.

Chen, Z. & Chan, T.H. 2017, 'A truncated generalized singular value decomposition algorithm for moving force identification with ill-posed problems', *Journal of Sound and Vibration*, vol. 401, pp. 297-310.

Chen, Z., Chan, T.H. & Yu, L. 2020, 'Comparison of regularisation methods for moving force identification with ill-posed problems', *Journal of Sound and Vibration*, vol. 478, p. 115349.

Cho, S., Jo, H., Jang, S., Park, J., Jung, H.-J., Yun, C.-B., Spencer Jr, B.F. & Seo, J.-W. 2010, 'Structural health monitoring of a cable-stayed bridge using wireless smart sensor technology: data analyses', *Smart Structures and Systems*, vol. 6, no. 5_6, pp. 461-80.

Dong, J., Yan, X. & Li, S. 2018, 'Cable force monitoring and prediction for cable group of long-span cable-supported bridges', *Journal of Civil Structural Health Monitoring*, vol. 8, no. 4, pp. 597-605.

Fan, W. & Qiao, P.Z. 2011, 'Vibration-based damage identification methods: a review and comparative study', *Structural health monitoring*, vol. 10, no. 1, pp. 83-111.

Fang, L., Zhou, Y., Jiang, Y., Pei, Y. & Yi, W. 2020, 'Vibration-based damage detection of a steel-concrete composite slab using non-model-based and model-based methods', *Advances in Civil Engineering*, vol. 2020.

Feng, D., Sun, H. & Feng, M.Q. 2015, 'Simultaneous identification of bridge structural parameters and vehicle loads', *Computers & Structures*, vol. 157, pp. 76-88.

Feng, D.M. & Feng, M.Q. 2016, 'Output-only damage detection using vehicle-induced displacement response and mode shape curvature index', *Structural Control and Health Monitoring*, vol. 23, no. 8, pp. 1088-107.

Feng, W., Li, Q., Lu, Q., Li, C. & Wang, B. 2021, 'Group Relevance Vector Machine for sparse force localization and reconstruction', *Mechanical Systems and Signal Processing*, vol. 161.

González, A., Obrien, E.J. & McGetrick, P.J. 2012, 'Identification of damping in a bridge using a moving instrumented vehicle', *Journal of Sound and Vibration*, vol. 331, no. 18, pp. 4115-31.

Hansen, M.S., J, M 1990, 'On predicting and improving the condition of modal-model-based indirect force measurement algorithms', *Proceedings of the 8th International Modal Analysis Conference*, Kissimmee, pp. 115-20.

He, W.Y. & Zhu, S.Y. 2016, 'Moving load-induced response of damaged beam and its application in damage localization', *Journal of Vibration and Control*, vol. 22, no. 16, pp. 3601-17.

Hester, D. & González, A. 2014, 'A bridge-monitoring tool based on bridge and vehicle accelerations', *Structure and Infrastructure Engineering*, vol. 11, no. 5, pp. 619-37.

Hester, D. & González, A. 2017, 'A discussion on the merits and limitations of using drive-by monitoring to detect localised damage in a bridge', *Mechanical Systems and Signal Processing*, vol. 90, pp. 234-53.

Huang, H., Yang, J.N. & Zhou, L. 2010, 'Adaptive quadratic sum-squares error with unknown inputs for damage identification of structures', *Structural Control and Health Monitoring*, vol. 17, no. 4, pp. 404-426.

Huang, N., Huang, K. & Chiang, W.L. 2005, 'HHT-based Bridge Structural Health-Monitoring Method'. *Interdisciplinary Mathematical Sciences*, pp.263-287.

Huang, W., Tao, C., Ji, H. & Qiu, J. 2021, 'Enhancement of Wave Energy Dissipation in Two-Dimensional Acoustic Black Hole by Simultaneous Optimization of Profile and Damping Layer', *Journal of Sound and Vibration*, vol. 491, p. 115764.

Huang, Y., Wang, Y., Fu, J., Liu, A. & Gao, W. 2018, 'Measurement of the real-time deflection of cable-stayed bridge based on cable tension variations', *Measurement*, vol. 119, pp. 218-28.

Hwang, J.S., Kareem, A. & Kim, W.J. 2009, 'Estimation of modal loads using structural response', *Journal of Sound and Vibration*, vol. 326, no. 3-5, pp. 522-39.

Jacquelin, E., Bennani, A. & Hamelin, P. 2003, 'Force reconstruction: analysis and regularisation of a deconvolution problem', *Journal of Sound and Vibration*, vol. 265, no. 1, pp. 81-107.

Jayalakshmi, V., Lakshmi, K. & Mohan Rao, A.R. 2018, 'Dynamic force reconstruction techniques from incomplete measurements', *Journal of Vibration and Control*, vol. 24, no. 22, pp. 5321-44.

Jayalakshmi, V. & Rao, A.R.M. 2017, 'Simultaneous identification of damage and input dynamic force on the structure for structural health monitoring', *Structural and Multidisciplinary Optimization*, vol. 55, no. 6, pp. 2211-38.

Jia, Y., Yang, Z. & Song, Q. 2015, 'Experimental study of random dynamic loads identification based on weighted regularisation method', *Journal of Sound and Vibration*, vol. 342, pp. 113-23.

Kalhori, H., Alamdari, M.M. & Ye, L. 2018, 'Automated algorithm for impact force identification using cosine similarity searching', *Measurement*, vol. 122, pp. 648-57.

Kalhori, H., Makki Alamdari, M., Zhu, X. & Samali, B. 2018, 'Nothing-on-road axle detection strategies in bridge-weigh-in-motion for a cable-stayed bridge: case study', *Journal of Bridge Engineering*, vol. 23, no. 8, p. 05018006.

Keenahan, J. & O'Brien, E.J. 2014, 'Allowing for a rocking datum in the analysis of drive-by bridge inspections'.

Keenahan, J., Obrien, E.J., McGetrick, P.J. & Gonzalez, A. 2013, 'The use of a dynamic truck–trailer drive-by system to monitor bridge damping', *Structural Health Monitoring: An International Journal*, vol. 13, no. 2, pp. 143-57.

Khanam, S., Dutt, J.K. & Tandon, N. 2015, 'Impact Force Based Model for Bearing Local Fault Identification', *Journal of Vibration and Acoustics*, vol. 137, no. 5.

Khorram, A., Bakhtiar Nejad, F. & Rezaeian, M. 2012, 'Comparison studies between two wavelet based crack detection methods of a beam subjected to a moving load', *International Journal of Engineering Science*, vol. 51, pp. 204-15.

Kim, C.W., Isemoto, R., McGetrick, P.J., Kawatani, M. & Obrien, E.J. 2014, 'Drive-by bridge inspection from three different approaches', *Smart Structures and Systems*, vol. 13, no. 5, pp. 775-96.

Kim, S.W., Jeon, B.G., Cheung, J.H., Kim, S.D. & Park, J.B. 2017, 'Stay cable tension estimation using a vision-based monitoring system under various weather conditions', *Journal of Civil Structural Health Monitoring*, vol. 7, no. 3, pp. 343-57.

Kim, S.W., Jeon, B.G., Kim, N.S. & Park, J.-C. 2013, 'Vision-based monitoring system for evaluating cable tensile forces on a cable-stayed bridge', *Structural Health Monitoring*, vol. 12, no. 5-6, pp. 440-56.

Law, S.S., Chan, T.H.T. & Zeng, Q.H. 1997, 'Moving Force Identification: A Time Domain Method', *Journal of Sound and Vibration*, vol. 201, no. 1, pp. 1-22.

Law, S.S., Chan, T.H.T., Zhu, Q.X. & Zeng, Q.H. 2001, 'Regularisation in Moving Force Identification', *Journal of Engineering Mechanics*, vol. 127, no. 2, pp. 136-48.

Law, S.S. & Li, J. 2010, 'Updating the reliability of a concrete bridge structure based on condition assessment with uncertainties', *Engineering Structures*, vol. 32, no. 1, pp. 286-96.

Law, S.S. & Zhu, X.Q. 2004, 'Dynamic behavior of damaged concrete bridge structures under moving vehicular loads', *Engineering Structures*, vol. 26, no. 9, pp. 1279-93.

LeClerc, J.R., Worden, K., Staszewski, W.J. & Haywood, J. 2007, 'Impact detection in an aircraft composite panel—A neural-network approach', *Journal of Sound and Vibration*, vol. 299, no. 3, pp. 672-82.

Lee, J.W., Kim, J.D., Yun, C.B., Yi, J.H. & Shim, J.M. 2002, 'Health-Monitoring Method for Bridges under Ordinary Traffic Loadings', *Journal of Sound and Vibration*, vol. 257, no. 2, pp. 247-64.

Lei, Y., Jiang, Y. & Xu, Z. 2012, 'Structural damage detection with limited input and output measurement signals', *Mechanical Systems and Signal Processing*, vol. 28, pp. 229-43.

Li, H. & Ou, J. 2016, 'The state of the art in structural health monitoring of cable-stayed bridges', *Journal of Civil Structural Health Monitoring*, vol. 6, no. 1, pp. 43-67.

Li, H., Ou, J. & Zhou, Z. 2009, 'Applications of optical fibre Bragg gratings sensing technology-based smart stay cables', *Optics and Lasers in Engineering*, vol. 47, no. 10, pp. 1077-84.

Li, H., Zhang, F. & Jin, Y. 2014, 'Real‐time identification of time‐varying tension in stay cables by monitoring cable transversal acceleration', *Structural Control and Health Monitoring*, vol. 21, no. 7, pp. 1100-17.

Li, J. & Hao, H. 2015, 'Damage detection of shear connectors under moving loads with relative displacement measurements', *Mechanical Systems and Signal Processing*, vol. 60-61, pp. 124-50.

Li, J., Hao, H., Fan, K. & Brownjohn, J. 2015, 'Development and application of a relative displacement sensor for structural health monitoring of composite bridges', *Structural Control and Health Monitoring*, vol. 22, no. 4, pp. 726-42.

Li, J., Hao, H. & Zhu, H.P. 2014, 'Dynamic assessment of shear connectors in composite bridges with ambient vibration measurements', *Advances in Structural Engineering*, vol. 17, no. 5, pp. 617-37.

Li, Q. & Lu, Q. 2016, 'Impact localization and identification under a constrained optimization scheme', *Journal of Sound and Vibration*, vol. 366, pp. 133-48.

Lin, C.W. & Yang, Y.B. 2005, 'Use of a passing vehicle to scan the fundamental bridge frequencies: An experimental verification', *Engineering Structures*, vol. 27, no. 13, pp. 1865-78.

Lin, J., Guo, X., Zhi, H., Howson, W.P. & Williams, F.W. 2001, 'Computer simulation of structural random loading identification', *Computers & Structures*, vol. 79, no. 4, pp. 375-87.

Liu, J., Qiao, B., Chen, Y., Zhu, Y., He, W. & Chen, X. 2022, 'Impact force reconstruction and localization using nonconvex overlapping group sparsity', *Mechanical Systems and Signal Processing*, vol. 162, p. 107983.

Liu, J., Qiao, B., He, W., Yang, Z. & Chen, X. 2020, 'Impact force identification via sparse regularisation with generalized minimax-concave penalty', *Journal of Sound and Vibration*, vol. 484, p. 115530.

Liu, Y. & Shepard Jr, W.S. 2005, 'Dynamic force identification based on enhanced least squares and total least-squares schemes in the frequency domain', *Journal of sound and vibration*, vol. 282, no. 1-2, pp. 37-60.

Lourens, E., Reynders, E., De Roeck, G., Degrande, G. & Lombaert, G. 2012, 'An augmented Kalman filter for force identification in structural dynamics', *Mechanical Systems and Signal Processing*, vol. 27, pp. 446-60.

Lu, Z.R. & Liu, J.K. 2011, 'Identification of both structural damages in bridge deck and vehicular parameters using measured dynamic responses', *Computers & Structures*, vol. 89, no. 13-14, pp. 1397-405.

Ma, C.K. & Ho, C.C. 2004, 'An inverse method for the estimation of input forces acting on non-linear structural systems', *Journal of Sound and Vibration*, vol. 275, no. 3-5, pp. 953-71.

Majumder, L. & Manohar, C.S. 2004, 'Nonlinear reduced models for beam damage detection using data on moving oscillator–beam interactions', *Computers & Structures*, vol. 82, no. 2, pp. 301-14.

Malekjafarian, A., McGetrick, P.J. & Obrien, E.J. 2015, 'A Review of Indirect Bridge Monitoring Using Passing Vehicles', *Shock and Vibration*, vol. 2015, pp. 1-16.

Mao, Y., M; Guo, X, L; Li, H, B 2009, 'Regularisation solution to inverse problem of dynamic force identification', *Proceedings of the 18th National Conference on Structural Engineering*, pp. 378-81.

Mazurek, D.F. & DeWolf, J.T. 1990, 'Experimental Study of Bridge Monitoring Technique', *Journal of Structural Engineering*, vol. 116, no. 9, pp. 2532-49.

McGetrick, P.J., Kim, C.W., González, A. & Brien, E.J.O. 2015, 'Experimental validation of a drive-by stiffness identification method for bridge monitoring', *Structural Health Monitoring: An International Journal*, vol. 14, no. 4, pp. 317-31.

Mehrabi, A.B. 2006, 'In-service evaluation of cable-stayed bridges, overview of available methods and findings', *Journal of Bridge Engineering*, vol. 11, no. 6, pp. 716-24.

Nassif, H.H., Gindy, M. & Davis, J. 2005, 'Comparison of laser Doppler vibrometer with contact sensors for monitoring bridge deflection and vibration', *Ndt & E International*, vol. 38, no. 3, pp. 213-8.

National Bridge Inventory (NBI), https://www.fhwa.dot.gov/bridge/nbi.cfm.

Nazarian, E., Ansari, F. & Azari, H. 2016, 'Recursive optimization method for monitoring of tension loss in cables of cable-stayed bridges', *Journal of Intelligent Material Systems and Structures*, vol. 27, no. 15, pp. 2091-101.

Nazarian, E., Ansari, F., Zhang, X. & Taylor, T. 2016, 'Detection of tension loss in cables of cable-stayed bridges by distributed monitoring of bridge deck strains', *Journal of Structural Engineering*, vol. 142, no. 6, p. 04016018.

Nguyen, K.V. & Tran, H.T. 2010, 'Multi-cracks detection of a beam-like structure based on the on-vehicle vibration signal and wavelet analysis', *Journal of Sound and Vibration*, vol. 329, no. 21, pp. 4455-65.

Nie, J.G. & Cai, C.S. 2003, 'Steel–Concrete Composite Beams Considering Shear Slip Effects', *Journal of Structural Engineering*, vol. 129, no. 4, pp. 495-506.

Noh, M.H. & Lee, S.Y. 2013, 'A bivariate Gaussian function approach for inverse cracks identification of forced-vibrating bridge decks', *Inverse Problems in Science and Engineering*, vol. 21, no. 6, pp. 1047-73.

Obrien, E., McGetrick, P. & Gonzalez, A. 2014, *A drive-by inspection system via vehicle moving force identification*, vol. 13.

Okubo, N., Tanabe, S. & Tatsuno, T. 1985, 'Identification of forces generated by a machine under operating condition', *Proceedings of IMAC*, vol. 3, p. 92.

Okubo, N.T., S; Tatsuno, T. 1985, 'Identification of forces generated by a machine under operating condition', *Proceedings of the 3rd International Modal Analysis Conference* Orlando, pp. 920-7.

Oshima, Y., Yamamoto, K. & Sugiura, K. 2014, 'Damage assessment of a bridge based on mode shapes estimated by responses of passing vehicles', *Smart Structures and Systems*, vol. 13, no. 5, pp. 731-53.

Pakrashi, V., O'Connor, A. & Basu, B. 2009, 'A Bridge-Vehicle Interaction Based Experimental Investigation of Damage Evolution', *Structural Health Monitoring: An International Journal*, vol. 9, no. 4, pp. 285-96.

Pan, C.D., Yu, L. & Liu, H.L. 2017, 'Identification of moving vehicle forces on bridge structures via moving average Tikhonov regularisation', *Smart Materials and Structures*, vol. 26, no. 8, p. 085041.

Pan, S., Su, H., Wang, H. & Chu, J. 2010, 'The study of joint input and state estimation with Kalman filtering', *Transactions of the Institute of Measurement and Control*, vol. 33, no. 8, pp. 901-18.

Park, J., Ha, S. & Chang, F.K. 2009, 'Monitoring Impact Events Using a System-Identification Method', *AIAA Journal*, vol. 47, no. 9, pp. 2011-21.

Park, T., Noh, M.H., Lee, S.Y. & Voyiadjis, G.Z. 2009, 'Identification of a Distribution of Stiffness Reduction in Reinforced Concrete Slab Bridges Subjected to Moving Loads', *Journal of Bridge Engineering*, vol. 14, no. 5, pp. 355-65.

Pioldi, F. & Rizzi, E. 2016, 'A Full Dynamic Compound Inverse Method for output-only element-level system identification and input estimation from earthquake response signals', *Computational Mechanics*, vol. 58, no. 2, pp. 307-27.

Qiao, B., Ao, C., Mao, Z. & Chen, X. 2020, 'Non-convex sparse regularisation for impact force identification', *Journal of Sound and Vibration*, vol. 477.

Qiao, B., Liu, J., Liu, J., Yang, Z. & Chen, X. 2019, 'An enhanced sparse regularisation method for impact force identification', *Mechanical Systems and Signal Processing*, vol. 126, pp. 341-67.

Qiao, B., Mao, Z., Liu, J., Zhao, Z. & Chen, X. 2019, 'Group sparse regularisation for impact force identification in time domain', *Journal of Sound and Vibration*, vol. 445, pp. 44-63.

Qiao, B., Zhang, X., Gao, J. & Chen, X. 2016, 'Impact-force sparse reconstruction from highly incomplete and inaccurate measurements', *Journal of Sound and Vibration*, vol. 376, pp. 72-94.

Ren, W.-X., Sun, Z.S., Xia, Y., Hao, H. & Deeks, A.J. 2008, 'Damage identification of shear connectors with wavelet packet energy: laboratory test study', *Journal of structural engineering*, vol. 134, no. 5, pp. 832-41.

Ren, Y., Xu, X., Huang, Q., Zhao, D.Y. & Yang, J. 2019, 'Long-term condition evaluation for stay cable systems using dead load–induced cable forces', *Advances in Structural Engineering*, vol. 22, no. 7, pp. 1644-56.

Roveri, N. & Carcaterra, A. 2012, 'Damage detection in structures under traveling loads by Hilbert–Huang transform', *Mechanical Systems and Signal Processing*, vol. 28, pp. 128-44.

Samagassi, S., Khamlichi, A., Driouach, A. & Jacquelin, E. 2015, 'Reconstruction of multiple impact forces by wavelet relevance vector machine approach', *Journal of Sound and Vibration*, vol. 359, pp. 56-67.

Sha, R.H. 2005, 'Dynamic load identification for turbine generator set based on neural network', Dalian University of Technology, Dalian.

Sim, S.H., Li, J., Jo, H., Park, J.W., Cho, S., Spencer Jr, B.F. & Jung, H.-J. 2013, 'A wireless smart sensor network for automated monitoring of cable tension', *Smart Materials and Structures*, vol. 23, no. 2, p. 025006.

Sofyan, E.T., P, M 2000, 'Solving aerodynamic load inverse problems using a hybrid FEM-artificial intelligence', *Proceeding of Australasian Matlab Users Conference*.

Sun, H. & Betti, R. 2014, 'Simultaneous identification of structural parameters and dynamic input with incomplete output-only measurements', *Structural Control and Health Monitoring*, vol. 21, no. 6, pp. 868-89.

Sun, M., Makki Alamdari, M. & Kalhori, H. 2017, 'Automated operational modal analysis of a cable-stayed bridge', *Journal of Bridge Engineering*, vol. 22, no. 12.

Sun, Z., Li, G. & Geng, S. 2013, 'Study on stayed-cable health monitoring', *Intelligence Computation and Evolutionary Computation*, Springer, pp. 1091-8.

Tan, Z.X., Thambiratnam, D.P., Chan, T.H., Gordan, M. & Abdul Razak, H. 2020, 'Damage detection in steel-concrete composite bridge using vibration characteristics and artificial neural network', *Structure and Infrastructure Engineering*, vol. 16, no. 9, pp. 1247-61.

Wambacq, J., Maes, K., Rezayat, A., Guillaume, P. & Lombaert, G. 2019, 'Localization of dynamic forces on structures with an interior point method using group sparsity', *Mechanical Systems and Signal Processing*, vol. 115, pp. 593-606.

Wang, B.-T. & Chiu, C.H. 2003, 'Determination of Unknown Impact Force Acting on a Simply Supported Beam', *Mechanical Systems and Signal Processing*, vol. 17, no. 3, pp. 683-704.

Wang, G. & Ye, J. 2019, 'Localization and quantification of partial cable damage in the long‐span cable‐stayed bridge using the abnormal variation of temperature‐induced girder deflection', *Structural Control and Health Monitoring*, vol. 26, no. 1, p. e2281.

Wang, L. & Chan, T.H. 2009, 'Review of vibration-based damage detection and condition assessment of bridge structures using structural health monitoring', QUT Conference Proceedings.

Wang, Y. & Qu, W.L. 2011, 'Moving train loads identification on a continuous steel truss girder by using dynamic displacement influence line method', *International Journal of Steel Structures*, vol. 11, no. 2, pp. 109-15.

Wu, S.q. & Shi, Z.y. 2006, 'Identification of vehicle axle loads based on FEM-wavelet-Galerkin method', *Journal of Vibration Engineering*, vol. 4, p. 010.

Xia, Y., Hao, H. & Deeks, A.J. 2007, 'Dynamic assessment of shear connectors in slab–girder bridges', *Engineering Structures*, vol. 29, no. 7, pp. 1475-86.

Yang, Y., Li, S., Nagarajaiah, S., Li, H. & Zhou, P. 2016, 'Real-time output-only identification of time-varying cable tension from accelerations via complexity pursuit', *Journal of Structural Engineering*, vol. 142, no. 1, p. 04015083.

Yang, Y.B. & Chang, K.C. 2009, 'Extracting the bridge frequencies indirectly from a passing vehicle: Parametric study', *Engineering Structures*, vol. 31, no. 10, pp. 2448-59.

Yang, Y.B., Chang, K.C. & Li, Y.C. 2013, 'Filtering techniques for extracting bridge frequencies from a test vehicle moving over the bridge', *Engineering Structures*, vol. 48, pp. 353-62.

Yang, Y.B., Li, Y.C. & Chang, K.C. 2014, 'Constructing the mode shapes of a bridge from a passing vehicle: a theoretical study', *Smart Structures and Systems*, vol. 13, no. 5, pp. 797-819.

Yang, Y.B., Lin, C.W. & Yau, J.D. 2004, 'Extracting bridge frequencies from the dynamic response of a passing vehicle', *Journal of Sound and Vibration*, vol. 272, no. 3-5, pp. 471-93.

Yang, Y.B. & Yang, J.P. 2018, 'State-of-the-Art Review on Modal Identification and Damage Detection of Bridges by Moving Test Vehicles', *International Journal of Structural Stability and Dynamics*, vol. 18, no. 02.

Yi, T.H., Li, H.N. & Gu, M. 2013, 'Recent research and applications of GPS‐based monitoring technology for high‐rise structures', *Structural Control and Health Monitoring*, vol. 20, no. 5, pp. 649-70.

Yin, S.H. & Tang, C.Y. 2011, 'Identifying cable tension loss and deck damage in a cable-stayed bridge using a moving vehicle', *Journal of Vibration and Acoustics*, vol. 133, no. 2.

Yu, L. & Chan, T.H. 2007, 'Recent research on identification of moving loads on bridges', *Journal of Sound and Vibration*, vol. 305, no. 1-2, pp. 3-21.

Yu, L. & Chan, T.H.T. 2003, 'Moving force identification based on the frequency–time domain method', *Journal of Sound and Vibration*, vol. 261, no. 2, pp. 329-49.

Yu, Y., Cai, C. & Deng, L. 2016, 'State-of-the-art review on bridge weigh-in-motion technology', *Advances in Structural Engineering*, vol. 19, no. 9, pp. 1514-30.

Yu, Z., Xia, H., Goicolea, J.M. & Xia, C. 2016, 'Bridge Damage Identification from Moving Load Induced Deflection Based on Wavelet Transform and Lipschitz Exponent', *International Journal of Structural Stability and Dynamics*, vol. 16, no. 05.

Zhang, Q., Jankowski, Ł. & Duan, Z. 2010, 'Simultaneous identification of moving masses and structural damage', *Structural and Multidisciplinary Optimization*, vol. 42, no. 6, pp. 907-22.

Zhang, Q., Jankowski, Ł. & Duan, Z. 2013, 'Simultaneous Identification of Moving Vehicles and Bridge Damages Considering Road Rough Surface', *Mathematical Problems in Engineering*, vol. 2013, pp. 1-12.

Zhang, Y., Lie, S.T. & Xiang, Z.H. 2013, 'Damage detection method based on operating deflection shape curvature extracted from dynamic response of a passing vehicle', *Mechanical Systems and Signal Processing*, vol. 35, no. 1, pp. 238-54.

Zheng, X., Huang, P., Han, Q. & Chen, G. 2014, 'Bond behavior of interface between CFL and concrete under static and fatigue load', *Construction and Building Materials*, vol. 52, pp. 33-41.

Zhong, J., Liu, H. & Yu, L. 2019, 'Sparse regularisation for traffic load monitoring using bridge response measurements', *Measurement*, vol. 131, pp. 173-82.

Zhu, X. & Law, S.S. 2015, 'Structural health monitoring based on vehicle-bridge interaction: accomplishments and challenges', *Advances in Structural Engineering*, vol. 18, no. 12, pp. 1999-2015.

Zhu, X., Samali, B., Rashidi, M. & Alamdari, M. 2017, 'Long-term vibration monitoring of a cable-stayed bridge: effects of environmental and operational conditions', *SHMII 2017-8th International Conference on Structural Health Monitoring of Intelligent Infrastructure, Proceedings*.

Zhu, X.Q., Hao, H., Uy, B., Xia, Y. & Mirza, O. 2012, 'Dynamic Assessment of Shear Connection Conditions in Slab-Girder Bridges by Kullback-Leibler Distance', *Advances in Structural Engineering*, vol. 15, no. 5, pp. 771-80.

Zhu, X.Q. & Law, S.S. 2000, 'Identification of vehicle axle loads from bridge dynamic responses', *Journal of Sound and Vibration*, vol. 236, no. 4, pp. 705-24.

Zhu, X.Q. & Law, S.S. 2001, 'Orthogonal function in moving loads identification on a multi-span bridge', *Journal of Sound and Vibration*, vol. 245, no. 2, pp. 329-45.

Zhu, X.Q. & Law, S.S. 2002, 'Moving loads identification through regularisation', *Journal of engineering mechanics*, vol. 128, no. 9, pp. 989-1000.

Zhu, X.Q. & Law, S.S. 2003, 'Identification of Moving Interaction Forces with Incomplete Velocity Information', *Mechanical Systems and Signal Processing*, vol. 17, no. 6, pp. 1349-66.

Zhu, X.Q. & Law, S.S. 2006, 'Wavelet-based crack identification of bridge beam from operational deflection time history', *International Journal of Solids and Structures*, vol. 43, no. 7, pp. 2299-317.

Zhu, X.Q. & Law, S.S. 2016, 'Recent developments in inverse problems of vehicle-bridge interaction dynamics', *Journal of Civil Structural Health Monitoring*, vol. 6, no. 2, pp. 107-128.

Zhu, X.Q., Law, S.S. & Bu, J.Q. 2006, 'A state space formulation for moving loads identification', *Journal of vibration and acoustics*, vol. 128, no. 4, pp. 509-20.

Zhu, X.Q., Law, S.S., Huang, L. & Zhu, S.Y. 2018, 'Damage identification of supporting structures with a moving sensory system', *Journal of Sound and Vibration*, vol. 415, pp. 111-27.